Quantum Monte Carlo Studies of Strongly Interacting Fermionic Systems

by

Lucas Madeira

A Dissertation Presented in Partial Fulfillment
of the Requirements for the Degree
Doctor of Philosophy

Approved June 2018 by the
Graduate Supervisory Committee:

Kevin Schmidt, Chair
Ricardo Alarcon
Oliver Beckstein
Onur Erten

ARIZONA STATE UNIVERSITY

August 2018

ABSTRACT

In this dissertation two kinds of strongly interacting fermionic systems were studied: cold atomic gases and nucleon systems. In the first part I report $T = 0$ diffusion Monte Carlo results for the ground-state and vortex excitation of unpolarized spin-1/2 fermions in a two-dimensional disk. I investigate how vortex core structure properties behave over the BEC-BCS crossover. The vortex excitation energy, density profiles, and vortex core properties related to the current are calculated. A density suppression at the vortex core on the BCS side of the crossover and a depleted core on the BEC limit is found. Size-effect dependencies in the disk geometry were carefully studied. In the second part of this dissertation I turn my attention to a very interesting problem in nuclear physics. In most simulations of nonrelativistic nuclear systems, the wave functions are found by solving the many-body Schrödinger equations, and they describe the quantum-mechanical amplitudes of the nucleonic degrees of freedom. In those simulations the pionic contributions are encoded in nuclear potentials and electroweak currents, and they determine the low-momentum behavior. By contrast, in this work I present a novel quantum Monte Carlo formalism in which both relativistic pions and nonrelativistic nucleons are explicitly included in the quantum-mechanical states of the system. I report the renormalization of the nucleon mass as a function of the momentum cutoff, an Euclidean time density correlation function that deals with the short-time nucleon diffusion, and the pion cloud density and momentum distributions. In the two nucleon sector the interaction of two static nucleons at large distances reduces to the one-pion exchange potential, and I fit the low-energy constants of the contact interactions to reproduce the binding energy of the deuteron and two neutrons in finite volumes. I conclude by showing that the method can be readily applied to light-nuclei.

DEDICATION

To my father and Marina.

Ao meu pai e à Marina.

ACKNOWLEDGMENTS

Those who know me well also know that I am not a man of many words. Although this section is brief, the contributions listed here are not. First, I am thankful for my advisor Kevin. His patience and willingness to help are unmatched. I am also grateful for my collaborators, Stefano, Francesco, and Alessandro. Each one, in their own way, contributed to improving this work. I also thank Dr. Ubirajara van Kolck for bringing to my attention important aspects of the chiral EFT. I thank my group members, Cody and Rong, for the useful discussions. I am thankful for my committee members, Dr. Alarcon, Dr. Beckstein, Dr. Lunardini, and Dr. Erten for their useful comments and suggestions. I am also indebted to the department's staff, specially Araceli. I am also thankful for my other friends at ASU: Dr. Tanmay Vachaspati, Andy, Ayush, David, Denys, Ian(s), Jiawei, Nikhil, Paul, Sean, Sebastian, Taylor, Tucker, Tushar, and Zhang. I am grateful for my Italian friends, Lorenzo Contessi, Lorenzo Andreoli, and Luca, for their hospitality. None of this would be possible without the support of my father, my first and life-long advisor, and Marina, who has always inspired me to be the best physicist that I can.

TABLE OF CONTENTS

CHAPTER Page

CHAPTER Page

CHAPTER Page

LIST OF TABLES

TABLE Page

LIST OF FIGURES

FIGURE Page

FIGURE Page

FIGURE Page

FIGURE Page

Chapter 1

INTRODUCTION

The many-body problem has attracted much attention since the dawn of physics. There are two essential ingredients to this problem. First, we need many bodies to be present: many atoms, many electrons, many nucleons, etc. Secondly, these bodies must interact, otherwise the problem would be reduced to many one-body problems. Fermions, such as electrons, protons and neutrons, compose all the usual matter around us. The Fermi-Dirac statistics governs the behavior of a wide range of systems: electrons in metals, nuclei, atoms, and even neutron stars. In this work, we focus on two types of many-body problems concerning strongly interacting fermionic systems: cold atomic gases and nucleon systems.

After the successful realization of the strongly interacting Fermi gases in three dimensions (3D), much attention has been payed to Fermi systems that have even stronger correlations, such as low-dimensional fermionic gases (Levinsen and Parish (2015)). Two-dimensional (2D) systems are of particular interest, due to insights into complex solid-state systems such as high-temperature superconductors and semiconductor interfaces. Ultracold atomic gases are dilute systems in which the interparticle interactions can be tuned via Feshbach resonances, leading to strongly interacting systems. This allows for the investigation of the crossover from BCS-type pairing to the Bose regime of tightly bound dimers. The concept of a BCS-BEC crossover was first applied to 2D Fermi gases by Randeria *et al.* (1989). Such mean-field calculations can qualitatively describe either very large or very small pair sizes, corresponding to the BCS or BEC limits, respectively. The intermediate regime is not expected to be accurately described by a mean-field theory, especially at unitarity where the system

lacks any perturbative expansion parameter. Hence, quantum Monte Carlo methods are invaluable tools to calculate properties of cold fermionic gases over all BCS-BEC crossover. In this work we studied properties of the ground-state and vortex excitation of spin-1/2 fermions in a 2D disk (Madeira *et al.* (2017)). Further motivation and a more comprehensive introduction to this problem is given in Chap. 3.

The second part of this dissertation deals with a very challenging problem in nuclear physics: the development of a method capable of including explicit pionic degrees of freedom in the frame of chiral effective field theory (EFT). Most Monte Carlo simulations of nucleon systems only include nucleonic degrees of freedom, while contributions from pions are implicitly included in the interaction potentials (Carlson *et al.* (2015a)). We developed a novel formalism which allows us to explicitly include contributions of the pion fields in Green's function Monte Carlo (GFMC) simulations.

Our goal with this formalism is to be able investigate problems that are not accessible to standard potential models where pions are included implicitly. Here we list some possibilities that we plan to investigate in the future. One of these problems is the scattering of pions by nucleons. The extraction of phase shifts from our simulations is not trivial because we work with a box geometry, however formalism such as the one of Bernard *et al.* (2008), developed for lattice QCD, may bridge the gap. The effect of pions on A-body systems is also a problem of great interest. One advantage of our formalism is that at leading order (LO) it already includes pion-mediated three-body forces that only start to appear at next-to next-to leading order (NNLO) in standard simulations (Epelbaum *et al.* (2011)). Finally, an example of nucleon systems that clearly requires explicit pionic degrees of freedom is the pion condensate, which attracts the interest of both the nuclear physics and astrophysics communities. The pion condensate is a conjectured state of neutron matter at extremely dense regimes, such as the ones found in neutron stars. The condensate is characterized

by the macroscopic occupation of one of the pion modes. The condensate manifests itself as a neutron spin-density wave, where alternating layers of opposite spins are located where the gradient of the pion field is maximum. Since we have explicit pion degrees of freedom, we should be able to observe that the ground-state of the system, in the pertinent density regime, corresponds to a macroscopic occupation of a single pion mode.

In this dissertation we present an extension of our results presented in Madeira *et al.* (2016, 2017, 2018). This work is structured as it follows. We start with the quantum Monte Carlo methods, which are used in both cold gases and nucleon systems, in Chapter 2. We present the variational Monte Carlo (VMC) and diffusion Monte Carlo (DMC) methods. Chapter 3 deals with 2D Fermi gases. After a brief introduction on the BEC-BCS crossover and vortices in two-dimensional fermionic systems, we present our methodology. We derive the wave functions we developed to study the ground-state and vortex excitation in these systems. Finally, we report our results. In Chapter 4 we introduce our formalism that allows for the inclusion of explicit pion degrees of freedom in quantum Monte Carlo (QMC) simulations. We present our formalism in the mold of chiral EFT, which includes expressions for the Lagrangian and the pion field. We derive the Hamiltonians and wave functions for A-nucleon systems, and we comment on technical aspects of the implementation. We report our one- and two-nucleon results. Finally, we present our final remarks in Chapter 5. In Appendix A we review the optimization algorithms used to determine the variational parameters in the wave functions. In Appendix B we show how unbiased estimators can be calculated in diffusion simulations. We list our conventions in Appendix C.

Chapter 2

QUANTUM MONTE CARLO METHODS

2.1 Monte Carlo methods

The core of a Monte Carlo simulation is the evaluation of multidimensional integrals by sampling the integrand statistically and averaging the sampled values (Foulkes *et al.* (2001)). Suppose we define a $3N$-dimensional vector,

$$\mathbf{R} = (\boldsymbol{r}_1, \boldsymbol{r}_2, \ldots, \boldsymbol{r}_N), \tag{2.1}$$

where $\boldsymbol{r}_i$ is the position of the i-th particle. Commonly, a particular $\mathbf{R}$ is called a *walker*. If the probability density of finding the particles in the configuration $\mathbf{R}$ is given by

$$\begin{aligned} \mathcal{P}(\mathbf{R}) &\geqslant 0, \\ \int d\mathbf{R}\mathcal{P}(\mathbf{R}) &= 1, \end{aligned} \tag{2.2}$$

then let $\{\mathbf{R}_m : m = 1, M\}$ be a set of uncorrelated configurations distributed accordingly to $\mathcal{P}(\mathbf{R})$. We define a random variable $\mathbf{Z}_f$ by

$$\mathbf{Z}_f = \frac{[f(\mathbf{R}_1) + f(\mathbf{R}_2) + \cdots + f(\mathbf{R}_M)]}{M}. \tag{2.3}$$

The function $f(\mathbf{R})$ is any *reasonable* function with mean μ_f and variance σ_f^2 given by

$$\begin{aligned} \mu_f &= \int d\mathbf{R} f(\mathbf{R})\mathcal{P}(\mathbf{R}), \\ \sigma_f^2 &= \int d\mathbf{R}[f(\mathbf{R}) - \mu_f]^2\mathcal{P}(\mathbf{R}). \end{aligned} \tag{2.4}$$

For large enough M, $\mathbf{Z}_f$ is normally distributed with mean μ_f and standard deviation $\sigma_f/\sqrt{M}$. Thus, regardless of $\mathcal{P}(\mathbf{R})$, the mean value of a function of $\mathbf{R}$ will be a good

estimator of the mean of that function with respect to $\mathcal{P}(\mathbf{R})$. Moreover, the standard deviation will decrease as $1/\sqrt{M}$, regardless of the dimension of the integral.

Suppose we want to evaluate an integral such as

$$I = \int d\mathbf{R} g(\mathbf{R}). \tag{2.5}$$

We begin by introducing an "importance function" $\mathcal{P}(\mathbf{R})$ and cast the integral in the form

$$I = \int d\mathbf{R} f(\mathbf{R}) \mathcal{P}(\mathbf{R}), \tag{2.6}$$

where $f(\mathbf{R}) \equiv g(\mathbf{R})/\mathcal{P}(\mathbf{R})$. The importance function is chosen such that it obeys Eq. (2.2), hence it is a probability density. The value of I may be obtained by drawing an infinite number of vectors from $\mathcal{P}(\mathbf{R})$,

$$I = \lim_{M\to\infty} \left\{ \frac{1}{M} \sum_{m=1}^{M} f(\mathbf{R}_m) \right\}. \tag{2.7}$$

A Monte Carlo estimate of I is obtained by a large, but finite, number of samples drawn from $\mathcal{P}(\mathbf{R})$,

$$I \approx \frac{1}{M} \sum_{m=1}^{M} f(\mathbf{R}_m). \tag{2.8}$$

The variance σ_f^2/M is

$$\frac{\sigma_f^2}{M} \approx \frac{1}{M(M-1)} \sum_{m=1}^{M} \left[f(\mathbf{R}_m) - \frac{1}{M} \sum_{n=1}^{M} f(\mathbf{R}_n) \right]^2, \tag{2.9}$$

leading to error bars of $\pm\sigma_f/\sqrt{M}$ on the computed value of I. A wise choice of $\mathcal{P}(\mathbf{R})$ can significantly reduce the variance for a fixed number of samples.

2.1.1 The Metropolis algorithm

The method described in the previous section relies on evaluating multidimensional integrals by sampling probability distributions in high-dimensional spaces.

Generally, normalizations of these distributions are unknown. The Metropolis rejection algorithm (Metropolis *et al.* (1953)) allows us to sample complex distributions without knowledge of their normalizations. The Metropolis algorithm generates a sequence of sampling points $\mathbf{R}_m$, and it can be summarized as the following:

(1) Start the walker at a random position $\mathbf{R}$.

(2) Make a trial move to a new position $\mathbf{R}'$ chosen from a probability density function $T(\mathbf{R}' \leftarrow \mathbf{R})$.

(3) Accept the trial move to $\mathbf{R}'$ with probability

$$A(\mathbf{R}' \leftarrow \mathbf{R}) = \min\left(1, \frac{T(\mathbf{R} \leftarrow \mathbf{R}')\mathcal{P}(\mathbf{R}')}{T(\mathbf{R}' \leftarrow \mathbf{R})\mathcal{P}(\mathbf{R})}\right), \tag{2.10}$$

If the trial move is accepted, $\mathbf{R}'$ becomes the next walker, otherwise $\mathbf{R}$ is the next walker. If $\mathcal{P}(\mathbf{R})$ is high, points near $\mathbf{R}$ may occur many times in the set of points making up the random walk.

(4) Return to step (2) and repeat.

To understand how this algorithm works, let us consider an enormous number of walkers executing random walks according to the algorithm. The probability that a walker at $\mathbf{R}$ is taken to $d\mathbf{R}'$ in one move is $d\mathbf{R}'A(\mathbf{R}' \leftarrow \mathbf{R})T(\mathbf{R}' \leftarrow \mathbf{R})$, the average number of walkers moving from $d\mathbf{R} \rightarrow d\mathbf{R}'$ in a single move is

$$d\mathbf{R}'A(\mathbf{R}' \leftarrow \mathbf{R})T(\mathbf{R}' \leftarrow \mathbf{R}) \times n(\mathbf{R})d\mathbf{R}. \tag{2.11}$$

This must be balanced with the number moving from $d\mathbf{R}' \rightarrow d\mathbf{R}$,

$$d\mathbf{R}'A(\mathbf{R}' \leftarrow \mathbf{R})T(\mathbf{R}' \leftarrow \mathbf{R})n(\mathbf{R})d\mathbf{R} = d\mathbf{R}A(\mathbf{R} \leftarrow \mathbf{R}')T(\mathbf{R} \leftarrow \mathbf{R}')n(\mathbf{R}')d\mathbf{R}'. \tag{2.12}$$

Hence, $n(\mathbf{R})$ satisfies

$$\frac{n(\mathbf{R})}{n(\mathbf{R}')} = \frac{A(\mathbf{R} \leftarrow \mathbf{R}')T(\mathbf{R} \leftarrow \mathbf{R}')}{A(\mathbf{R}' \leftarrow \mathbf{R})T(\mathbf{R}' \leftarrow \mathbf{R})}. \tag{2.13}$$

Since the ratio of acceptance probabilities are

$$\frac{A(\mathbf{R} \leftarrow \mathbf{R}')}{A(\mathbf{R}' \leftarrow \mathbf{R})} = \frac{T(\mathbf{R}' \leftarrow \mathbf{R})\mathcal{P}(\mathbf{R})}{T(\mathbf{R} \leftarrow \mathbf{R}')\mathcal{P}(\mathbf{R}')}, \tag{2.14}$$

then

$$\frac{n(\mathbf{R})}{n(\mathbf{R}')} = \frac{\mathcal{P}(\mathbf{R})}{\mathcal{P}(\mathbf{R}')}. \tag{2.15}$$

Therefore, the equilibrium walker density $n(\mathbf{R})$ is proportional to $\mathcal{P}(\mathbf{R})$, and the probability of finding any given walker in $d\mathbf{R}$ is $\mathcal{P}(\mathbf{R})d\mathbf{R}$, as required. A rigorous derivation of the results presented in this section is given in Feller (1957), where convergence of the method is also shown.

2.2 Variational Monte Carlo

The Variational Monte Carlo method is based on the variational principle, and the Monte Carlo method is applied in the evaluation of the resulting multidimensional integrals (Foulkes *et al.* (2001)). It relies on a trial wave function Ψ_T which should mimic as many as possible properties of the true ground-state function Ψ_0.

The expectation value of H, evaluated with a trial wave function Ψ_T, provides an upper bound on the exact ground-state energy E_0

$$E_V = \frac{\int \Psi_T^*(\mathbf{R}) H \Psi_T(\mathbf{R}) d\mathbf{R}}{\int \Psi_T^*(\mathbf{R}) \Psi_T(\mathbf{R}) d\mathbf{R}} \geqslant E_0, \tag{2.16}$$

where $\mathbf{R}$= $(\boldsymbol{r}_1, \boldsymbol{r}_2, \ldots, \boldsymbol{r}_N)$ is a $3N$-dimensional vector with the coordinates of the N particles. This property can be easily verified. Consider the expansion

$$\Psi_T = \sum_i \alpha_i \Psi_i, \tag{2.17}$$

where $\{\Psi_i\}$ are the eigenstates of H with eigenvalues $\{E_i\}$. The substitution of the last expression in Eq. (2.16) shows that E_V is an upper bound of the exact ground-state energy.

The application of the Monte Carlo method in the evaluation of Eq. (2.16) is accomplished by rewriting this equation in the form

$$E_V = \frac{\int |\Psi_T(\mathbf{R})|^2 \left[\Psi_T(\mathbf{R})^{-1} H \Psi_T(\mathbf{R})\right] d\mathbf{R}}{\int |\Psi_T(\mathbf{R})|^2 d\mathbf{R}}. \tag{2.18}$$

The Metropolis algorithm then can be used to sample a set of points $\{\mathbf{R}_m : m = 1, M\}$ from the configuration-space, with the probability density

$$\mathcal{P}(\mathbf{R}) = \frac{|\Psi_T(\mathbf{R})|^2}{\int |\Psi_T(\mathbf{R})|^2 d\mathbf{R}}. \tag{2.19}$$

We define a "local energy" $E_L(\mathbf{R}) = \Psi_T(\mathbf{R})^{-1} H \Psi_T(\mathbf{R})$ and, at each of the points, it is evaluated and its average energy accumulated

$$E_V \approx \frac{1}{M} \sum_{m=1}^{M} E_L(\mathbf{R}_m). \tag{2.20}$$

The trial moves can be sampled from a Gaussian centered on the current position of the walker and the variance is chosen such that the average acceptance probability is $\approx 50\%$. Expectation values of operators other than the Hamiltonian can be computed in analogous ways.

2.3 Diffusion Monte Carlo

Diffusion Monte Carlo is a method for solving imaginary-time many-body Schrödinger equation (Foulkes *et al.* (2001)),

$$-\partial_t \Phi(\mathbf{R}, t) = (H - E_T)\Phi(\mathbf{R}, t), \tag{2.21}$$

where t is real and it measures the progress in imaginary time, and E_T is an energy offset.

In the integral form Eq. (2.21) is rewritten as

$$\Phi(\mathbf{R}, t+\tau) = \int G(\mathbf{R} \leftarrow \mathbf{R}', \tau)\Phi(\mathbf{R}', t)d\mathbf{R}', \tag{2.22}$$

where

$$G(\mathbf{R} \leftarrow \mathbf{R}', \tau) = \langle \mathbf{R}| \exp\left[-\tau(H - E_T)\right]|\mathbf{R}'\rangle \tag{2.23}$$

is the Green's function. For $t > 0$ it obeys the same equation as $\Phi(\mathbf{R}, t)$,

$$-\partial_t G(\mathbf{R} \leftarrow \mathbf{R}', \tau) = (H - E_T)G(\mathbf{R} \leftarrow \mathbf{R}', \tau), \tag{2.24}$$

with the initial condition $G(\mathbf{R} \leftarrow \mathbf{R}', 0) = \delta(\mathbf{R} - \mathbf{R}')$. The Green's function can be expressed as

$$G(\mathbf{R} \leftarrow \mathbf{R}', \tau) = \sum_i \Psi_i(\mathbf{R}) \exp\left\{-\tau(E_i - E_T)\right\}\Psi_i^*(\mathbf{R}'), \tag{2.25}$$

where $\{\Psi_i\}$ and $\{E_i\}$ are the complete set of eigenstates and eigenenergies of H, respectively. As $\tau \to \infty$, the operator $\exp\left\{-\tau(E_i - E_T)\right\}$ projects out the lowest eigenstate $|\Psi_0\rangle$ that has non-zero overlap with an initial state $|\Phi_{\text{init}}\rangle$,

$$\begin{aligned}\lim_{\tau\to\infty} \langle \mathbf{R}| \exp\left[-\tau(H - E_T)\right]|\Phi_{\text{init}}\rangle &= \lim_{\tau\to\infty} \int G(\mathbf{R} \leftarrow \mathbf{R}', \tau)\Phi_{\text{init}}(\mathbf{R}')d\mathbf{R}' \\ &= \lim_{\tau\to\infty} \sum_i \Psi_i(\mathbf{R}) \exp\left[-\tau(E_i - E_T)\right]\langle\Psi_i|\Phi_{\text{init}}\rangle. \end{aligned} \tag{2.26}$$

By adjusting $E_T = E_0$, and taking the limit $\tau \to \infty$, only the $|\Psi_0\rangle$ state is projected, since the higher energy states are all exponentially damped because their energies are higher than E_0.

If we neglect potential terms in Eq. (2.21), it simplifies to

$$\partial_t \Phi_0(\mathbf{R}, t) = \frac{\hbar^2}{2m} \sum_{i=1}^{N} \nabla_i^2 \Phi_0(\mathbf{R}, t). \tag{2.27}$$

The Green's function for this problem is

$$G_0(\mathbf{R} \leftarrow \mathbf{R}', \tau) = \left[\frac{m}{2\pi\hbar^2\tau}\right]^{3N/2} \exp\left[-\frac{m(\mathbf{R} - \mathbf{R}')^2}{2\hbar^2\tau}\right]. \tag{2.28}$$

If we consider the Hamiltonian with both kinetic and potential terms, the exact Green's function is known only for a few special cases. The Trotter-Suzuki formula can be used to obtain an approximation of the Green's function. For two operators A and B,

$$e^{-\tau(A+B)} = e^{-\tau B/2} e^{-\tau A} e^{-\tau B/2} + \mathcal{O}(\tau^3). \tag{2.29}$$

If $A = T$, where T is the kinetic energy operator, and $B = V - E_T$, V being the potential energy operator, we have

$$\begin{aligned} G(\mathbf{R} \leftarrow \mathbf{R}', \tau) &= \langle \mathbf{R} | e^{-\tau(T+V-E_T)} | \mathbf{R}' \rangle \\ &\approx e^{-\tau[V(\mathbf{R})-E_T]/2} \langle \mathbf{R} | e^{-\tau T} | \mathbf{R}' \rangle e^{-\tau[V(\mathbf{R}')-E_T]/2}. \end{aligned} \tag{2.30}$$

The approximate Green's function for small τ is therefore

$$G(\mathbf{R} \leftarrow \mathbf{R}', \tau) = G_0(\mathbf{R} \leftarrow \mathbf{R}', \tau) \exp\left[-\tau[V(\mathbf{R}) + V(\mathbf{R}') - 2E_T]/2\right], \tag{2.31}$$

and the error is proportional to τ^3. The exponential

$$P = \exp\left[-\tau[V(\mathbf{R}) + V(\mathbf{R}') - 2E_T]/2\right] \tag{2.32}$$

is a time-dependent reweighting of the Green's function. This change of normalization is incorporated in the calculations by using the *branching* algorithm, in which P determines the number of surviving walkers in each step. The procedure is:

(1) If $P < 1$ the walker continues its evolution with probability P.

(2) If $P \geqslant 1$ the walker continues and, in addition, a new walker is created in the same position with probability $P - 1$.

One way the number M_{new} of walkers evolving to the next step at a given position can be coded as

$$M_{\text{new}} = \text{INT}(P + \xi), \tag{2.33}$$

where INT is the integer part of a real number and ξ is a random number drawn from a uniform distribution in the interval [0,1]. The energy offset E_T is used to control

the population of walkers. By adjusting E_T, the total number of walkers fluctuates around a desirable value.

The ground-state energy can be calculated by the mixed estimate

$$\langle H \rangle_{\rm mix} = \frac{\langle \Psi_T | H | \Phi(t \to \infty) \rangle}{\langle \Psi_T | \Phi(t \to \infty) \rangle} = E_0 \frac{\langle \Psi_T | \Phi(t \to \infty) \rangle}{\langle \Psi_T | \Phi(t \to \infty) \rangle} = E_0. \tag{2.34}$$

In Sec. 4.8 we show the changes to the DMC algorithm so that it can be used in systems with spin/isospin degrees of freedom.

2.3.1 Importance sampling

The simple DMC algorithm described so far is spectacularly inefficient. The main reason is that P from Eq. (2.32) may fluctuate wildly between steps. This difficulty is overcome by carrying out an *importance-sampling transformation* using a trial wave function $\Psi_T(\mathbf{R})$. Let us multiply Eq. (2.21) by $\Psi_T(\mathbf{R})$ and introduce $f(\mathbf{R}, t) = \Phi(\mathbf{R}, t)\Psi_T(\mathbf{R})$. After some manipulations,

$$-\partial f(\mathbf{R}, t) = -\frac{1}{2}\nabla^2 f(\mathbf{R}, t) + \nabla \cdot [\mathbf{v}_D(\mathbf{R}) f(\mathbf{R}, t)] + [E_L(\mathbf{R}) - E_T] f(\mathbf{R}, t), \tag{2.35}$$

where $\nabla = (\nabla_1, \ldots, \nabla_N)$, $\mathbf{v}_D(\mathbf{R})$ is the $3N$-dimensional drift velocity,

$$\mathbf{v}_D(\mathbf{R}) = \nabla \ln |\Psi_T(\mathbf{R})| = \Psi_T(\mathbf{R})^{-1} \nabla \Psi_T(\mathbf{R}). \tag{2.36}$$

The integral equation becomes

$$f(\mathbf{R}, t + \tau) = \int \tilde{G}(\mathbf{R} \leftarrow \mathbf{R}', \tau) f(\mathbf{R}', t) d\mathbf{R}', \tag{2.37}$$

where

$$\tilde{G}(\mathbf{R} \leftarrow \mathbf{R}', \tau) \equiv \Psi_T(\mathbf{R}) G(\mathbf{R} \leftarrow \mathbf{R}', \tau) \Psi_T(\mathbf{R}')^{-1}. \tag{2.38}$$

The short-time approximation to $\tilde{G}(\mathbf{R} \leftarrow \mathbf{R}', \tau)$ is

$$\tilde{G}(\mathbf{R} \leftarrow \mathbf{R}', \tau) \approx G_d(\mathbf{R} \leftarrow \mathbf{R}', \tau) G_b(\mathbf{R} \leftarrow \mathbf{R}', \tau), \tag{2.39}$$

where

$$\begin{aligned} G_d(\mathbf{R} \leftarrow \mathbf{R}', \tau) &= (2\pi\tau)^{-3N/2} \exp\left[-\frac{[\mathbf{R} - \mathbf{R}' - \tau \mathbf{v}_D(\mathbf{R}')]^2}{2\tau} \right], \\ G_b(\mathbf{R} \leftarrow \mathbf{R}', \tau) &= \exp\left\{ -\tau [E_L(\mathbf{R}) + E_L(\mathbf{R}') - 2E_T]/2 \right\}. \end{aligned} \tag{2.40}$$

Eq. (2.40) is a typical implementation of importance sampling, however other related methods can be used to sample Eq. (2.38). Importance sampling has several consequences. The density of walkers is increased (decreased) where Ψ_T is large (small), because $\mathbf{v}_D(\mathbf{R})$ carries the walkers along in the direction of increasing $|\Psi_T|$. Moreover, the exponent in the reweighting term contains the local energy, instead of the potential. This is crucial because, for a good trial wave function, the local energy is close to the ground-state energy and approximately constant, thus diminishing population fluctuations.

Importance sampling is also extremely helpful in fulfilling the fixed-node constraint. Whenever a walker approaches the nodal surface, the drift velocity grows and pushes it away. Despite that, in the event of a walker crossing the nodal surface, the walker is eliminated.

Note that the trial wave function $\Psi_T(\mathbf{R})$ is used in three different ways: approximation of the ground-state in the VMC calculation, importance function, and for avoiding the sign problem as we will see in the next section.

2.3.2 The fixed-node approximation

So far we have assumed that the wave function is positive everywhere, which is not true for fermions due to the antisymmetry requirement. Unfortunately, DMC will

be stable only for positive distributions. For example, the denominator of a matrix element such as the mixed energy contains the sum $\sum_{i=1}^{N_s} P_i \Psi_T(\mathbf{R}_i)$. If the path of sample i has crossed nodes of Ψ_T an odd number of times, the contribution to the sum will be negative. For large times, the contributions of the negative paths cancel almost completely the contributions of the paths that have not crossed the nodes (or crossed an even number of times). The signal dies out exponentially compared to the noise.

Fixed-node DMC (Anderson (1975)) is an alternative method to overcome the sign problem. A trial many-body wave function is chosen and used to define a trial many-body nodal surface. In a three-dimensional system with N fermions, the wave function depends on $3N$ variables and the trial nodal surface is a $(3N-1)$-dimensional surface. If a walker in a proposed move crosses the nodal surface, it is deleted.

The fixed-node DMC algorithm then produces the lowest-energy state given the nodal surface. Therefore, fixed-node DMC may be regarded as a variational method that gives exact results provided that the nodal surface is exact.

2.3.3 Extrapolated estimators

Expectations of quantities that do not commute with the Hamiltonian can be calculated using a combination of mixed and variational estimators (Foulkes *et al.* (2001)),

$$\langle \Phi|S|\Phi\rangle \approx 2\langle \Phi|S|\Psi_T\rangle - \langle \Psi_T|S|\Psi_T\rangle + \mathcal{O}\left[(\Phi-\Psi_T)^2\right], \tag{2.41}$$

where S is the operator related to some physical quantity of interest. For nonnegative quantities, for example the density, another possibility is

$$\langle \Phi|S|\Phi\rangle \approx \frac{\langle \Phi|S|\Psi_T\rangle^2}{\langle \Psi_T|S|\Psi_T\rangle} + \mathcal{O}\left[(\Phi-\Psi_T)^2\right]. \tag{2.42}$$

Such combinations of VMC and DMC estimators are called extrapolated estimators.

2.3.4 *Forward walking*

The direct calculation of the expectation value of an operator $S(\mathbf{R})$ other than the Hamiltonian (or an operator that commutes with H) from $\Phi_0(\mathbf{R})$ corresponds to a matrix element which is usually called a "mixed estimator",

$$\langle S(\mathbf{R})\rangle_m = \frac{\langle \Psi_T(\mathbf{R})|S(\mathbf{R})|\Phi_0(\mathbf{R})\rangle}{\langle \Psi_T(\mathbf{R})|\Phi_0(\mathbf{R})\rangle}. \tag{2.43}$$

There are several methods to compute expectation values of quantities, such as the density, that do not commute with H. One of them is the extrapolation method where the results of diffusion and variational simulations are combined, see Sec. 2.3.3. However, the accuracy of the extrapolation method relies on the quality of the trial wave function. Moreover, even in the case of accurate trial wave functions, the bias of the extrapolated estimator is difficult to evaluate. One alternative is the forward walking method, which is discussed in detail in Casulleras and Boronat (1995). This method relies on the calculation of the asymptotic offspring of walkers coming from the branching term to compute the exact estimator,

$$\langle S(\mathbf{R})\rangle_e = \frac{\langle \Phi_0(\mathbf{R})|S(\mathbf{R})|\Phi_0(\mathbf{R})\rangle}{\langle \Phi_0(\mathbf{R})|\Phi_0(\mathbf{R})\rangle}. \tag{2.44}$$

A more detailed discussion of forward walking and unbiased estimators is presented in Appendix B.

2.4 QMC on parallel computers

Monte Carlo calculations are intrinsically parallel. The calculations performed on each walker are independent, and may be carried out in parallel. QMC calculations are very suitable for parallel architecture machines, which offer orders of magnitude more computational power.

The most common paradigm used in QMC on massively parallel processors is the "master-slave", with one processor orchestrating the whole simulation. In VMC simulations, the argument for using parallel computers is even more compelling. Each process independently runs a simulation and accumulates its own set of observables; at the end of the run the master processor gathers and averages the results. The situation is similar in DMC and GFMC simulations, however some inter-process communication is required during the simulation to control the population of walkers and perform the load balance between processes.

Our code, in the computational sense, is very similar to an auxiliary field diffusion Monte Carlo (AFDMC) code developed together with our collaborators. The AFDMC code has been successfully used to calculate properties of a plethora of systems: nuclear matter, neutron matter, and medium-mass nuclei (see Carlson *et al.* (2015a) and references therein). Although heavy load-balancing is involved, the AFDMC code shows strong scaling up to 96,000 cores on Edison at National Energy Research Scientific Computing Center (NERSC) - Edison is a Cray XC30, with a peak performance of 2.57 petaflops/sec, 133,824 compute cores, 357 terabytes of memory, and 7.56 petabytes of disk. In Fig. 2.1 (Stefano Gandolfi, private communication, 2018) we show the time it takes to propagate for 100 steps 96,000 configurations of 28 nucleons in a box with a number density of 0.16 fm^{-3}.

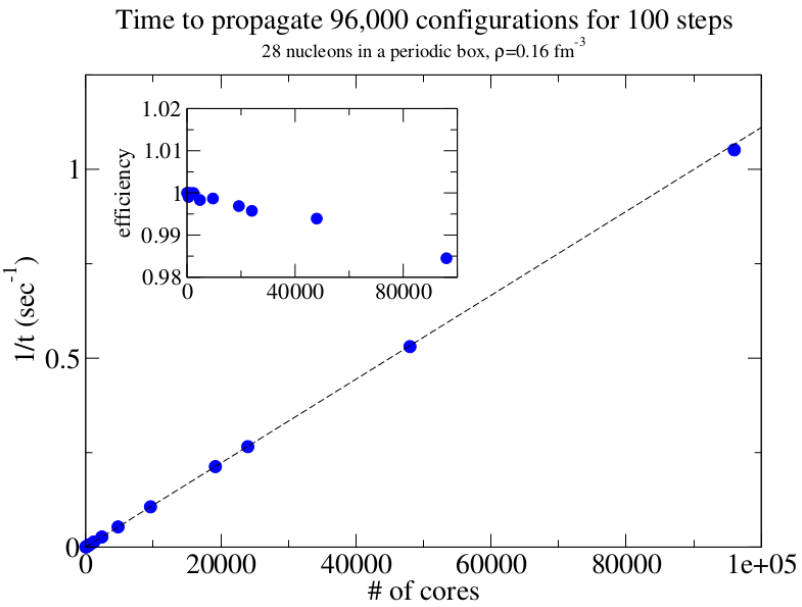

Figure 2.1: Scaling of the AFDMC code obtained on the Cray XC30 machine at NERSC. The inset shows the efficiency as a function of the number of cores, which is higher than 98% for 96,000 cores.

Chapter 3

TWO-DIMENSIONAL FERMI GASES

3.1 Introduction

The study of cold Fermi gases has proven to be a very rich research field, and the investigation of low-dimensional systems has become an active area in this context (Giorgini *et al.* (2008); Bloch *et al.* (2008)). Particularly, the two-dimensional Fermi gas has attracted much interest recently. It was the object of several theoretical investigations (Randeria *et al.* (1989, 1990); Petrov *et al.* (2003); Martikainen and Törmä (2005); Tempere *et al.* (2007); Zhang *et al.* (2008)), but its experimental realization using a highly anisotropic potential, see Fig. 3.1, was a milestone in the study of these systems (Martiyanov *et al.* (2010)).

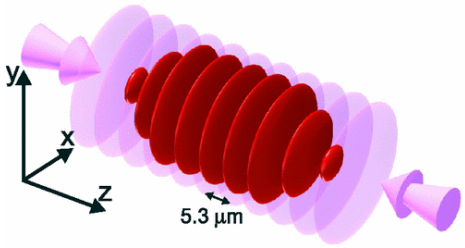

Figure 3.1: The experiment of Martiyanov *et al.* (2010) consisted in a degenerate gas of fermionic atoms which move in two dimensions, while the motion in the third dimension is "frozen" by tight confinement and low temperature. The gas is confined in a optical potential, in the antinodes of a standing optical wave. The isolated clouds of atoms are shown in red, and the standing-wave intensity in purple. Each disk has a radius of approximately 70 μm, while the separation between them is of ≈ 5.3 μm.

Many other studies have been carried out since (Orel *et al.* (2011); Makhalov *et al.* (2014)). Quantum Monte Carlo methods were successfully employed to compute several properties of the BEC-BCS crossover. These methods include diffusion Monte Carlo (Bertaina and Giorgini (2011); Galea *et al.* (2016)), auxiliary-field quantum Monte Carlo (Shi *et al.* (2015)), and lattice Monte Carlo (Anderson and Drut (2015); Rammelmüller *et al.* (2016); Luo *et al.* (2016)). The fact that a fully attractive potential in 2D always supports a bound state, and the ability to vary the interaction strength over the entire BEC-BCS crossover regime offers rich possibilities for the study of these systems.

The presence of quantized vortices is an indication of a superfluid state in both Bose and Fermi systems. In three-dimensional systems, much progress has been made (Bulgac and Yu (2003); Sensarma *et al.* (2006); Simonucci *et al.* (2013); Madeira *et al.* (2016)), including the observation of vortex lattices in a strongly interacting rotating Fermi gas of ^{6}Li (Zwierlein *et al.* (2005)). With the recent progress on the 2D Fermi gases, it seems natural to also extend the theoretical study of vortices to these systems. Interest is further augmented in 2D, where a Berezinksii-Kosterlitz-Thouless transition (Berezinsky (1971); Kosterlitz and Thouless (1972)) could take place at finite temperatures, and pairs of vortices and antivortices would eventually condense to form a square lattice (Botelho and Sá de Melo (2006)).

We are interested in how the properties of a vortex change over the BEC-BCS crossover. Experiments in 3D systems show that the vortex core properties change over the crossover. A theoretical investigation of 2D systems seems pertinent, so that the results can be compared with experiments once they become available.

In this work we focus on ultracold atomic Fermi gases, but it is noteworthy that a duality is expected between neutron matter and superfluid atomic Fermi gases. In 3D, both ultracold atomic gases and low-density neutron matter exhibit pairing gaps

of the order of the Fermi energy (Carlson *et al.* (2013)). In dilute cold gases systems, the effective range r_e between atoms is nearly zero, and the diluteness guarantees that the scattering length a is much larger than the interparticle spacing r_0[1]. Comparison with other systems is meaningful if they also obey $a \gg r_0 \gg r_e$. The scattering length of neutron matter, $a^{nn} \sim -18.5$ fm, is much larger than the interparticle distance and the effective range, $r_e^{nn} \sim 2.7$ fm, such that $|r_e^{nn}/a^{nn}| \approx 0.15$. However, only at very low-densities the effective range is much smaller than the interparticle distance. If we neglect the effects of a finite effective range in the neutron-neutron interaction, cold atoms and neutron matter are universal in the sense that properties depend on the product $k_F a$. Unlike the Fermi atom gases, the possibility of microscopically tuning interactions of neutron-matter is not available. However, we can study neutron pairing by looking at the BCS side of the crossover (Gezerlis and Carlson (2008, 2010)). Vortex properties are also of significant interest in neutron matter (De Blasio and Elgarøy (1999); Yu and Bulgac (2003)) because a significant part of the matter in rotating neutron stars is superfluid, and vortices are expected to appear. Moreover, phases called nuclear pasta, where neutrons are restricted to 1D or 2D configurations, are predicted in neutron stars (Ravenhall *et al.* (1983); Yu and Bulgac (2003)).

We report properties of a single vortex in a 2D Fermi gas. We considered the ground-state to be a disk with hard walls and total angular momentum zero, and the vortex excitation corresponds to each fermion pair having angular momentum $\hbar$. Hopefully, our results will motivate experiments to increase our understanding of vortices in 2D Fermi gases.

This chapter is structured as it follows. In Sec. 3.2 we introduce the methodology employed. In Sec. 3.2.1 we discuss aspects of finite-size fermionic systems, we briefly introduce 2D scattering in Sec. 3.2.2, and Sec. 3.2.3 is devoted to the wave functions

[1]For ^{6}Li, $k_F \sim 1$ μm^{-1}, while the order of magnitude of the range is $\sim$ Å.

employed for the bulk, disk, and vortex systems. Finally, the results are presented in Sec 3.3 and a summary of the work is given in Chapter 5.

3.2 Methods

Previous simulations of vortices in 3D bosonic systems, such as ^{4}He, have often employed a periodic array of counter-rotating vortices, which enables the usage of periodic boundary conditions. In the ^{4}He calculations of Sadd *et al.* (1997), the simulation cell consisted of 300 particles in four counter-rotating vortices. If we had employed a similar methodology, we would need the same number of fermion pairs, i.e., a system with 600 fermions. There are simulations of fermionic systems that have been performed with this number of particles, but the variance required for a detailed optimization is beyond the scope of this work. Instead, we considered a disk geometry similar to the one used in Ortiz and Ceperley (1995) for DMC simulations of the vortex core structure properties in ^{4}He.

3.2.1 Finite-size systems

We are interested in the interacting many-body problem, but it is useful to first consider the non interacting case. In this section we compare the energy of finite-size 2D systems to the results in the thermodynamic limit.

First let us consider the case of N fermions in a square of side L with periodic boundary conditions. The single-particle states are plane waves $\psi_{\boldsymbol{k}_\mathbf{n}}(\boldsymbol{r}) = e^{i\boldsymbol{k}_\mathbf{n}\cdot\boldsymbol{r}}/L$, with wave vector

$$\boldsymbol{k}_\mathbf{n} = \frac{2\pi}{L}(n_x\hat{\boldsymbol{x}} + n_y\hat{\mathbf{y}}). \tag{3.1}$$

The eigenenergies are $E_\mathbf{n} = \hbar^2\boldsymbol{k}_\mathbf{n}^2/2m$, where m is the mass of the fermion. At $T = 0$, all states with energy up to the Fermi energy $\epsilon_F = \hbar^2 k_F^2/2m$, where k_F is the Fermi

wave number, are occupied. A shell structure arises from the fact that different combinations of n_x and n_y in Eq. (3.1) yield the same $|\boldsymbol{k}_{\mathbf{n}}|$. The closed shells occur at total particle number $N = (2, 10, 18, 26, 42, 50, 58, \cdots)$. The free-gas energy of a finite system with N fermions, $E_{FG}^{\text{bulk}}(N)$, is readily calculated by filling the lowest energy states described by Eq. (3.1). In the thermodynamic limit, which corresponds to $N, L \to \infty$ and $n = N/L^2$ held constant, the energy per particle of the free-gas is $E_{\text{FG}} = \epsilon_F/2$ and $k_F = \sqrt{2\pi n}$.

Now let us consider the case of N fermions in a disk of radius $\mathcal{R}$ with a hard wall boundary condition, i.e., the wave function must vanish at $\mathcal{R}$. The single-particle states are

$$\psi_{\nu p}(\rho, \varphi) = \mathcal{N}_{\nu p} J_\nu \left(\frac{j_{\nu p}}{\mathcal{R}} \rho \right) e^{i\nu\varphi}, \tag{3.2}$$

where (ρ, φ) are the usual polar coordinates, $\mathcal{N}_{\nu p}$ is a normalization constant, J_ν are Bessel functions of the first kind, and $j_{\nu p}$ is the p-th zero of J_ν. The quantum number ν can take the values $0, \pm 1, \pm 2, \cdots$ and $p = 1, 2, \cdots$. The corresponding eigenenergies are

$$E_{\nu p} = \frac{\hbar^2}{2m} \left(\frac{j_{\nu p}}{\mathcal{R}} \right)^2. \tag{3.3}$$

This system also presents a shell structure, due to the energy degeneracy of single-particles states with the same $|\nu|$, with shell closures at total particle number $N = (2, 6, 10, 12, 16, 20, 24, 28, 30, 34, \cdots)$. Notice that the energy levels of the bulk system are much more degenerate than the ones of the disk. In practice this means that more shells are needed to describe a disk with a given N. The free-gas energy for the disk, $E_{FG}^{\text{disk}}(N)$, can be calculated analogously to the bulk case using the energy levels of Eq. (3.3). The thermodynamic limit for this case corresponds to $\mathcal{R} \to \infty$ with $n = N/(\pi\mathcal{R}^2)$ held constant, and E_{FG} and k_F go to the same expressions as the bulk ones.

The comparison between the free-gas energy of finite systems in the bulk case and in the disk geometry is not immediate due to the presence of hard walls in the latter. In order to compare the free-gas energy in both geometries, we define

$$E_0^{\rm disk}(N) = E_{FG}^{\rm disk}(N) - \frac{\lambda_s}{2}\sqrt{\frac{n}{\pi N}}, \tag{3.4}$$

in which we separated the total energy $E_{FG}^{\rm disk}(N)$ into a bulk component, $E_0^{\rm disk}(N)$, and a surface term, the second term on the RHS. For further discussions on the functional form of the surface term, see Sec. 3.3.1. Figure 3.2 shows $E_{FG}^{\rm bulk}(N)$ and $E_0^{\rm disk}(N)$, with $\lambda_s = 17.5\ E_{FG}k_F^{-1}$, at the same density. The value of λ_s, within a 0.2% error, was determined by fitting the data for $10 \leqslant N \leqslant 226$ to the functional form of Eq. (3.4).

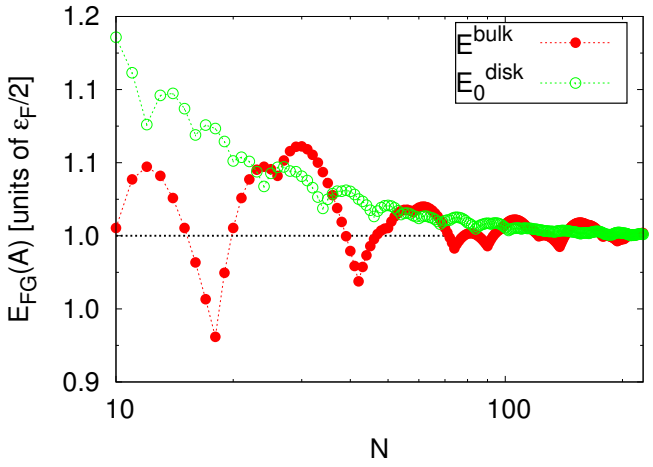

Figure 3.2: Free-gas energy for finite-size systems as a function of the number of particles N, where the dotted lines are drawn to guide the eye. The (red) closed circles denote the energy of the bulk system, $E_{FG}^{\rm bulk}(N)$, and the (green) open circles indicate the bulk energy component in the disk geometry, $E_0^{\rm disk}(N)$, as defined in Eq. (3.4). Local minima in $E_{FG}^{\rm bulk}(N)$ correspond to shell closures.

The disk presents a considerably higher free-gas energy, if compared to the bulk system, due to the presence of hard walls, but the difference between them is rapidly suppressed as we increase the particle number.

3.2.2 Scattering in 2D

Two-body scattering by a finite-range potential $V(r)$ in 2D is described by the Schrödinger equation. We separate the solutions into radial $R(r)$ and angular $P(\phi)$ parts, the latter being a constant for s-wave scattering. The two-body equation for an azimuthally symmetric (s-wave) solution is

$$\left[-\frac{\hbar^2\nabla^2}{2m_r} + V(r)\right] u(r) = \frac{\hbar^2 k^2}{2m_r} u(r), \tag{3.5}$$

where m_r is the reduced mass of the system, and $\hbar^2k^2/2m_r$ is the scattering energy. The scattering length a and effective range r_{eff} can be easily determined from the $k \to 0$ solution of Eq. (3.5), $u_0(r)$, and its asymptotic form y_0. We choose the solution

$$y_0(r) = -\ln\left(\frac{r}{a}\right), \tag{3.6}$$

and we match u_0 and y_0, and their derivatives, outside the range of the potential.

In 2D, the low-energy phase shifts $\delta(k)$, a, and effective range r_{eff}, are related by (Khuri *et al.* (2009))

$$\cot\delta(k) \approx \frac{2}{\pi}\left[\ln\left(\frac{ka}{2}\right) + \gamma\right] + \frac{k^2 r_{\text{eff}}^2}{4}, \tag{3.7}$$

where $\gamma = 0.577\ldots$ is the Euler-Mascheroni constant, and the effective range is defined as (Adhikari *et al.* (1986))

$$r_{\text{eff}}^2 = 4\int_0^\infty (y_0^2(r) - u_0^2(r))r\ dr. \tag{3.8}$$

Equation (3.7) is often called the shape-independent approximation because it guarantees that a broad range of well-chosen potentials can be constructed to describe low-energy scattering.

We consider the modified Poschl-Teller potential

$$V(r) = -v_0 \frac{\hbar^2}{m_r} \frac{\mu^2}{\cosh^2(\mu r)}, \tag{3.9}$$

where v_0 and μ can be tuned to reproduce the desired a and r_{eff}.

Bound-states occur for purely attractive potentials for any strength in 2D. If we continually increase the depth of $V(r)$, a will eventually reach zero, and then it diverges to $+\infty$ when a new bound-state is created. The binding energy of the pair is given by

$$\epsilon_b = -\frac{4\hbar^2}{ma^2 e^{2\gamma}}. \tag{3.10}$$

We chose values of v_0 and μ such that only one bound-state is present, and $k_F r_{\text{eff}}$ is held constant at 0.006 (Galea *et al.* (2016)). This choice guarantees that the systems studied in this work are in the dilute regime, since $r_0 \gg r_{\text{eff}}$, where $r_0 = 1/\sqrt{\pi n}$ is of order of the interparticle spacing.

The Hamiltonian of the two-component Fermi gas is given by

$$H = -\frac{\hbar^2}{2m} \left[\sum_{i=1}^{N_\uparrow} \nabla_i^2 + \sum_{i=j'}^{N_\downarrow} \nabla_{j'}^2 \right] + \sum_{i,j'} V(r_{ij'}), \tag{3.11}$$

with $N = N_\uparrow + N_\downarrow$, and $V(r_{ij'})$ given by Eq. (3.9). The DMC method projects the lowest energy state of H from an initial state ψ_T, obtained from variational Monte Carlo simulations, see Sec. (2.3).

We carefully optimized the trial wave function ψ_T, since it is used in three ways: an approximation of the ground-state in the VMC calculations, as an importance function, and to give the nodal surface for the fixed-node approximation. The variational parameters in Eqs. (3.18), (3.21), and (3.23) were determined using the stochastic reconfiguration method (Casula *et al.* (2004)), see Appendix A.1. Expectation values of operators that do not commute with the Hamiltonian, for example the current and density, were calculated using extrapolated estimators, Eq. (2.41).

3.2.3 *Wave functions*

The BCS wave function, which describes pairing explicitly, has been successfully used in a variety of strongly interacting Fermi gases systems, such as: 3D (Carlson *et al.* (2003)) and 2D (Galea *et al.* (2016)) bulk systems, vortices in the unitary regime (Madeira *et al.* (2016)), two-component mixtures (Gezerlis *et al.* (2009); Gandolfi (2014)), and many other systems. This wave function, projected to a fixed number of particles N (half with spin-up and half with spin-down), can be written as the antisymmetrized product (Leggett (1975); Bouchaud, J.P. *et al.* (1988))

$$\psi_{\mathrm{BCS}}(\mathbf{R}, S) = \mathcal{A}[\phi(\boldsymbol{r}_1, s_1, \boldsymbol{r}_2, s_2)\phi(\boldsymbol{r}_3, s_3, \boldsymbol{r}_4, s_4)\ldots\phi(\boldsymbol{r}_{N-1}, s_{N-1}, \boldsymbol{r}_N, s_N)], \quad (3.12)$$

where $\mathbf{R}$ is a vector containing the particle positions $\boldsymbol{r}_i$, S stands for the spins s_i, and ϕ is the pairing function, which is given by

$$\phi(\boldsymbol{r}, s, \boldsymbol{r}', s') = \tilde{\phi}(\boldsymbol{r}, \boldsymbol{r}')\left[\langle s\ s'|\uparrow\downarrow\rangle - \langle s\ s'|\downarrow\uparrow\rangle\right], \quad (3.13)$$

where we have explicitly included the spin part to impose singlet pairing. The assumed expressions for $\tilde{\phi}$ depend on the system being studied (see Secs. 3.2.3, 3.2.3, and 3.2.3). Since neither the Hamiltonian or any operators in the quantities we calculate flip the spins, the results are equivalent to viewing spin-up and spin-down as distinguishable particles. Thus, we adopt hereafter the convention of primed indexes to denote spin-down particles and unprimed ones to refer to spin-up particles. Equation (3.12) reduces to

$$\psi_{\mathrm{BCS}}(\mathbf{R}, S) = \mathcal{A}[\phi(\boldsymbol{r}_1, s_1, \boldsymbol{r}_{1'}, s_{1'})\phi(\boldsymbol{r}_2, s_2, \boldsymbol{r}_{2'}, s_{2'})\ldots\phi(\boldsymbol{r}_{N/2}, s_{N/2}, \boldsymbol{r}_{N/2'}, s_{N/2'})], \quad (3.14)$$

where the antisymmetrization is over spin-up and/or spin-down particles only. This wave function can be calculated efficiently as a determinant (Gandolfi *et al.* (2009)).

In addition to fully paired systems, it is also possible to simulate systems with unpaired particles (Carlson *et al.* (2003)), described by single particle states $\Phi(\boldsymbol{r})$. For q pairs, u spin-up, and d spin-down unpaired single particles states, $N = 2q + u + d$, we can rewrite Eq. (3.14) as

$$\psi_{\rm BCS}(\mathbf{R}, S) = \mathcal{A}[\phi(\boldsymbol{r}_1, s_1, \boldsymbol{r}_{1'}, s_{1'}) \cdots \phi(\boldsymbol{r}_q, s_q, \boldsymbol{r}_{q'}, s_{q'}) \Phi_{1\uparrow}(\boldsymbol{r}_{q+1}) \cdots \Phi_{u\uparrow}(\boldsymbol{r}_{q+u}) \\ \Phi_{1\downarrow}(\boldsymbol{r}_{(q+1)'}) \cdots \Phi_{d\downarrow}(\boldsymbol{r}_{(q+d)'})]. \quad (3.15)$$

We also included a two-body Jastrow factor $f(r_{ij'})$, $r_{ij'} = |\boldsymbol{r}_i - \boldsymbol{r}_{j'}|$, which accounts for correlations between antiparallel spins. It is obtained from solutions of the two-body Schröedinger equation

$$\left[-\frac{\hbar^2 \nabla^2}{2m_r} + V(r)\right] f(r < d) = \lambda f(r < d), \quad (3.16)$$

with the boundary conditions $f(r > d) = 1$ and $f'(r = d) = 0$, where d is a variational parameter, and λ is adjusted so that $f(r)$ is nodeless. The total trial wave function is written as

$$\psi_{\rm T}(\mathbf{R}, S) = \prod_{i,j'} f(r_{ij'}) \psi_{\rm BCS}(\mathbf{R}, S). \quad (3.17)$$

Bulk system

The assumed form of the pairing function for the bulk case is the same as Carlson *et al.* (2003),

$$\tilde{\phi}_{\rm bulk}(\boldsymbol{r}, \boldsymbol{r}') = \sum_{n=1}^{n_c} \alpha_n e^{i\boldsymbol{k}_{\mathbf{n}} \cdot (\boldsymbol{r} - \boldsymbol{r}')} + \tilde{\beta}(|\boldsymbol{r} - \boldsymbol{r}'|), \quad (3.18)$$

where α_n are variational parameters, and contributions from momentum states up to a level n_c are included.

Contributions with $n > n_c$ are included through the $\tilde{\beta}$ function given by

$$\tilde{\beta}(r) = \begin{cases} \beta(r) + \beta(L-r) - 2\beta(L/2) & \text{for } r \leqslant L/2 \\ 0 & \text{for } r > L/2 \end{cases} \tag{3.19}$$

with

$$\beta(r) = [1 + cbr][1 - e^{-dbr}]\frac{e^{-br}}{dbr}, \tag{3.20}$$

where $r = |\boldsymbol{r} - \boldsymbol{r}'|$ and b, c, and d are variational parameters. This functional form of $\beta(r)$ describes the short-distance correlation of particles with antiparallel spins. We consider $b = 0.5\ k_F$, $d = 5$, and c is adjusted so that $\partial\tilde{\beta}/\partial r = 0$ at $r = 0$.

Disk

The pairing function for the disk geometry is constructed using the single-particle orbitals of Eq. (3.2). Each pair consists of one single-particle orbital coupled with its time-reversed state. This ansatz has been used before in the 3D system (Madeira *et al.* (2016)), a cylinder with hard walls, and the form presented here is analogous to that one if we disregard the z components. We supposed the pairing function to be

$$\tilde{\phi}_{\text{disk}}(\boldsymbol{r}, \boldsymbol{r}') = \sum_{n=1}^{n_c} \tilde{\alpha}_n \mathcal{N}_{\nu p}^2 J_\nu \left(\frac{j_{\nu p}}{\mathcal{R}}\rho\right) J_\nu \left(\frac{j_{\nu p}}{\mathcal{R}}\rho'\right) e^{i\nu(\varphi - \varphi')} + \bar{\beta}(\boldsymbol{r}, \boldsymbol{r}'), \tag{3.21}$$

where the $\tilde{\alpha}_n$ are variational parameters, and n is a label for the disk shells, such that different states with the same energy are associated with the same variational parameter, as in the plane wave expansion of Eq. (3.18).

In principle the single-particle orbitals in Eq. (3.21) form a complete set. To speed convergence, we introduce a cutoff and we assume that higher momenta contributions

are described by the $\bar{\beta}$ function. It is similar to $\tilde{\beta}$ employed in the bulk system, but we modify it to ensure the hard wall boundary condition is met,

$$\bar{\beta}(\boldsymbol{r},\boldsymbol{r'}) = \begin{cases} \mathcal{N}_{01}^2 J_0\left(\frac{j_{01}\rho}{\mathcal{R}}\right) J_0\left(\frac{j_{01}\rho'}{\mathcal{R}}\right) \times \\ [\beta(r)+\beta(2\mathcal{R}-r)-2\beta(\mathcal{R})] & \text{for } r \leqslant \mathcal{R} \\ 0 & \text{for } r > \mathcal{R} \end{cases} \tag{3.22}$$

and β has the same expression as the bulk case, Eq. (3.20).

Vortex

The vortex excitation is accomplished by considering pairing orbitals which are eigenstates of L_z with eigenvalues $\pm\hbar$. This is achieved by coupling single-particle states with angular quantum numbers differing by one. In this case we used pairing orbitals of the form

$$\begin{aligned} \tilde{\phi}_{\text{vortex}}(\boldsymbol{r},\boldsymbol{r'}) = \sum_{n=1}^{n_c} \bar{\alpha}_n \mathcal{N}_{\nu p}\mathcal{N}_{\nu-1;p} \Bigg\{ J_\nu\left(\frac{j_{\nu p}}{\mathcal{R}}\rho\right) J_{\nu-1}\left(\frac{j_{\nu-1;p}}{\mathcal{R}}\rho'\right) e^{i(\nu\varphi-(\nu-1)\varphi')} \\ + J_\nu\left(\frac{j_{\nu p}}{\mathcal{R}}\rho'\right) J_{\nu-1}\left(\frac{j_{\nu-1;p}}{\mathcal{R}}\rho\right) e^{i(\nu\varphi'-(\nu-1)\varphi)} \Bigg\}, \end{aligned} \tag{3.23}$$

where n is a label for the vortex shells, and $\bar{\alpha}$ are variational parameters. The largest contribution is assumed to be from states with the same quantum number p for the radial part (Madeira *et al.* (2016)). Equation (3.23) is symmetric under interchange of the prime and unprimed coordinates, as required for singlet pairing.

The $\bar{\beta}$ function of Eq. (3.22) is not suited to describe the vortex state because it is an eigenstate of L_z with angular momentum zero. We tried different functional forms that had the desired angular momentum eigenvalue, but none of them resulted in a significant lower total energy. Thus, we chose to employ only the terms in Eq. (3.23). As before, the functions in the absence of cutoff form a complete set.

3.3 Results

This section is structured as it follows. Sec. 3.3.1 contains the ground-state energies in the disk geometry and discussions of size-effects. In Sec. 3.3.2 we present the vortex excitation energy. The determination of the crossover region is done in Sec. 3.3.3. Density profiles of the vortex and ground-state systems are shown in Sec. 3.3.4. Properties of the vortex core are discussed in Sec. 3.3.5.

We define the interaction strength $\eta \equiv \ln(k_F a)$. Large values of η correspond to the BCS side of the crossover, while small η are on the BEC side. We probed $0.0 \leqslant \eta \leqslant 1.5$, which encompasses the crossover region (see Sec. 3.3.3). For all systems the number density is $n = N/(\pi\mathcal{R}^2)$, and $k_F = \sqrt{2N}/\mathcal{R}$.

3.3.1 Ground-state energy and size-effects

We used the pairing function of Eq. (3.18), and $N = 26$, to calculate the ground-state energy per particle of the bulk systems. Our results (see Table 3.1) are in agreement with previous DMC calculations (Galea *et al.* (2016)).

Previous DMC simulations of 2D Fermi gases found that $N = 26$ is well suited to simulate bulk properties of systems in the region studied here (Galea *et al.* (2016)). However, the disk geometry presents more intricate size-dependent effects. We investigated how the ground-state energy depends on the disk radius $\mathcal{R}$. In the thermodynamic limit, $\mathcal{R} \to \infty$, the energy per particle should go to the bulk value. Since our system has hard walls, the energy has a dependence on the "surface" of the disk. Including this surface term, the energy per particle can be fit to

$$E_{\text{disk}}(\mathcal{R}) = E_0 + \frac{\lambda_s}{2\pi\mathcal{R}}, \tag{3.24}$$

where E_0 and λ_s are constants related to the bulk and surface terms.

Table 3.1: Comparison between the ground-state energy per particle of the bulk ($E_{\rm bulk}$) and disk systems as a function of the interaction strength η. The parameters E_0 and λ_s, see Eq. (3.24), are related to our assumption of the functional form of the ground-state energy per particle in the disk geometry.

η	$E_{\rm bulk}$ $[E_{FG}]$	E_0 $[E_{FG}]$	λ_s $[E_{FG}k_F^{-1}]$
0.00	-2.3740(3)	-2.32(3)	6(2)
0.25	-1.3316(3)	-1.31(3)	8(2)
0.50	-0.6766(2)	-0.65(2)	8(1)
0.75	-0.2562(2)	-0.25(2)	11(1)
1.00	0.0233(2)	0.03(1)	11(1)
1.25	0.2149(2)	0.22(2)	12(1)
1.50	0.3523(2)	0.34(1)	13(1)

A few words about Eq. (3.24) are in order. The relation between the thermodynamic properties of a confined fluid and the shape of the container where it is confined has been an active field of study. Our choice was inspired by functional forms (see for example König *et al.* (2004)) where, aside from the constant term, thermodynamical properties are expressed as functions of the various curvatures of the container. The next correction to this functional form of the energy per particle would include a term proportional to $\mathcal{R}^{-2}$. We found that the inclusion of such a term does not significantly improve our description of the ground-state energy.

In order to determine the number of particles necessary to simulate systems in the disk geometry, with controllable size effects, we performed simulations with $26 \leqslant N \leqslant 70$, and all particles paired, i.e., only even values of N.

The dependence of E_0 with the system size was investigated by fitting our data using Eq. (3.24) for different intervals of $\mathcal{R}$ or, equivalently, different intervals of N. We found that fitting the data for $58 \leqslant N \leqslant 70$ resulted in a good agreement between E_{bulk} and E_0, that is, we were able to separate the bulk portion of the energy from the hard wall contribution in the disk geometry. The resulting parameters of the fitting procedure are summarized in Table 3.1, and Fig. 3.3 shows the energy per particle as a function of $\mathcal{R}$ for all interaction strengths studied in this work.

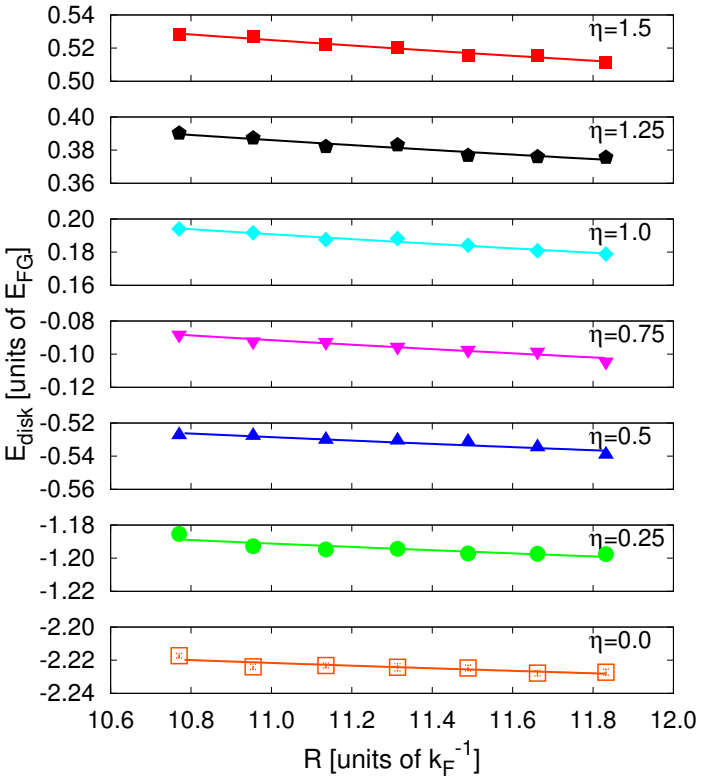

Figure 3.3: Ground-state energy per particle E_{disk} as a function of the disk radius $\mathcal{R}$ for several interaction strengths. The curves correspond to the assumed functional form of Eq. (3.24), with the parameters given in Table 3.1. Error bars are smaller than the symbols.

The E_0 values agree with the bulk energies within the error bars, except for $\eta = 0$ and $\eta = 0.5$ (however the differences between the values are less than 2% and 4%, respectively). As it can be seen in Table 3.1, the typical uncertainty in E_0 is of order 0.01 E_F, independent of the interaction strength. Thus the relative error can be quite large for systems where the absolute value of the bulk energy is small, as it is observed for $\eta = 1.0$. This is an improvement if compared to a similar DMC calculation in 3D (Madeira *et al.* (2016)) which used the same procedure to calculate the ground-state energy per particle of a unitary Fermi gas, where the discrepancy between the result and the known bulk value was $\approx 30\%$.

We point out that this method is not intended to be a precise calculation of the bulk energy of these systems. Instead, it is a way for us to determine the minimum number of particles needed to simulate systems in the disk geometry with controllable size effects. If we had naively assumed that the same number of particles used in bulk calculations would suffice, $N = 26$, then we simply could not rely on the results. In our simulations with $26 \leqslant N \leqslant 38$ the discrepancies between E_0 and E_{bulk} were as large as 50%, and in some cases the uncertainty in λ_s was bigger than the value itself. Results with $58 \leqslant N \leqslant 70$ are much more well-behaved, and they are within computational capabilities.

It is also noteworthy to mention that the energy contribution of the surface term, due to the presence of hard walls, is more significant for the BCS side than in the BEC limit (see the λ_s values in Table 3.1). This is expected, since the largest energy contribution in the BEC side should be from the binding energy of the pairs, Eq. (3.10), and they are smaller than the BCS pairs so that surface effects are smaller. One of our goals is to obtain the vortex excitation energy, which is the difference between the vortex and the ground-state energies. Since both systems have hard walls, we expect that the surface effects will tend to cancel.

3.3.2 *Vortex excitation energy*

The energy per particle of the vortex system is obtained using the pairing functions of Eq. (3.23). The vortex excitation energy is given by the difference between the energy of the vortex and ground-state systems, for the same number of particles. We performed simulations with $58 \leqslant N \leqslant 70$ and averaged the results.

In Fig. 3.4 we show the vortex excitation energy per particle as a function of the interaction strength. The energy necessary to excite the system to a vortex state increases as we move from the BCS to the BEC limit. The inset shows the vortex and ground-state energies per particle for $\eta = 1.5$, although the other interaction strengths display the same qualitative behavior.

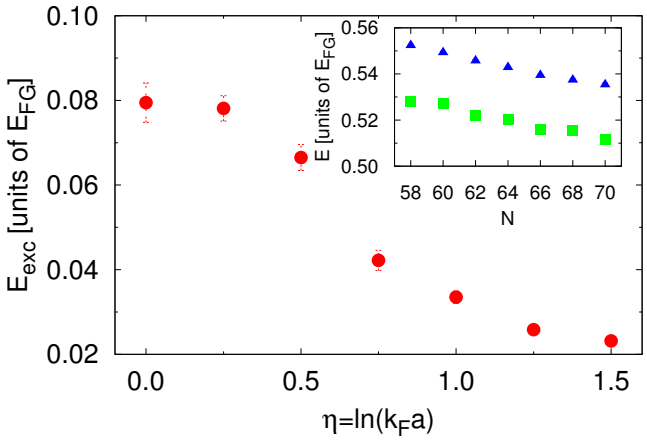

Figure 3.4: Vortex excitation energy per particle $E_{\rm exc}$ as a function of the interaction strength η. The inset shows the ground-state (squares) and vortex (triangles) energies per particle as a function of the number of particles N for $\eta = 1.5$.

3.3.3 *Crossover region*

In 2D, the BCS limit corresponds to $k_F a \gg 1$ and the BEC limit to $k_F a \ll 1$, however unlike 3D where the unitarity is signaled by the addition of a two-body bound

state, there is no equivalent effect with two-body sector in 2D. Nevertheless, we can determine the interaction strength for which we can add a pair to the system with zero energy cost (note that the chemical potential is not zero for the unitary gas in 3D). The chemical potential μ can be estimated as

$$\mu = \left.\frac{\partial E}{\partial N}\right|_{\text{Even } N}, \tag{3.25}$$

for each interaction strength, where the even number condition implies that all particles are paired. For each value of η we used a finite difference formula to evaluate Eq. (3.25), for $58 \leqslant N \leqslant 70$ (see Fig. 3.5).

We found that $\mu = 0$ at $\eta \approx 0.90$ for the ground-state of the disk. Previous DMC simulations of 2D bulk systems (Galea *et al.* (2016)) found that the chemical potential changes sign at $\eta \approx 0.65$. Although the results differ, most probably due to the different geometry employed in this work, it is safe to assume that the interaction strength interval $0 \leqslant \eta \leqslant 1.5$ encompasses the BEC-BCS crossover region. The chemical potential of the vortex state is higher than the ground-state, as expected, thus $\mu = 0$ is at a smaller interaction strength, $\eta \approx 0.85$.

3.3.4 Density profile

We calculated the density profile $\mathcal{D}(\rho)$ along the radial direction ρ for both the vortex and ground-state systems. The normalization is such that

$$\int \mathcal{D}(\rho) d^2r = 1, \tag{3.26}$$

where the integral is performed over the area of the disk. The results are obtained using the extrapolation procedure of Eq. (2.41), which combines both VMC and DMC runs. It is noteworthy to point out that, although the densities observed in VMC and DMC simulations differ, they are much closer than previous results in 3D (Madeira

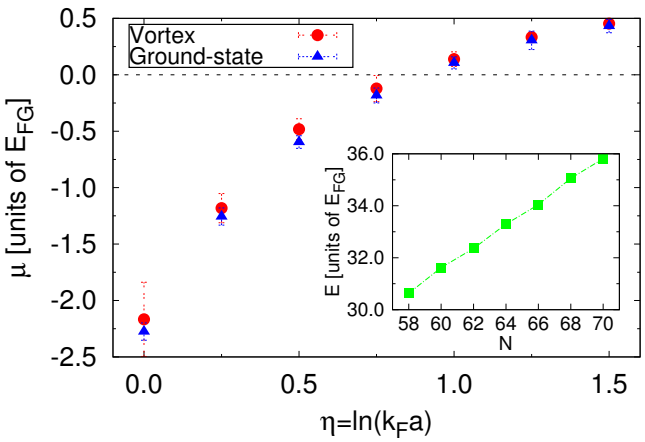

Figure 3.5: Chemical potential of the ground-state (triangles) and vortex (circles) as a function of the interaction strength. The chemical potential changes sign at $\eta \approx 0.90$ for the ground-state, and $\eta \approx 0.85$ for the vortex state. In the inset we show the total energy as a function of the number of particles for the ground-state of $\eta = 1.5$. Other interaction strengths with positive (negative) μ have positive (negative) slopes.

et al. (2016)). In that calculation it was needed to explicitly include a one-body term in the wave function to maximize the density overlap between DMC and VMC runs, whereas in this work no such term was employed.

Figure 3.6 shows the density profile of both the vortex and ground-state systems for $N = 70$ and $\eta = 1.5$. The oscillations in the density profiles are much more pronounced than in a similar DMC calculation of a unitary Fermi gas in 3D (Madeira *et al.* (2016)). In this 3D calculation a cylindrical geometry was employed, with hard walls and periodic boundary conditions along the axis of the cylinder. The density profiles were obtained by averaging the results over the z direction of the axis of the cylinder, we therefore expect more fluctuations in 2D where the particles are confined to a plane. For the ground-state, the density oscillations are surface effects. They

are present in both the interacting and non-interacting systems, as it can be seen in Fig. 3.6.

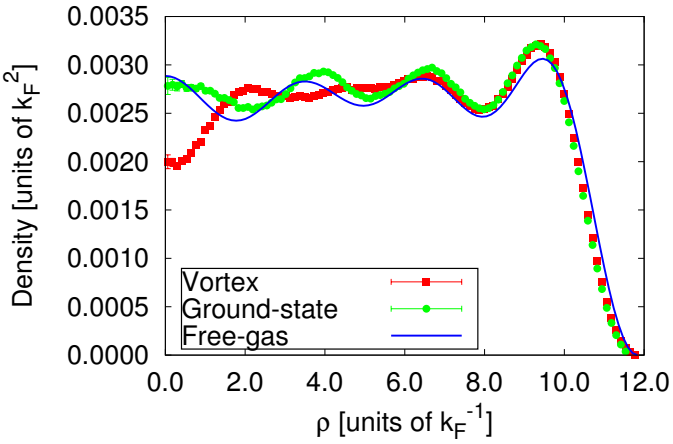

Figure 3.6: Density profile along the radial direction ρ of the vortex (red squares) and ground-state (green circles) for $N = 70$ and $\eta = 1.5$. Although there is a density suppression at the vortex core of $\approx 30\%$, the density is non-zero at the center of the disk. We also plot the analytical result for the ground-state density of the free- gas in a disk (blue curve), which presents oscillations due to the presence of hard-walls.

In Fig. 3.7 we show the density profiles of the other interaction strengths studied in this work, $0 \leqslant \eta \leqslant 1.25$. We found that the density depletion at the vortex core goes from $\approx 30\%$ at $\eta = 1.5$ to a completely depleted core at $\eta \leqslant 0.25$.

The regions close to the walls exhibit a characteristic behavior due to the hard wall condition we imposed, as it can be seen in Figs. 3.6 and 3.7. In order to estimate the number of particles outside this region, we can define the particle number a distance R from the center of the disk as

$$\mathcal{N}(R) = N \int_0^{2\pi} d\varphi \int_0^R d\rho \; \rho \; \mathcal{D}(\rho). \tag{3.27}$$

For the case of Figs. 3.6 and 3.7 where $N = 70$, if we set $R \sim 8 \; k_F^{-1}$, $\mathcal{N}$ is approximately between 40 and 45 for the ground-state, and between 35 and 40 for the vortex

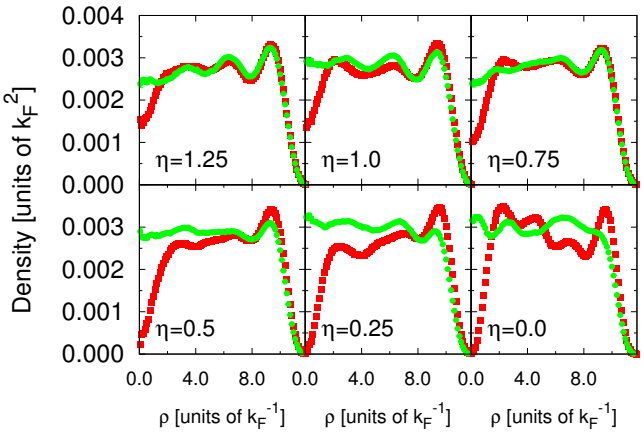

Figure 3.7: Density profile along the radial direction ρ of the vortex (red squares) and ground-state (green circles) for $N = 70$ and $0 \leqslant \eta \leqslant 1.25$. It is interesting to observe that the density at the vortex core diminishes as we go from the BCS to the BEC limit, and at $\eta \leqslant 0.25$ the core is completely depleted. This can be understood if we consider the pair sizes, which correspond to a few k_F^{-1} in the BCS side, and tightly bound molecules in BEC limit. Thus, in the BCS side, one of the fermions in a pair can be near $\rho = 0$ while the center of mass of the pair rotates around the axis. The same is not possible in the BEC limit of tightly bound pairs, hence the depleted core.

systems. Hence the number of particles in this regime is larger than the usual value of $N = 26$ employed in bulk systems (Galea *et al.* (2016)).

Additionally, we performed simulations of the vortex systems with an odd number of particles, i.e., one unpaired particle was added to a fully paired system, Eq. (3.15) with $q = 34$, $u = 1$, and $d = 0$. We set its angular momentum to zero, Eq. (3.2) with $\nu = 0$ and $p = 1$. In the BEC limit we observed a non-vanishing density at the center of the disk, which suggests that the unpaired particle fills the empty vortex core region. On the other hand, in the BCS limit the density close to the wall increased, while the density at the origin was unchanged. We chose a qualitative discussion of

this phenomenon because the required variance for a detailed optimization is beyond the scope of this work. Future calculations should include quantities such as the one-body density matrix, which may contribute to an accurate quantitative approach.

3.3.5 Vortex core size

The probability current density operator can be written as

$$\mathbf{J}(\boldsymbol{r}) = \frac{1}{2N}\sum_{j=1}^{N}\left[\mathbf{v}_j\delta^2(\boldsymbol{r}-\boldsymbol{r}_j) + \delta^2(\boldsymbol{r}-\boldsymbol{r}_j)\mathbf{v}_j\right], \tag{3.28}$$

where the velocity operator is $\mathbf{v}_j = \boldsymbol{p}_j/m \to -i\hbar\nabla_j/m$. We are interested in the angular component as a function of the radial coordinate, $J_\varphi(\rho)$, because the position of its maximum can be used as an estimate of the vortex core size, $J_{\max} \equiv J_\varphi(\rho = \xi)$.

We followed the extrapolation procedure of Eq. (2.41). Figure 3.8 shows $J_\varphi(\rho)$ for $N = 70$ and $0 \leqslant \eta \leqslant 1.5$. The maximum of the current increases as we go from the BCS to the BEC limit, its value at the BEC side, $\eta = 0$, being more than twice $J_{\max}$ at the BCS side, $\eta = 1.5$. The position of the maximum is between $\xi = 1.7$ and $1.8\ k_F^{-1}$ at the BCS side of the crossover, i.e., $0.75 \leqslant \eta \leqslant 1.5$; at the BEC side, $\eta = 0.25$ and 0.5, $\xi \sim 1.6\ k_F^{-1}$. The case $\eta = 0$ moves away from the trend of a smaller core as we go from the BCS to the BEC limit, with $\xi = 2.0\ k_F^{-1}$. It is unclear if ξ or $J_{\max}$ depend on the disk radius $\mathcal{R}$, because the $\mathcal{R}$ values are closely spaced for $58 \leqslant N \leqslant 70$, and no significant difference was observed in the maximum as we varied N. Nevertheless, the relative results contribute to understanding how the vortex core evolves over the BEC-BCS crossover.

The wave function that we employed for the vortex state is an eigenstate of the total angular momentum operator. Since this operator commutes with the Hamiltonian, the diffusion procedure does not change the eigenvalue of the state. In addition, the calculation of the probability current density operator allowed us to verify that

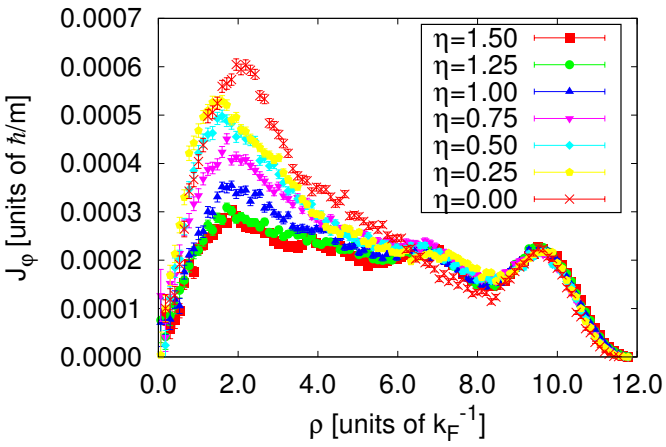

Figure 3.8: Angular component of the probability current J_φ as a function of the radial coordinate ρ for several interaction strengths η. The position of its maximum provides an estimate of the vortex core size.

the vortex corresponds to a $N\hbar/2$ total angular momentum state in a straightforward way. The angular momentum can be written as

$$\mathbf{L} = m \int (\boldsymbol{r} \times \mathbf{J}) d^2\boldsymbol{r}, \tag{3.29}$$

and the component of interest is

$$L_z = 2\pi m \int \rho^2 J_\varphi(\rho) d\rho. \tag{3.30}$$

In our definition of the probability current density operator, we divide by the number of particles N, see Eq. (3.28). Thus, the evaluation of L_z using Eq. (3.30) should yield $\hbar/2$. We verified that, for all interaction strengths, this is in agreement with our simulations.

Chapter 4

QUANTUM MONTE CARLO FOR DYNAMICAL PIONS AND NUCLEONS

Modern nuclear theory is characterized by a series of attempts to rigorously bridge the gap between quarks and gluons, the degrees of freedom of quantum chromodynamics (QCD), and the confined phase in which massive particles such as mesons and baryons can be regarded as the constituents of matter. Nuclear effective field theories (EFTs) are employed to connect QCD to low-energy nuclear observables. EFTs exploit the separation between the "hard" (M, typically the nucleon mass) and "soft" (Q, typically the exchanged momentum) momentum scales. The active degrees of freedom at soft scales are hadrons whose interactions are consistent with QCD. Effective potentials and currents are derived in a systematic expansion in Q/M from the most general Lagrangian constrained by the QCD symmetries. Chiral-EFT, which is best suited to describe processes characterized by $Q \simeq m_\pi$, exploits the (approximate) chiral symmetry of QCD and its pattern of spontaneous symmetry breaking to derive consistent nuclear potentials and currents, and to estimate their uncertainties (Epelbaum *et al.* (2009); Machleidt and Entem (2011)).

Potentials and electroweak currents derived within chiral-EFT are the main input to "ab-initio" many-body methods that are aimed at solving the many-body Schrödinger equation associated with the nuclear Hamiltonian (Barrett *et al.* (2013); Epelbaum *et al.* (2011); Hagen *et al.* (2014); Hergert *et al.* (2016); Carbone *et al.* (2013); Carlson *et al.* (2015b)). These schemes rely on the assumption that processes like the one meson exchange are well approximated by an instantaneous interaction, and that the meson degrees of freedom can be integrated out and their contribution is encoded in nuclear potentials and electroweak currents, determining their low-

momentum behavior. Not much attention has been devoted so far to the development of techniques capable of including mesonic degrees of freedom in these many-body calculations. There are several reasons for this choice. The main one is that effects arising from not assuming an instantaneous interaction are believed to be unessential for the derivation of nuclear potentials. Without such assumption, many-body interactions would automatically be generated already at leading order when integrating out the meson fields. The fact that, when neglecting dynamical effects in the meson fields, three- and many-body interactions appear at next-to-next-to leading order (N2LO) suggests that such effects can be considered to be sub-leading at any order. However, such assumptions have never been rigorously tested in ab-initio scheme for a many-nucleon system.

Most of the progress to account for explicit pions into nuclear EFT has been made so far by using lattice methods. Whilst the inclusion of pion fields into the Lagrangians is straightforward, dynamical pions bring noise and sign problems in lattice Monte Carlo calculations (Hjorth-Jensen *et al.* (2017)). One alternative approach is to use static pion auxiliary fields (Borasoy *et al.* (2007); Lee (2009)), where time derivatives are neglected, and thus pions couple to nucleons only through spatial derivatives. Since these pion fields are instantaneous, this eliminates the self-energy diagrams responsible for mass renormalization.

It is noteworthy to point out that there is a condensed matter analog to the axial-vector coupling between one nucleon and the pions, the polaron (Feynman (1955)). However, the coupling between the electron and the phonons is scalar, and the bosonic degrees of freedom can be integrated out explicitly. Quantum Monte Carlo methods have been successful at tackling both problems (Carlson and Schmidt (1992)).

In this dissertation, we devise a QMC framework in which both relativistic pions and nonrelativistic nucleons are explicitly included in the quantum-mechanical states

of the system. From a given order chiral-EFT Lagrangian, the corresponding Hamiltonian is derived, and the pion fields are expressed in the Schrödinger representation. The nuclear structure problem is written in terms of the modes of the relativistic pion field, and of the position and spin-isospin degrees of freedom of the nucleons. QMC techniques are employed to accurately solve the corresponding Schrödinger equation, which is equivalent to summing all Feynman diagrams originating from a given order of the chiral-EFT Lagrangian. Resummation techniques are already employed in chiral-EFT. The nucleon-nucleon (NN) system at low angular momenta is characterized by a shallow bound state, the deuteron, and large scattering lengths, which prevents the applicability of standard chiral perturbation theory. Weinberg suggested to use perturbation theory to calculate the irreducible diagrams defining the NN potential, and apply it in a scattering equation to obtain the NN amplitude (Weinberg (1990)). Solving the scattering equation corresponds to summing all diagrams with purely nucleonic intermediate states (Machleidt and Entem (2011)). Diagrammatic resummation in chiral-EFT is also needed to describe resonances in pion-pion scattering that cannot be obtained in perturbation theory to any finite order (Nieves and Arriola (2000)).

Before moving to larger systems, there are several non-trivial questions arising when including pions in a QMC calculation, that need to be addressed already for the one and two nucleon cases. One of the major issues is the assessment of finite size effects, since our calculations are necessarily limited to nucleons and pions lying in a box of side L with periodic boundary conditions. This naturally introduces a infrared cutoff dependence which, together with the ultraviolet cutoff we employ, affects the pion-nucleon interaction.

In the single-nucleon sector, we study the energy-shift of the nucleon mass as a function of the momentum cutoff. We also compute the pion cloud density and

momentum distributions. In the NN sector, we first verified that our results for two static nucleons correctly reduce to the one-pion exchange potential at sufficiently large separation distance. We then fit the low-energy constants associated to the contact terms of the leading-order (LO) chiral-EFT Lagrangian to describe the deuteron and two neutrons in a finite volume.

This chapter is a summary of our formalism, and the steps used to derive it, that allows for the inclusion of explicit pion degrees of freedom in quantum Monte Carlo simulations of nucleon systems. In Sec. 4.1, after a brief introduction on chiral effective field theory, we derive the leading order chiral Lagrangian, in which only nucleons and pions degrees of freedom are included, in the heavy baryon framework. Expressions for the pion field and related quantities are provided in Sec. 4.2. In Sec. 4.3 we derive expressions for the Hamiltonians and wave functions needed for A-nucleon simulations. Sec. 4.4 includes a lowest order nonrelativistic calculation of the self-energy of the nucleon in a box, and analytical expressions for pion derivatives. The one pion exchange potential is derived in Sec. 4.5. Physical two nucleon systems, namely the deuteron and two neutrons, are studied in Sec. 4.6. In Sec. 4.7 we comment on technical aspects of the implementation of one- and two-body operators, as well as the basis employed in our code. Finally, the results are presented in Sec. 4.9 and an outlook of the work is given in Chapter 5.

4.1 Chiral effective field theory

In this section we follow the treatment of Machleidt and Entem (2011) to show how nuclear forces emerge from low-energy quantum chromodynamics via chiral effective field theory. One of the major open problems in nuclear physics is how to construct a nucleon-nucleon (NN) interaction potential from first principles. The first attempts were based on Yukawa's seminal idea of a description based on pion exchanges. While

the one pion exchange (OPE) turned out to be useful in explaining NN scattering data and deuteron properties, multi-pion exchange could not be resolved in a satisfactory way. Hence the "pion theories" of the 1950's were deemed failures, but the reason is understood today: pion dynamics is constrained by chiral symmetry, which was unknown at the time.

A major breakthrough occurred when the concept of an EFT was applied to low-energy QCD. Weinberg suggested that one has to write the most general Lagrangian consistent with the assumed symmetry principles, in particular the broken chiral symmetry of QCD. At low energy, the effective degrees of freedom are pions and nucleons, rather than quarks and gluons. Heavy mesons and nucleon resonances are "integrated out".

QCD is the theory of strong interactions. It is part of the Standard Model of particle physics and it deals with quarks, gluons, and their interactions. One crucial step for the development of an EFT is the identification of a separation of scales. In the hadron spectrum there is a large gap between the masses of pions and vector mesons, such as the $\rho(770)$. So the soft scale is set by the pion mass, $Q \sim m_\pi$, and the rho mass sets the hard (breaking) scale, $\Lambda_\chi \sim m_\rho$. This suggests an expansion in terms of Q/Λ_χ. To make sure that this EFT is not just another phenomenology, there must be a proper link with QCD, which is established by having the EFT observe all relevant symmetries of the underlying theory.

The EFT procedure can be summarized as:

1. Identify soft and hard scales, and the appropriate degrees of freedom for low-energy nuclear physics

2. Identify the relevant symmetries of low-energy QCD (and if and how they are broken)

3. Write down the most general Lagrangian consistent with 1 and 2.

4. Design a low-momentum expansion that can distinguish between more and less important contributions.

5. Guided by 4, calculate the Feynman diagrams for the problem to the desired accuracy.

4.1.1 Symmetries of low-energy QCD

The QCD Lagrangian is

$$\mathcal{L}_{\rm QCD} = \bar{q}(i\gamma^\mu \mathcal{D}_\mu - \mathcal{M})q - \frac{1}{4}\mathcal{G}_{\mu\nu,a}\mathcal{G}_a^{\mu\nu}, \tag{4.1}$$

with the gauge-covariant derivative,

$$\mathcal{D}_\mu = \partial_\mu - ig\frac{\lambda_a}{2}\mathcal{A}_{\mu,a}, \tag{4.2}$$

and the gluon field strength tensor,

$$\mathcal{G}_{\mu\nu,a} = \partial_\mu \mathcal{A}_{\nu,a} - \partial_\nu \mathcal{A}_{\mu,a} + g f_{abc}\mathcal{A}_{\mu,b}\mathcal{A}_{\nu,c}, \tag{4.3}$$

where q stands for the quark fields, $\mathcal{M}$ is the quark mass matrix, g is the strong coupling constant, $\mathcal{A}_{\mu,a}$ are the gluon fields, the λ_a are the Gell-Mann matrices and the f_{abc} are the structure constants of the $\mathrm{SU(3)_{color}}$ Lie algebra $(a, b, c = 1, ..., 8)$.

The masses of the up (u), down (d), and strange (s) quarks are

$$\begin{aligned} m_u &= 2.5 \pm 0.8\mathrm{MeV}, \\ m_d &= 5.0 \pm 0.9\mathrm{MeV}, \\ m_s &= 101 \pm 25\mathrm{MeV}, \end{aligned} \tag{4.4}$$

which are small if compared to a typical hadronic scale (low-mass hadrons which are not Goldstone bosons), $m_\rho \approx 1$ GeV. So let us look at the QCD Lagrangian in the limit of vanishing quark masses,

$$\mathcal{L}^0_{\rm QCD} = \bar{q} i\gamma^\mu \mathcal{D}_\mu q - \frac{1}{4}\mathcal{G}_{\mu\nu,a}\mathcal{G}^{\mu\nu}_a. \tag{4.5}$$

We define the right- and left-handed quark fields, corresponding to spin and momentum aligned and antialigned,

$$q_R = P_R q, \qquad q_L = P_L q, \tag{4.6}$$

with the projectors,

$$P_R = \frac{1}{2}(1+\gamma_5), \qquad P_L = \frac{1}{2}(1-\gamma_5). \tag{4.7}$$

We can rewrite the Lagrangian as

$$\mathcal{L}^0_{\rm QCD} = \bar{q}_R i\gamma^\mu \mathcal{D}_\mu q_R + \bar{q}_L i\gamma^\mu \mathcal{D}_\mu q_L - \frac{1}{4}\mathcal{G}_{\mu\nu,a}\mathcal{G}^{\mu\nu}_a. \tag{4.8}$$

If we restrict ourselves to up and down quarks only, we see that $\mathcal{L}^0_{\rm QCD}$ is invariant under the global unitary transformations

$$q_R = \begin{pmatrix} u_R \\ d_R \end{pmatrix} \mapsto g_R q_R = \exp\left(-i\Theta^R_i \frac{\tau_i}{2}\right) \begin{pmatrix} u_R \\ d_R \end{pmatrix}, \tag{4.9}$$

and

$$q_L = \begin{pmatrix} u_L \\ d_L \end{pmatrix} \mapsto g_L q_L = \exp\left(-i\Theta^L_i \frac{\tau_i}{2}\right) \begin{pmatrix} u_L \\ d_L \end{pmatrix}, \tag{4.10}$$

where the τ_i $(i = 1, 2, 3)$ are the usual Pauli matrices with the commutation relations

$$\left[\frac{\tau_i}{2}, \frac{\tau_j}{2}\right] = i\epsilon^{ijk}\frac{\tau_k}{2}, \tag{4.11}$$

and g_R and g_L are elements of $SU(2)_R$ and $SU(2)_L$, respectively. The conclusion is that right- and left-handed components of massless quarks do not mix. This is the $SU(2)_R \times SU(2)_L$ symmetry, also known as chiral symmetry.

Noether's theorem implies the existence of conserved currents, three right-handed,

$$R_i^\mu = \bar{q}_R \gamma^\mu \frac{\tau_i}{2} q_R \ \text{ with } \partial_\mu R_i^\mu = 0, \tag{4.12}$$

and three left-handed,

$$L_i^\mu = \bar{q}_L \gamma^\mu \frac{\tau_i}{2} q_L \ \text{ with } \partial_\mu L_i^\mu = 0. \tag{4.13}$$

It is useful to consider some linear combinations; three vector-currents

$$V_i^\mu = R_i^\mu + L_i^\mu = \bar{q} \gamma^\mu \frac{\tau_i}{2} q \ \text{ with } \partial_\mu V_i^\mu = 0, \tag{4.14}$$

and three axial-vector currents,

$$A_i^\mu = R_i^\mu - L_i^\mu = \bar{q} \gamma^\mu \gamma_5 \frac{\tau_i}{2} q \ \text{ with } \partial_\mu A_i^\mu = 0, \tag{4.15}$$

which are named after the fact that they transform under parity as vector and axial-vector current densities, respectively. The vector transformations are

$$q = \begin{pmatrix} u \\ d \end{pmatrix} \mapsto \exp\left(-i\Theta_i^V \frac{\tau_i}{2}\right) \begin{pmatrix} u \\ d \end{pmatrix}, \tag{4.16}$$

which represent isospin rotations. Therefore, invariance under vector transformations can be associated with isospin symmetry.

There are six conserved charges,

$$Q_i^R = \int d^3x R_i^0 = \int d^3x q_R^\dagger(t, \boldsymbol{x}) \frac{\tau_i}{2} q_R(t, \boldsymbol{x}), \ \text{with } \frac{dQ_i^R}{dt} = 0, \tag{4.17}$$

and

$$Q_i^L = \int d^3x L_i^0 = \int d^3x q_L^\dagger(t, \boldsymbol{x}) \frac{\tau_i}{2} q_L(t, \boldsymbol{x}), \ \text{with } \frac{dQ_i^L}{dt} = 0. \tag{4.18}$$

Alternatively,

$$Q_i^V = \int d^3x V_i^0 = \int d^3x q^\dagger(t,\boldsymbol{x})\frac{\tau_i}{2}q(t,\boldsymbol{x}), \text{ with } \frac{dQ_i^V}{dt} = 0, \tag{4.19}$$

and

$$Q_i^A = \int d^3x A_i^0 = \int d^3x q^\dagger(t,\boldsymbol{x})\gamma_5\frac{\tau_i}{2}q(t,\boldsymbol{x}), \text{ with } \frac{dQ_i^A}{dt} = 0. \tag{4.20}$$

4.1.2 Explicit symmetry breaking

The mass term in the QCD Lagrangian, Eq. (4.1), breaks chiral symmetry explicitly. Let us write $\mathcal{M}$ for the two-flavor case,

$$\begin{aligned}\mathcal{M} &= \begin{pmatrix} m_u & 0 \\ 0 & m_d \end{pmatrix} = \frac{1}{2}(m_u+m_d)\begin{pmatrix} 1 & 0 \\ 0 & 1 \end{pmatrix} + \frac{1}{2}(m_u-m_d)\begin{pmatrix} 1 & 0 \\ 0 & -1 \end{pmatrix} \\ &= \frac{1}{2}(m_u+m_d)\mathbf{1} + \frac{1}{2}(m_u-m_d)\tau_3. \end{aligned} \tag{4.21}$$

The first term in the last equation is invariant under $SU(2)_V$, i.e. isospin symmetry, and the second term vanishes for $m_u = m_d$. Thus, isospin is an exact symmetry if the up and down quarks have the same masses. However, both terms break chiral symmetry. Since m_u and m_d are much smaller than the typical hadronic mass scale of ~ 1 GeV, the explicit chiral symmetry breaking due to non-vanishing quark masses is very small.

4.1.3 Spontaneous symmetry breaking

A continuous symmetry is said to be spontaneously broken if a symmetry of the Lagrangian is not realized in the ground-state of the system. There is evidence that the approximate chiral symmetry of the QCD Lagrangian is spontaneously broken, which comes from the hadron spectrum. The Q_i^A of Eq. (4.20), a conserved quantity, commutes with the Hamiltonian and it has negative parity, thus one would naively

assume that for any hadron of positive parity there must be a negative one as well. However, these "parity doublets" are not observed in nature.

A spontaneously broken global symmetry implies the existence of massless Goldstone bosons, with the quantum numbers of the broken generators. The broken generators are the Q_i^A of Eq. (4.20), which are pseudoscalar. The Goldstone bosons are identified with the isospin triplet of the pseudoscalar pions. The pion masses are not exactly zero because the masses of u and d quarks do not vanish either (explicit symmetry breaking), but this explains why pions are so light. In pions we see a remarkable example of both spontaneous and explicit symmetry breaking.

4.1.4 Chiral effective Lagrangian

Now we build the Lagrangian consistent with the broken symmetries discussed in the previous sections. The relevant degrees of freedom are nucleons and pions (Goldstone bosons). Since interactions of Goldstone bosons must vanish at zero momentum transfer and in the chiral limit $m_\pi \to 0$, the low-energy expansion of the Lagrangian is arranged in powers of derivatives and pion masses. The effective Lagrangian can formally be written as

$$\mathcal{L}_{\text{eff}} = \mathcal{L}_{\pi\pi} + \mathcal{L}_{\pi N} + \cdots , \tag{4.22}$$

where $\mathcal{L}_{\pi\pi}$ accounts for the dynamics between pions, $\mathcal{L}_{\pi N}$ deals with the interactions of pions and a nucleon, and the ellipsis denotes terms with pions with two or more nucleons. In turn, each Lagrangian can be organized as

$$\mathcal{L}_{\pi\pi} = \mathcal{L}_{\pi\pi}^{(2)} + \mathcal{L}_{\pi\pi}^{(4)} + \cdots$$
$$\mathcal{L}_{\pi N} = \mathcal{L}_{\pi N}^{(1)} + \mathcal{L}_{\pi N}^{(2)} + \cdots ,$$

where the superscript denotes the chiral dimension (number of derivatives or pion mass).

We introduce the SU(2) matrix

$$U = \mathbf{1} + \frac{i}{f_\pi}\boldsymbol{\tau}\cdot\boldsymbol{\pi} - \frac{1}{2f_\pi^2}\boldsymbol{\pi}^2 + \cdots, \tag{4.23}$$

where f_π is the pion decay constant. The coefficient of the linear term was chosen to produce the desired kinetic term in the pion-pion Lagrangian, and the coefficient of the quadratic term enforces that U is unitary, at second order in the pion fields. The leading order (LO) Lagrangian is given by

$$\mathcal{L}^{(2)}_{\pi\pi} = \frac{f_\pi^2}{4}\mathrm{tr}\left[\partial_\mu U \partial^\mu U^\dagger + m_\pi^2(U + U^\dagger)\right]. \tag{4.24}$$

Since Goldstone bosons can interact only when they carry momentum, the interaction between pions comes in powers of $\partial_\mu U$. Only even powers of m_π are present because of Lorentz invariance. The U field transforms under global chiral rotations as

$$U \mapsto g_L U g_R^\dagger. \tag{4.25}$$

Since under global chiral rotations g_R and g_L do not depend on space-time, $\partial_\mu U$ transforms in the same way as U does, hence the first term in Eq. (4.24) is chiral invariant. The second term breaks chiral symmetry explicitly, with the coefficient chosen to reproduce the correct mass term. Inserting U and keeping terms with only two pion fields yields

$$\mathcal{L}^{(2)}_{\pi\pi} = \frac{1}{2}\partial_\mu\boldsymbol{\pi}\cdot\partial^\mu\boldsymbol{\pi} - \frac{1}{2}m_\pi^2\boldsymbol{\pi}^2 + \mathcal{O}(\boldsymbol{\pi}^4), \tag{4.26}$$

where we dropped the constant $f_\pi^2 m_\pi^2$.

The LO relativistic πN Lagrangian is

$$\mathcal{L}^{(1)}_{\pi N} = \bar{\Psi}\left(i\gamma^\mu D_\mu - M_N + \frac{g_A}{2}\gamma^\mu\gamma_5 u_\mu\right)\Psi, \tag{4.27}$$

where the chirally covariant derivative is $D_\mu = \partial_\mu + \Gamma_\mu$, $\Gamma_\mu = [\xi^\dagger, \partial_\mu\xi]$, and $u_\mu = i\left\{\xi^\dagger, \partial_\mu\xi\right\}$ with

$$\xi = \sqrt{U} = \mathbf{1} + \frac{i}{2f_\pi}\boldsymbol{\tau}\cdot\boldsymbol{\pi} - \frac{1}{8f_\pi^2}\boldsymbol{\pi}^2 + \cdots \tag{4.28}$$

Using the identity $(\mathbf{a}\cdot\boldsymbol{\tau})(\mathbf{b}\cdot\boldsymbol{\tau}) = (\mathbf{a}\cdot\mathbf{b})\mathbf{1} + i\boldsymbol{\tau}\cdot(\mathbf{a}\times\mathbf{b})$, we have

$$\Gamma_\mu = \frac{i}{4f_\pi^2}\boldsymbol{\tau}\cdot(\boldsymbol{\pi}\times\partial_\mu\boldsymbol{\pi}) + \mathcal{O}(\boldsymbol{\pi}^4), \tag{4.29}$$

and

$$u_\mu = -\frac{1}{f_\pi}\boldsymbol{\tau}\cdot\partial_\mu\boldsymbol{\pi} + \mathcal{O}(\boldsymbol{\pi}^3). \tag{4.30}$$

The πN Lagrangian of Eq. 4.27 can be cast more explicitly as

$$\mathcal{L}_{\pi N}^{(1)} = \bar{\Psi}\left(i\gamma^\mu\partial_\mu - M_N - \frac{1}{4f_\pi^2}\gamma^\mu\boldsymbol{\tau}\cdot(\boldsymbol{\pi}\times\partial_\mu\boldsymbol{\pi}) - \frac{g_A}{2f_\pi}\gamma^\mu\gamma_5\boldsymbol{\tau}\cdot\partial_\mu\boldsymbol{\pi} + \cdots\right)\Psi. \tag{4.31}$$

The term proportional to $g_A/2f_\pi$ is the axial-vector coupling of one pion to a nucleon, and the term proportional to $1/4f_\pi^2$ is the so-called Weinberg-Tomozawa coupling. Finally, the LO NN Lagrangian is

$$\mathcal{L}_{NN}^{(0)} = -\frac{1}{2}C_S(\bar{N}N)(\bar{N}N) - \frac{1}{2}C_T(\bar{N}\sigma^i N)(\bar{N}\sigma^i N). \tag{4.32}$$

4.1.5 Heavy baryon formalism

The relativistic treatment of baryons in chiral perturbation theory leads to problems, mainly because the time-derivative of a relativistic baryon field gives a factor of $E \approx M$ (M being the baryon mass), which is not small as compared to the chiral breaking scale $\Lambda_\chi \approx 1$ GeV. A solution is to treat baryons as heavy static sources, the so-called extreme nonrelativistic limit, because the momentum transfers between baryons and pions is small if compared to the baryon mass. Here we follow the treatment of Gårdestig *et al.* (2007). The Lagrangian of Eq. (4.27) can easily be cast in the form

$$\mathcal{L} = \bar{\Psi}(i\gamma^\mu D_\mu - M_N + \gamma_0 G)\Psi, \tag{4.33}$$

with

$$G = \begin{pmatrix} A & B \\ C & D \end{pmatrix}, \tag{4.34}$$

with $A - D$ being 2x2 matices. In our case $B = -C$ and $A = -D$, but we carry out the general procedure. A heavy fermion implies that it is essentially static, and we can expand its four-momenta around its large mass. We write p^μ in terms of the four-velocity v^μ and a residual fermion momentum l^μ,

$$p^\mu = mv^\mu + l^\mu, \tag{4.35}$$

where $l^\mu \ll m$ and $v^2 = 1$. For an on-shell fermion ($p^2 = m^2$), we have $2mv\cdot l + l^2 = 0$.

We split the fermion field into large and small components, H and h respectively,

$$\Psi = e^{-imv\cdot c}(H + h), \tag{4.36}$$

where $\not{v}H = H$ and $\not{v}h = -h$. We assume, without loss of generality, that $v^\mu = (1, 0, 0, 0)$, such that $\not{v} = \gamma_0$. Equation (4.33) now reads

$$\mathcal{L} = (H^\dagger \; h^\dagger) \begin{pmatrix} iD_0 + A & -i\boldsymbol{\sigma}\cdot\vec{D} + B \\ -i\boldsymbol{\sigma}\cdot\vec{D} + C & 2m + iD_0 + D \end{pmatrix} \begin{pmatrix} H \\ h \end{pmatrix}. \tag{4.37}$$

The mixing between upper and lower components is avoided by defining a new small component field h',

$$\begin{aligned} h &= h' - (2m + iD_0 + D)^{-1}(-i\boldsymbol{\sigma}\cdot\vec{D} + C)H, \\ h^\dagger &= h'^\dagger - H^\dagger(-i\boldsymbol{\sigma}\cdot\vec{D} + B)(2m + iD_0 + D)^{-1}. \end{aligned} \tag{4.38}$$

Now, the Lagrangian is block-diagonal,

$$\begin{aligned} \mathcal{L} = H^\dagger \left(iD_0 + A - (-i\boldsymbol{\sigma}\cdot\vec{D} + B)\frac{1}{2m + iD_0 + D}(-i\boldsymbol{\sigma}\cdot\vec{D} + C) \right) H \\ + h'^\dagger(2m + iD_0 + D)h'. \end{aligned} \tag{4.39}$$

After integrating out the small components, only the H fields remain (Gårdestig *et al.* (2007)). Then we expand this term assuming $iD^\mu, G \ll 2m$, that is, in powers

of $(iD_0 + D)/2m$. The first two orders (inverse power of M_N) of the heavy fermions Lagrangian are

$$\mathcal{L}^{(0)}_{\rm HF} = H^\dagger(iD_0 + A)H \tag{4.40}$$

$$\mathcal{L}^{(1)}_{\rm HF} = -\frac{1}{2M_N}H^\dagger(-i\boldsymbol{\sigma}\cdot\vec{D} + B)(-i\boldsymbol{\sigma}\cdot\vec{D} + C)H. \tag{4.41}$$

We use Eq. (4.40) to treat the πN Lagrangian of Eq. (4.31) non-relativistically, and we include the $\pi\pi$ and NN Lagrangians of Eqs. (4.26) and (4.32). Finally, the heavy baryon leading order chiral Lagrangian in which only nucleons and pions degrees of freedom are included reads (Machleidt and Entem (2011))

$$\begin{aligned}\mathcal{L}_0 = &\frac{1}{2}\partial_\mu\pi_i\partial^\mu\pi_i - \frac{1}{2}m_\pi^2\pi_i\pi_i + N^\dagger\Big[i\partial_0 + \frac{\nabla^2}{2M_0} - \frac{1}{4f_\pi^2}\epsilon_{ijk}\tau_i\pi_j\partial_0\pi_k - M_0\Big]N \\ &- \frac{g_A}{2f_\pi}N^\dagger\tau_i\sigma^j\partial_j\pi_i N - \frac{1}{2}C_S(N^\dagger N)(N^\dagger N) - \frac{1}{2}C_T(N^\dagger\sigma^i N)(N^\dagger\sigma^i N)\,.\end{aligned} \tag{4.42}$$

Note that, although the nucleon kinetic energy appears at next to leading order (it comes from Eq. (4.41)), it has been promoted to the leading order, to allow the usage of quantum Monte Carlo algorithms. For convenience, let us split the Lagrangian into

$$\begin{aligned}\mathcal{L}_{\pi\pi} &= \frac{1}{2}\partial_\mu\pi_i\partial^\mu\pi_i - \frac{1}{2}m_\pi^2\pi_i\pi_i \\ \mathcal{L}_{\pi NN} &= N^\dagger\left[-\frac{g_A}{2f_\pi}\tau_i\sigma^j\partial_j\pi_i - \frac{1}{4f_\pi^2}\epsilon_{ijk}\tau_i\pi_j\partial_0\pi_k\right]N \\ \mathcal{L}_{NN} &= N^\dagger\left[i\partial_0 + \frac{\nabla^2}{2M_0} - M_0\right]N - \frac{1}{2}C_S(N^\dagger N)(N^\dagger N) \\ &\quad -\frac{1}{2}C_T(N^\dagger\sigma^i N)(N^\dagger\sigma^i N).\end{aligned} \tag{4.43}$$

The conjugate fields are given by

$$\begin{aligned}\Pi_N &= \frac{\partial\mathcal{L}}{\partial(\partial_0 N)} = iN^\dagger \\ \Pi_{N^\dagger} &= \frac{\partial\mathcal{L}}{\partial(\partial_0 N^\dagger)} = 0 \\ \Pi_k &= \frac{\partial\mathcal{L}}{\partial(\partial_0\pi_k)} = \partial_0\pi_k - \frac{1}{4f_\pi^2}\epsilon_{ijk}\pi_j N^\dagger\tau_i N\,.\end{aligned} \tag{4.44}$$

The Hamiltonian density is obtained as

$$\begin{aligned}\mathcal{H} &= \Pi_N \partial_0 N + \Pi_k \partial_0 \pi_k - \mathcal{L} \\ &= \frac{1}{2}\partial_0\pi_k\partial_0\pi_k + \frac{1}{2}\partial_i\pi_k\partial_i\pi_k + \frac{1}{2}m_\pi^2\pi_k\pi_k + \frac{g_A}{2f_\pi}N^\dagger\tau_i\sigma^j\partial_j\pi_i N - N^\dagger\left[\frac{\nabla^2}{2M_0} - M_0\right]N \\ &+ \frac{1}{2}C_S(N^\dagger N)(N^\dagger N) + \frac{1}{2}C_T(N^\dagger\sigma^i N)(N^\dagger\sigma^i N). \end{aligned} \tag{4.45}$$

Note that the natural variables of the Hamiltonian density are the fields and their conjugate momenta. Therefore, we need to express $\partial_0\pi_k$ in terms of Π_k,

$$\partial_0\pi_k = \Pi_k + \frac{1}{4f_\pi^2}\epsilon_{ijk}\pi_j N^\dagger\tau_i N, \tag{4.46}$$

and,

$$\begin{aligned}(\partial_0\pi_k)^2 &= \Pi_k^2 + \frac{1}{2f_\pi^2}\epsilon_{ijk}\pi_j\Pi_k N^\dagger\tau_i N + \frac{1}{16f_\pi^4}\epsilon_{ijk}\pi_j N^\dagger\tau_i N\epsilon_{lmk}\pi_m N^\dagger\tau_l N \\ &= \Pi_k^2 + \frac{1}{2f_\pi^2}\epsilon_{ijk}\pi_j\Pi_k N^\dagger\tau_i N + \frac{1}{16f_\pi^4}\pi_j N^\dagger\tau_i N\left[\pi_j N^\dagger\tau_i N - \pi_i N^\dagger\tau_j N\right], \end{aligned} \tag{4.47}$$

where we used the property $\epsilon_{ijk}\epsilon_{ilm} = \delta_{jl}\delta_{km} - \delta_{jm}\delta_{kl}$.

The Hamiltonian density can be written as a sum of three terms,

$$\begin{aligned}\mathcal{H}_{\pi\pi} &= \frac{1}{2}\Pi_k\Pi_k + \frac{1}{2}\partial_i\pi_k\partial_i\pi_k + \frac{1}{2}m_\pi^2\pi_k\pi_k, \\ \mathcal{H}_{\pi N} &= \frac{1}{4f_\pi^2}\epsilon_{ijk}\pi_j\Pi_k N^\dagger\tau_i N + \frac{1}{32f_\pi^4}\pi_j N^\dagger\tau_i N\Big[\pi_j N^\dagger\tau_i N - \pi_i N^\dagger\tau_j N\Big] \\ &\quad + \frac{g_A}{2f_\pi}N^\dagger\tau_i\sigma^j\partial_j\pi_i N, \\ \mathcal{H}_{NN} &= N^\dagger\left[-\frac{\nabla^2}{2M_0} + M_0\right]N + \frac{1}{2}C_S(N^\dagger N)(N^\dagger N) + \frac{1}{2}C_T(N^\dagger\sigma^i N)(N^\dagger\sigma^i N). \end{aligned} \tag{4.48}$$

The term proportional to $1/f_\pi^4$ is higher order, thus we drop it. Note that the Hamiltonian is a constant of motion and we can conveniently write the three contributions above at $x^0 = t = 0$. The pion-field term is given by

$$H_{\pi\pi} = \int d^3x \frac{1}{2}\Big[\Pi_i^2(\mathbf{x}) + (\nabla\pi_i(\mathbf{x}))^2 + m_\pi^2\pi_i^2(\mathbf{x})\Big], \tag{4.49}$$

where the standard conventions adopted for the gradient are given in Appendix C. The pion-nucleon interaction Hamiltonian reads

$$H_{\pi N} = \int d^3x \left[\frac{g_A}{2f_\pi} N^\dagger(\mathbf{x}) \tau_i \sigma^j \partial_j \pi_i(\mathbf{x}) N(\mathbf{x}) + \frac{1}{4f_\pi^2} \epsilon_{ijk} \pi_j(\mathbf{x}) \Pi_k(\mathbf{x}) N^\dagger(\mathbf{x}) \tau_i N(\mathbf{x}) \right]. \tag{4.50}$$

The first term is the axial-vector pion-nucleon coupling, and the second (referred to as the Weinberg-Tomozawa term) is the contact interaction with two factors of the pion field interacting with the nucleon at a single point (Scherer (2010)). The nucleon Hamiltonian is given by

$$\begin{aligned} H_{NN} = \int d^3x \Big[N^\dagger(\mathbf{x}) \Big(-\frac{\nabla^2}{2M_0} + M_0 \Big) N(\mathbf{x}) + \frac{1}{2} C_S N^\dagger(\mathbf{x}) N(\mathbf{x}) N^\dagger(\mathbf{x}) N(\mathbf{x}) + \\ \frac{1}{2} C_T N^\dagger(\mathbf{x}) \sigma^i N(\mathbf{x}) N^\dagger(\mathbf{x}) \sigma^i N(\mathbf{x}) \Big], \end{aligned} \tag{4.51}$$

where C_S and C_T are two low-energy constants (LEC) that have to be fitted against two-nucleon properties.

Up to this point everything in this chapter is well known in chiral EFT. In the following sections we present our contributions, that is, a formulation of chiral EFT in a way appropriate for quantum Monte Carlo methods.

4.2 Pion fields in the Schrödinger picture

4.2.1 The formalism

We work in the Schrödinger picture, where the pion fields and their conjugate momenta are time independent, and obey the canonical commutation relations,

$$\begin{aligned} [\pi_i(\boldsymbol{x}), \pi_j(\boldsymbol{y})] = [\Pi_i(\boldsymbol{x}), \Pi_j(\boldsymbol{y})] = 0, \\ [\pi_i(\boldsymbol{x}), \Pi_j(\boldsymbol{y})] = i\delta_{ij}\delta^{(3)}(\boldsymbol{x} - \boldsymbol{y}). \end{aligned} \tag{4.52}$$

Let us perform a plane-wave expansion in a box of size L with periodic boundary conditions, implying that the allowed momenta are discretized,

$$\boldsymbol{k} = \frac{2\pi}{L}(n_x, n_y, n_z), \text{ with } n_i = 0, \pm 1, \pm 2, \ldots \tag{4.53}$$

This discretization introduces an infrared cutoff on the three-momentum of the pions, proportional to the inverse of the size of the box. To avoid infinities, the theory is regularized introducing an ultraviolet cutoff for the three-momentum of the pions, such that $k \equiv |\boldsymbol{k}| \leq k_c$. The Fourier expansions read

$$\begin{aligned} \pi_i(\boldsymbol{x}) &= \frac{1}{\sqrt{L^3}} \sum_{\boldsymbol{k}} \pi_{i\boldsymbol{k}} e^{i\boldsymbol{k}\cdot\boldsymbol{x}}, \\ \Pi_i(\boldsymbol{x}) &= \frac{1}{\sqrt{L^3}} \sum_{\boldsymbol{k}} \Pi_{i\boldsymbol{k}} e^{i\boldsymbol{k}\cdot\boldsymbol{x}}\,. \end{aligned} \tag{4.54}$$

Since the fields are hermitian, the mode operators are such that $\pi^\dagger_{i\boldsymbol{k}} = \pi_{i-\boldsymbol{k}}$ and $\Pi^\dagger_{i\boldsymbol{k}} = \Pi_{i-\boldsymbol{k}}$. The canonical commutation relations of Eq. (4.52) imply

$$\begin{aligned} [\pi_{i\boldsymbol{k}}, \pi_{j\boldsymbol{k}'}] &= [\Pi_{i\boldsymbol{k}}, \Pi_{j\boldsymbol{k}'}] = 0, \\ [\pi_{i\boldsymbol{k}}, \Pi_{j\boldsymbol{k}'}] &= i\delta_{ij}\delta_{\boldsymbol{k}-\boldsymbol{k}'}. \end{aligned} \tag{4.55}$$

When expressed in terms of the pion modes, the free pion Hamiltonian of Eq. (4.49) describes a collection of harmonic oscillators with frequencies $\omega_{\boldsymbol{k}} = \sqrt{k^2 + m_\pi^2}$,

$$H_{\pi\pi} = \sum_{\boldsymbol{k}} \sum_i \left[\frac{1}{2}\Pi^2_{i\boldsymbol{k}} + \frac{1}{2}\omega^2_{\boldsymbol{k}} \pi^2_{i\boldsymbol{k}} \right]. \tag{4.56}$$

The latter can be quantized by defining the creation and annihilation operators,

$$\begin{aligned} a_{i\boldsymbol{k}} &= \frac{1}{\sqrt{2\omega_{\boldsymbol{k}}}}(\omega_{\boldsymbol{k}}\pi_{i\boldsymbol{k}} + i\Pi_{i\boldsymbol{k}}) \\ a^\dagger_{i\boldsymbol{k}} &= \frac{1}{\sqrt{2\omega_{\boldsymbol{k}}}}(\omega_{\boldsymbol{k}}\pi^\dagger_{i\boldsymbol{k}} - i\Pi^\dagger_{i\boldsymbol{k}})\,, \end{aligned} \tag{4.57}$$

which are independent for each mode, and satisfy the canonical commutation relations,

$$[a_{i\boldsymbol{k}}, a^\dagger_{j\boldsymbol{q}}] = \delta_{ij}\delta_{\boldsymbol{k}\boldsymbol{q}}\,. \tag{4.58}$$

Using Eq. (4.57) to express $\pi_{i\boldsymbol{k}}$ and $\Pi_{i\boldsymbol{k}}$ in Eq. (4.54) in terms of the creation and annihilation operators, we recover the usual expansion for the pion field operator and its conjugate momentum,

$$\begin{aligned}
\pi_i(\boldsymbol{r}) &= \frac{1}{\sqrt{2L^3}} \sum_{\boldsymbol{k}} \frac{1}{\sqrt{\omega_{\boldsymbol{k}}}} \left[a_{i\boldsymbol{k}} e^{i\boldsymbol{k}\cdot\boldsymbol{r}} + a^\dagger_{i\boldsymbol{k}} e^{-i\boldsymbol{k}\cdot\boldsymbol{r}} \right], \\
\Pi_i(\boldsymbol{r}) &= \frac{-i}{\sqrt{2L^3}} \sum_{\boldsymbol{k}} \sqrt{\omega_{\boldsymbol{k}}} \left[a_{i\boldsymbol{k}} e^{i\boldsymbol{k}\cdot\boldsymbol{r}} - a^\dagger_{i\boldsymbol{k}} e^{-i\boldsymbol{k}\cdot\boldsymbol{r}} \right], \qquad (4.59)
\end{aligned}$$

where $\omega_{\boldsymbol{k}} = \sqrt{k^2 + m_\pi^2}$. We perform the unitary transformation,

$$\begin{aligned}
a^\dagger_{i\boldsymbol{k}} &= \frac{1}{\sqrt{2}} \left(c^\dagger_{i\boldsymbol{k}} + i s^\dagger_{i\boldsymbol{k}} \right), \\
a^\dagger_{i-\boldsymbol{k}} &= \frac{1}{\sqrt{2}} \left(c^\dagger_{i\boldsymbol{k}} - i s^\dagger_{i\boldsymbol{k}} \right), \qquad (4.60)
\end{aligned}$$

where the $\boldsymbol{k}$ values on the right hand side of the equations are chosen typically so that $\boldsymbol{k}$ is included and $-\boldsymbol{k}$ is not. Specifically, if $k_z \neq 0$ then $k_z > 0$; if $k_z = 0$ and $k_y \neq 0$ then $k_y > 0$; and if $k_z = k_y = 0$ then $k_x > 0$. The single $\boldsymbol{k} = 0$ mode does not couple to the nucleons through the axial-vector coupling, but it does couple to them via the Weinberg-Tomozawa term. With these definitions, the operators satisfy the canonical commutation relations $[a, a^\dagger] = 1$, and all operators with different arguments commute. The field operator and its conjugate momentum can be written as

$$\begin{aligned}
\pi_i(\boldsymbol{r}) &= \frac{1}{\sqrt{2m_\pi L^3}} (c^\dagger_{i0} + c_{i0}) \\
&\quad + \sqrt{\frac{2}{L^3}} {\sum_{\boldsymbol{k}}}' \frac{1}{\sqrt{2\omega_{\boldsymbol{k}}}} \left[(c^\dagger_{i\boldsymbol{k}} + c_{i\boldsymbol{k}}) \cos(\boldsymbol{k}\cdot\boldsymbol{r}) + (s^\dagger_{i\boldsymbol{k}} + s_{i\boldsymbol{k}}) \sin(\boldsymbol{k}\cdot\boldsymbol{r}) \right], \\
\Pi_i(\boldsymbol{r}) &= i \sqrt{\frac{m_\pi}{2L^3}} (c^\dagger_{i0} - c_{i0}) \\
&\quad + \sqrt{\frac{2}{L^3}} {\sum_{\boldsymbol{k}}}' i \sqrt{\frac{\omega_{\boldsymbol{k}}}{2}} \left[(c^\dagger_{i\boldsymbol{k}} - c_{i\boldsymbol{k}}) \cos(\boldsymbol{k}\cdot\boldsymbol{r}) + (s^\dagger_{i\boldsymbol{k}} - s_{i\boldsymbol{k}}) \sin(\boldsymbol{k}\cdot\boldsymbol{r}) \right], \qquad (4.61)
\end{aligned}$$

where hereafter we adopt the convention of a primed sum to indicate that it is over the set of $\boldsymbol{k}$ described above. We employ the usual harmonic oscillator definitions,

$x = (a + a^\dagger)/\sqrt{2\omega}$ and $p = i\sqrt{\omega/2}(a^\dagger - a)$, to write the c and s operators in terms of the field amplitude operators in whose eigenspace we work,

$$\begin{aligned} \pi^c_{i\boldsymbol{k}} &= \frac{1}{\sqrt{2\omega_{\boldsymbol{k}}}}(c^\dagger_{i\boldsymbol{k}} + c_{i\boldsymbol{k}}), \qquad & \pi^s_{i\boldsymbol{k}} &= \frac{1}{\sqrt{2\omega_{\boldsymbol{k}}}}(s^\dagger_{i\boldsymbol{k}} + s_{i\boldsymbol{k}}), \\ \Pi^c_{i\boldsymbol{k}} &= i\sqrt{\frac{\omega_{\boldsymbol{k}}}{2}}(c^+_{i\boldsymbol{k}} - c_{i\boldsymbol{k}}), \qquad & \Pi^s_{i\boldsymbol{k}} &= i\sqrt{\frac{\omega_{\boldsymbol{k}}}{2}}(s^+_{i\boldsymbol{k}} - s_{i\boldsymbol{k}}), \end{aligned} \tag{4.62}$$

so that

$$\begin{aligned} \pi_i(\boldsymbol{r}) &= \frac{\pi^c_{i0}}{\sqrt{L^3}} + \sqrt{\frac{2}{L^3}}{\sum_{\boldsymbol{k}}}' \left[\pi^c_{i\boldsymbol{k}} \cos(\boldsymbol{k}\cdot\boldsymbol{r}) + \pi^s_{i\boldsymbol{k}} \sin(\boldsymbol{k}\cdot\boldsymbol{r})\right], \\ \Pi_i(\boldsymbol{r}) &= \frac{\Pi^c_{i0}}{\sqrt{L^3}} + \sqrt{\frac{2}{L^3}}{\sum_{\boldsymbol{k}}}' \left[\Pi^c_{i\boldsymbol{k}} \cos(\boldsymbol{k}\cdot\boldsymbol{r}) + \Pi^s_{i\boldsymbol{k}} \sin(\boldsymbol{k}\cdot\boldsymbol{r})\right]. \end{aligned} \tag{4.63}$$

Now it should be clear that the fields π and Π obey the canonical commutation relations. We use $[\pi^\alpha_{j\boldsymbol{k}}, \Pi^\beta_{j\boldsymbol{k}'}] = i\delta_{\alpha,\beta}\delta_{\boldsymbol{k},\boldsymbol{k}'}\delta_{j,j'}$, to calculate

$$\begin{aligned} [\pi_i(\boldsymbol{r}), \Pi_i(\boldsymbol{r}')] &= \frac{2i}{L^3}{\sum_{\boldsymbol{k}}}' \cos(\boldsymbol{k}\cdot\boldsymbol{r})\cos(\boldsymbol{k}\cdot\boldsymbol{r}') + \sin(\boldsymbol{k}\cdot\boldsymbol{r})\sin(\boldsymbol{k}\cdot\boldsymbol{r}') \\ &= \frac{i}{L^3}{\sum_{\boldsymbol{k}}}' \left(\cos(\boldsymbol{k}\cdot(\boldsymbol{r}+\boldsymbol{r}')) + \cos(\boldsymbol{k}\cdot(\boldsymbol{r}-\boldsymbol{r}'))\right. \\ &\quad \left. - \cos(\boldsymbol{k}\cdot(\boldsymbol{r}+\boldsymbol{r}')) + \cos(\boldsymbol{k}\cdot(\boldsymbol{r}-\boldsymbol{r}'))\right) \\ &= \frac{2i}{L^3}{\sum_{\boldsymbol{k}}}' \cos(\boldsymbol{k}\cdot(\boldsymbol{r}-\boldsymbol{r}')) \\ &= \frac{i}{L^3}\sum_{\boldsymbol{k}} \exp[i\boldsymbol{k}\cdot(\boldsymbol{r}-\boldsymbol{r}')] \xrightarrow[k_c\to\infty]{} i\delta^{(3)}(\boldsymbol{r}-\boldsymbol{r}'), \end{aligned} \tag{4.64}$$

where we have omitted the unwanted indexes.

The pion Hamiltonian of Eq. (4.56) becomes

$$H_{\pi\pi} = {\sum_{\boldsymbol{k}}}' \sum_i \left[\frac{1}{2}\Pi^{c\,2}_{i\boldsymbol{k}} + \frac{1}{2}\Pi^{s\,2}_{i\boldsymbol{k}} + \frac{1}{2}(k^2 + m_\pi^2)(\pi^{c\,2}_{i\boldsymbol{k}} + \pi^{s\,2}_{i\boldsymbol{k}})\right]. \tag{4.65}$$

In our simulations, in exact analogy to working in the position operator eigenstates of the usual harmonic oscillator, we work in the eigenbasis of the mode amplitude operators, $\pi^{c,s}_{i\boldsymbol{k}}$. Wave functions which are the overlaps of our states with this basis,

represent the states. The momentum operators conjugate to $\pi^{c,s}_{i\boldsymbol{k}}$ are the generators of translations of these amplitudes, and therefore when operating on a state represented in this basis, they give the derivative of the wave function in the usual way,

$$\Pi^{c,s}_{i\boldsymbol{k}} \to -i\frac{\partial}{\partial \pi^{c,s}_{i\boldsymbol{k}}}. \tag{4.66}$$

Using the latter relation, the free pion Hamiltonian operating on the state becomes the differential operator

$$H_{\pi\pi} = {\sum_{\boldsymbol{k}}}' \sum_i \left[-\frac{1}{2}\frac{\partial^2}{\partial \pi^{c\,2}_{i\boldsymbol{k}}} - \frac{1}{2}\frac{\partial^2}{\partial \pi^{s\,2}_{i\boldsymbol{k}}} + \frac{1}{2}(k^2 + m_\pi^2)(\pi^{c\,2}_{i\boldsymbol{k}} + \pi^{s\,2}_{i\boldsymbol{k}}) \right], \tag{4.67}$$

operating on the wave function.

The ground-state wave function for the pion modes is analogous to that describing the positions of a collection of quantum harmonic oscillators,

$$\Psi_0(\boldsymbol{\pi}^{c,s}) = \exp\left[-{\sum_{\boldsymbol{k}}}' \sum_i \frac{\omega_k}{2}(\pi^{c\,2}_{i\boldsymbol{k}} + \pi^{s\,2}_{i\boldsymbol{k}}) \right]. \tag{4.68}$$

where we use the symbol $\boldsymbol{\pi}^{c,s}$ to denote the full set of $\pi^c_{i\boldsymbol{k}}$ and $\pi^s_{i\boldsymbol{k}}$. When pion-nucleon interactions are accounted for in the Hamiltonian, the solution of the Schrödinger equation is no longer in closed form. We will employ QMC methods to tackle this problem when one and two nucleons are present in the system under study.

4.2.2 Pion density

We define

$$\psi_i(\boldsymbol{r}) = \frac{1}{\sqrt{L^3}} \sum_{\boldsymbol{k}} a_{i\boldsymbol{k}} e^{i\boldsymbol{k}\cdot\boldsymbol{r}}, \tag{4.69}$$

which has the commutation relations

$$\left[\psi_i(\boldsymbol{r}), \psi_i^\dagger(\boldsymbol{r}') \right] = \frac{1}{L^3} \sum_{\boldsymbol{k}} e^{i\boldsymbol{k}\cdot(\boldsymbol{r}-\boldsymbol{r}')}. \tag{4.70}$$

In the limit of infinite ultraviolet cutoff, this expression tends to $\delta^{(3)}(\boldsymbol{r} - \boldsymbol{r}')$, as prescribed by the canonical commutation relations. For a finite cutoff k_c, the delta

function will be smeared over a volume proportional to k_c^{-3}. The corresponding Cartesian component pion density operator is defined as

$$\rho_i(\boldsymbol{r}) = \psi_i^\dagger(\boldsymbol{r})\psi_i(\boldsymbol{r}). \tag{4.71}$$

To compute the expression above we must change the sums over $\boldsymbol{k}$ to the primed sums using half of the $\boldsymbol{k}$ values,

$$\begin{aligned}
\sum_{\boldsymbol{k}} a_{\boldsymbol{k}}^\dagger e^{-i\boldsymbol{k}\cdot\boldsymbol{r}} &= \sum_{\boldsymbol{k}}{}' (a_{\boldsymbol{k}}^\dagger e^{-i\boldsymbol{k}\cdot\boldsymbol{r}} + a_{-\boldsymbol{k}}^\dagger e^{i\boldsymbol{k}\cdot\boldsymbol{r}}) \\
&= \frac{1}{\sqrt{2}}\sum_{\boldsymbol{k}}{}' \left[(c_{\boldsymbol{k}}^\dagger + is_{\boldsymbol{k}}^\dagger)e^{-i\boldsymbol{k}\cdot\boldsymbol{r}} + (c_{\boldsymbol{k}}^\dagger - is_{\boldsymbol{k}}^\dagger)e^{i\boldsymbol{k}\cdot\boldsymbol{r}}\right], \\
\sum_{\boldsymbol{k}'} a_{\boldsymbol{k}'} e^{i\boldsymbol{k}'\cdot\boldsymbol{r}} &= \sum_{\boldsymbol{k}'}{}' (a_{\boldsymbol{k}'} e^{i\boldsymbol{k}'\cdot\boldsymbol{r}} + a_{-\boldsymbol{k}'} e^{-i\boldsymbol{k}'\cdot\boldsymbol{r}}) \\
&= \frac{1}{\sqrt{2}}\sum_{\boldsymbol{k}'}{}' \left[(c_{\boldsymbol{k}'} - is_{\boldsymbol{k}'})e^{i\boldsymbol{k}'\cdot\boldsymbol{r}} + (c_{\boldsymbol{k}'} + is_{\boldsymbol{k}'})e^{-i\boldsymbol{k}'\cdot\boldsymbol{r}}\right].
\end{aligned} \tag{4.72}$$

Hence,

$$\begin{aligned}
\rho_i(\boldsymbol{r}) &= \frac{1}{2L^3}\sum_{\boldsymbol{k},\boldsymbol{k}'}{}' \left[(c_{\boldsymbol{k}}^\dagger + is_{\boldsymbol{k}}^\dagger)e^{-i\boldsymbol{k}\cdot\boldsymbol{r}} + (c_{\boldsymbol{k}}^\dagger - is_{\boldsymbol{k}}^\dagger)e^{i\boldsymbol{k}\cdot\boldsymbol{r}}\right] \times \\
&\quad \left[(c_{\boldsymbol{k}'} - is_{\boldsymbol{k}'})e^{i\boldsymbol{k}'\cdot\boldsymbol{r}} + (c_{\boldsymbol{k}'} + is_{\boldsymbol{k}'})e^{-i\boldsymbol{k}'\cdot\boldsymbol{r}}\right] \\
&= \frac{1}{2L^3}\sum_{\boldsymbol{k},\boldsymbol{k}'}{}' [4c_{\boldsymbol{k}}^\dagger c_{\boldsymbol{k}'}\cos(\boldsymbol{k}\cdot\boldsymbol{r})\cos(\boldsymbol{k}'\cdot\boldsymbol{r}) + 4s_{\boldsymbol{k}}^\dagger c_{\boldsymbol{k}'}\sin(\boldsymbol{k}\cdot\boldsymbol{r})\cos(\boldsymbol{k}'\cdot\boldsymbol{r}) \\
&\quad +4c_{\boldsymbol{k}}^\dagger s_{\boldsymbol{k}'}\cos(\boldsymbol{k}\cdot\boldsymbol{r})\sin(\boldsymbol{k}'\cdot\boldsymbol{r}) + 4s_{\boldsymbol{k}}^\dagger s_{\boldsymbol{k}'}\sin(\boldsymbol{k}\cdot\boldsymbol{r})\sin(\boldsymbol{k}'\cdot\boldsymbol{r})].
\end{aligned} \tag{4.73}$$

So the cartesian component pion density operator is

$$\begin{aligned}
\rho_i(\boldsymbol{r}) = \frac{2}{L^3}\sum_{\boldsymbol{k},\boldsymbol{k}'}{}' &[c_{\boldsymbol{k}}^\dagger c_{\boldsymbol{k}'}\cos(\boldsymbol{k}\cdot\boldsymbol{r})\cos(\boldsymbol{k}'\cdot\boldsymbol{r}) + s_{\boldsymbol{k}}^\dagger c_{\boldsymbol{k}'}\sin(\boldsymbol{k}\cdot\boldsymbol{r})\cos(\boldsymbol{k}'\cdot\boldsymbol{r}) \\
&+c_{\boldsymbol{k}}^\dagger s_{\boldsymbol{k}'}\cos(\boldsymbol{k}\cdot\boldsymbol{r})\sin(\boldsymbol{k}'\cdot\boldsymbol{r}) + s_{\boldsymbol{k}}^\dagger s_{\boldsymbol{k}'}\sin(\boldsymbol{k}\cdot\boldsymbol{r})\sin(\boldsymbol{k}'\cdot\boldsymbol{r})].
\end{aligned} \tag{4.74}$$

The density can be resolved for the different charge states,

$$\begin{aligned}
\rho_{\pi^+}(\boldsymbol{r}) &= \left[\frac{\psi_x^\dagger(\boldsymbol{r}) - i\psi_y^\dagger(\boldsymbol{r})}{\sqrt{2}}\right]\left[\frac{\psi_x(\boldsymbol{r}) + i\psi_y(\boldsymbol{r})}{\sqrt{2}}\right], \\
\rho_{\pi^-}(\boldsymbol{r}) &= \left[\frac{\psi_x^\dagger(\boldsymbol{r}) + i\psi_y^\dagger(\boldsymbol{r})}{\sqrt{2}}\right]\left[\frac{\psi_x(\boldsymbol{r}) - i\psi_y(\boldsymbol{r})}{\sqrt{2}}\right], \\
\rho_{\pi^0}(\boldsymbol{r}) &= \psi_z^\dagger(\boldsymbol{r})\psi_z(\boldsymbol{r})\,. \qquad (4.75)
\end{aligned}$$

The corresponding operators are

$$\begin{aligned}
\rho_{\pi^+}(\boldsymbol{r}) &= \frac{1}{2}\left[\psi_x^\dagger(\boldsymbol{r})\psi_x(\boldsymbol{r}) + i\psi_x^\dagger(\boldsymbol{r})\psi_y(\boldsymbol{r}) - i\psi_y^\dagger(\boldsymbol{r})\psi_x(\boldsymbol{r}) + \psi_y^\dagger(\boldsymbol{r})\psi_y(\boldsymbol{r})\right], \\
\rho_{\pi^-}(\boldsymbol{r}) &= \frac{1}{2}\left[\psi_x^\dagger(\boldsymbol{r})\psi_x(\boldsymbol{r}) - i\psi_x^\dagger(\boldsymbol{r})\psi_y(\boldsymbol{r}) + i\psi_y^\dagger(\boldsymbol{r})\psi_x(\boldsymbol{r}) + \psi_y^\dagger(\boldsymbol{r})\psi_y(\boldsymbol{r})\right], \qquad (4.76)
\end{aligned}$$

with

$$\begin{aligned}
\psi_x^\dagger(\boldsymbol{r})\psi_y(\boldsymbol{r}) = \frac{2}{L^3}{\sum_{\boldsymbol{k},\boldsymbol{k'}}}'[&c_{x\boldsymbol{k}}^\dagger c_{y\boldsymbol{k'}}\cos(\boldsymbol{k}\cdot\boldsymbol{r})\cos(\boldsymbol{k'}\cdot\boldsymbol{r}) + s_{x\boldsymbol{k}}^\dagger c_{y\boldsymbol{k'}}\sin(\boldsymbol{k}\cdot\boldsymbol{r})\cos(\boldsymbol{k'}\cdot\boldsymbol{r}) \\
&+c_{x\boldsymbol{k}}^\dagger s_{y\boldsymbol{k'}}\cos(\boldsymbol{k}\cdot\boldsymbol{r})\sin(\boldsymbol{k'}\cdot\boldsymbol{r}) + s_{x\boldsymbol{k}}^\dagger s_{y\boldsymbol{k'}}\sin(\boldsymbol{k}\cdot\boldsymbol{r})\sin(\boldsymbol{k'}\cdot\boldsymbol{r})], \\
\psi_y^\dagger(\boldsymbol{r})\psi_x(\boldsymbol{r}) = \frac{2}{L^3}{\sum_{\boldsymbol{k},\boldsymbol{k'}}}'[&c_{y\boldsymbol{k}}^\dagger c_{x\boldsymbol{k'}}\cos(\boldsymbol{k}\cdot\boldsymbol{r})\cos(\boldsymbol{k'}\cdot\boldsymbol{r}) + s_{y\boldsymbol{k}}^\dagger c_{x\boldsymbol{k'}}\sin(\boldsymbol{k}\cdot\boldsymbol{r})\cos(\boldsymbol{k'}\cdot\boldsymbol{r}) \\
&+c_{y\boldsymbol{k}}^\dagger s_{x\boldsymbol{k'}}\cos(\boldsymbol{k}\cdot\boldsymbol{r})\sin(\boldsymbol{k'}\cdot\boldsymbol{r}) + s_{y\boldsymbol{k}}^\dagger s_{x\boldsymbol{k'}}\sin(\boldsymbol{k}\cdot\boldsymbol{r})\sin(\boldsymbol{k'}\cdot\boldsymbol{r})]. \qquad (4.77)
\end{aligned}$$

The elements we need to calculate are

$$\begin{aligned}
\alpha_{i\boldsymbol{k}}^\dagger\beta_{j\boldsymbol{q}} &= \sqrt{\frac{\omega_k}{2}}\left(\pi_{i\boldsymbol{k}}^\alpha - \frac{1}{\omega_k}\frac{\partial}{\partial\pi_{i\boldsymbol{k}}^\alpha}\right)\sqrt{\frac{\omega_q}{2}}\left(\pi_{j\boldsymbol{q}}^\beta + \frac{1}{\omega_q}\frac{\partial}{\partial\pi_{j\boldsymbol{q}}^\beta}\right) \\
&= \frac{1}{2}\sqrt{\omega_k\omega_q}\left(\pi_{i\boldsymbol{k}}^\alpha\pi_{j\boldsymbol{q}}^\beta + \frac{\pi_{i\boldsymbol{k}}^\alpha}{\omega_q}\frac{\partial}{\partial\pi_{j\boldsymbol{q}}^\beta} - \frac{\pi_{j\boldsymbol{q}}^\beta}{\omega_k}\frac{\partial}{\partial\pi_{i\boldsymbol{k}}^\alpha} - \frac{1}{\omega_k}\delta_{\alpha i\boldsymbol{k};\beta j\boldsymbol{q}} - \frac{1}{\omega_k\omega_q}\frac{\partial^2}{\partial\pi_{i\boldsymbol{k}}^\alpha\partial\pi_{j\boldsymbol{q}}^\beta}\right), \qquad (4.78)
\end{aligned}$$

with the (abusive) notation $\alpha, \beta = c, s$, and $i, j = x, y, z$. Notice that the expression above includes mixed derivatives in the pion coordinates. Alternatively, we can integrate by parts to calculate only the elements

$$\langle\boldsymbol{\pi}^{c,s}|\beta_{j\boldsymbol{q}}|\psi_T\rangle = \sqrt{\frac{\omega_q}{2}}\left(\pi_{j\boldsymbol{q}}^\beta + \frac{1}{\omega_q}\frac{\partial}{\partial\pi_{j\boldsymbol{q}}^\beta}\right)\langle\boldsymbol{\pi}^{c,s}|\psi_T\rangle. \qquad (4.79)$$

The dot product with $(\alpha_{i\boldsymbol{k}}|\psi_T\rangle)^\dagger = \langle\psi_T|\alpha^\dagger_{i\boldsymbol{k}}$ gives the elements needed for the density calculation,

$$\left(\langle\psi_T|\alpha^\dagger_{i\boldsymbol{k}}\right)\left(\beta_{j\boldsymbol{q}}|\psi_T\rangle\right) = \int d\boldsymbol{\pi}^{c,s}\langle\psi_T|\boldsymbol{\pi}^{c,s}\rangle\sqrt{\frac{\omega_k}{2}}\left(\pi^\alpha_{i\boldsymbol{k}} - \frac{1}{\omega_k}\frac{\partial}{\partial\pi^\alpha_{i\boldsymbol{k}}}\right) \times\sqrt{\frac{\omega_q}{2}}\left(\pi^\beta_{j\boldsymbol{q}} + \frac{1}{\omega_q}\frac{\partial}{\partial\pi^\beta_{j\boldsymbol{q}}}\right)\langle\boldsymbol{\pi}^{c,s}|\psi_T\rangle. \tag{4.80}$$

4.2.3 Number of pions

The Hamiltonian describing the pions is that of a harmonic oscillator. Excitations of the pion field correspond to pion production. For each pion mode k, α, i we have

$$E_{\boldsymbol{k},\alpha,i} = \omega_k\left(N_{\boldsymbol{k},\alpha,i} + \frac{1}{2}\right), \tag{4.81}$$

where $N_{\boldsymbol{k},\alpha,i}$ is the number of pions. In the absence of coupling, all harmonic oscillators are in their respective ground-state and $N = 0$. So we can calculate how many pions are in a given mode by computing

$$N_{\boldsymbol{k},\alpha,i} = \frac{1}{\omega_k}\left[-\frac{1}{2}\frac{\partial^2}{\partial\pi^{\alpha 2}_{i\boldsymbol{k}}} + \frac{1}{2}\omega^2\pi^{\alpha 2}_{i\boldsymbol{k}}\right] - \frac{1}{2}. \tag{4.82}$$

4.2.4 Charge conservation

Unlike standard Green's function Monte Carlo (GFMC) calculations (Carlson *et al.* (2015b)), the sum of the nucleon charges in our QMC simulations,

$$Q_N = \sum_{i=1}^{A}\frac{(1+\tau_z^i)}{2}, \tag{4.83}$$

is not conserved configuration by configuration. This is due to the fact that the total charge of the system includes that of the charged pions,

$$Q = Q_N + Q_\pi, \tag{4.84}$$

with $Q_\pi \equiv (N_+ - N_-)$. The charged pion number operators are defined as

$$N_\pm = \sum_{\boldsymbol{k}} a^\dagger_{\pm\boldsymbol{k}}a_{\pm\boldsymbol{k}}, \tag{4.85}$$

where the creation and annihilation operators – see Appendix C for our conventions on the fields associated with charged pions – are given by

$$a^\dagger_{\pm\boldsymbol{k}} = \frac{1}{\sqrt{2}}\left[a^\dagger_{x\boldsymbol{k}} \mp i a^\dagger_{y\boldsymbol{k}}\right],$$
$$a_{\pm\boldsymbol{k}} = \frac{1}{\sqrt{2}}\left[a_{x\boldsymbol{k}} \pm i a_{y\boldsymbol{k}}\right]. \tag{4.86}$$

while for the neutral pion,

$$a_{0\boldsymbol{k}} = a_{z\boldsymbol{k}}\,. \tag{4.87}$$

The pion-charge is evaluated expressing the Cartesian isospin creation and annihilation operators in terms of the modes of the pion field. It simplifies some expressions to combine the isospin components into vectors in the usual way and define the pion mode amplitudes and their conjugate momenta as the isospin vectors,

$$\begin{aligned}\boldsymbol{\Pi}^{c,s}_{\boldsymbol{k}} &= \Pi^{c,s}_{x\boldsymbol{k}}\hat{\boldsymbol{x}} + \Pi^{c,s}_{y\boldsymbol{k}}\hat{\boldsymbol{y}} + \Pi^{c,s}_{z\boldsymbol{k}}\hat{\boldsymbol{z}},\\ \boldsymbol{\pi}^{c,s}_{\boldsymbol{k}} &= \pi^{c,s}_{x\boldsymbol{k}}\hat{\boldsymbol{x}} + \pi^{c,s}_{y\boldsymbol{k}}\hat{\boldsymbol{y}} + \pi^{c,s}_{z\boldsymbol{k}}\hat{\boldsymbol{z}}.\end{aligned} \tag{4.88}$$

The pion charge operator becomes

$$Q_\pi = -\hat{\boldsymbol{z}}\cdot{\sum_{\boldsymbol{k}}}'\left[\boldsymbol{\pi}^c_{\boldsymbol{k}}\times\boldsymbol{\Pi}^c_{\boldsymbol{k}} + \boldsymbol{\pi}^s_{\boldsymbol{k}}\times\boldsymbol{\Pi}^s_{\boldsymbol{k}}\right], \tag{4.89}$$

or as a differential operator on a wave function,

$$Q_\pi = i{\sum_{\boldsymbol{k}}}'\left[\pi^c_{x\boldsymbol{k}}\frac{\partial}{\partial\pi^c_{y\boldsymbol{k}}} - \pi^c_{y\boldsymbol{k}}\frac{\partial}{\partial\pi^c_{x\boldsymbol{k}}} + \pi^s_{x\boldsymbol{k}}\frac{\partial}{\partial\pi^s_{y\boldsymbol{k}}} - \pi^s_{y\boldsymbol{k}}\frac{\partial}{\partial\pi^s_{x\boldsymbol{k}}}\right]. \tag{4.90}$$

4.2.5 Perturbation theory

In this section we are interested in the first-order old-fashioned perturbation theory ground-state of a nucleon fixed at the origin. The interaction only couples to states with a single pion, hence the ground-state is

$$|O\rangle = |0\rangle + \sum_{m\neq 0}\frac{|m\rangle\langle m|V|0\rangle}{E_0 - E_m} + ... \tag{4.91}$$

and we wish to calculate the expected value of (one Cartesian component of) the pion density operator

$$\langle \rho_i(\boldsymbol{r}) \rangle = \frac{\langle O|\rho_i(\boldsymbol{r})|O\rangle}{\langle O|O\rangle}\,. \tag{4.92}$$

The interaction can only create a single pion in the intermediate state. The density operator does not change the number of pions, so the lowest order surviving term in the numerator is second order in the interaction. The next-order perturbation term contributes to the density at higher order. In the denominator, the normalization change is also second order in the interaction. Since the numerator is already second order, we can drop the normalization change, and take the denominator to be 1. Let us start with the numerator,

$$\left(\langle 0| + \sum_{m'\neq 0} \frac{\langle 0|V|m'\rangle\langle m'|}{E_0 - E_{m'}}\right) \rho_i(\boldsymbol{r}) \left(|0\rangle + \sum_{m\neq 0} \frac{|m\rangle\langle m|V|0\rangle}{E_0 - E_m}\right). \tag{4.93}$$

The action of V on the vacuum is given by

$$V|0\rangle = \frac{g_A}{2f_\pi}\sqrt{\frac{2}{L^3}}{\sum_{\boldsymbol{k}}}' \boldsymbol{\sigma}\cdot\boldsymbol{k}\tau_i(\pi^s_{i\boldsymbol{k}}\cos(\boldsymbol{k}\cdot\boldsymbol{x}) - \pi^c_{i\boldsymbol{k}}\sin(\boldsymbol{k}\cdot\boldsymbol{x}))|0\rangle. \tag{4.94}$$

We use Eq. (4.62) and

$$\begin{aligned}
c^\dagger_{i\boldsymbol{k}} &= \frac{1}{\sqrt{2}}(a^\dagger_{i\boldsymbol{k}} + a^\dagger_{i-\boldsymbol{k}}),\\
s^\dagger_{i\boldsymbol{k}} &= \frac{1}{i\sqrt{2}}(a^\dagger_{i\boldsymbol{k}} - a^\dagger_{i-\boldsymbol{k}}),\\
c_{i\boldsymbol{k}} &= \frac{1}{\sqrt{2}}(a_{i\boldsymbol{k}} + a_{i-\boldsymbol{k}}),\\
s_{i\boldsymbol{k}} &= -\frac{1}{i\sqrt{2}}(a_{i\boldsymbol{k}} - a_{i-\boldsymbol{k}}),
\end{aligned} \tag{4.95}$$

to write the π amplitudes in term of the creation/destruction operators,

$$
\begin{aligned}
V|0\rangle &= \frac{g_A}{2f_\pi}\sqrt{\frac{2}{L^3}}{\sum_{\boldsymbol{k}}}'\boldsymbol{\sigma}\cdot\boldsymbol{k}\tau_i\frac{1}{\sqrt{2\omega_k}}\frac{1}{\sqrt{2}}\Bigg[(-i(a^\dagger_{i\boldsymbol{k}}-a^\dagger_{i-\boldsymbol{k}}) \\
&\quad +i(a_{i\boldsymbol{k}}-a_{i-\boldsymbol{k}}))\cos(\boldsymbol{k}\cdot\boldsymbol{x})-(a^\dagger_{i\boldsymbol{k}}+a^\dagger_{i-\boldsymbol{k}}+a_{i\boldsymbol{k}}+a_{i-\boldsymbol{k}})\sin(\boldsymbol{k}\cdot\boldsymbol{x})\Bigg]|0\rangle \\
&= \frac{g_A}{2f_\pi}\sqrt{\frac{2}{L^3}}{\sum_{\boldsymbol{k}}}'\boldsymbol{\sigma}\cdot\boldsymbol{k}\tau_i\frac{1}{2\sqrt{\omega_k}}\Bigg[(-i\cos(\boldsymbol{k}\cdot\boldsymbol{x})-\sin(\boldsymbol{k}\cdot\boldsymbol{x}))|\boldsymbol{k}\rangle \\
&\quad +(i\cos(\boldsymbol{k}\cdot\boldsymbol{x})-\sin(\boldsymbol{k}\cdot\boldsymbol{x}))|-\boldsymbol{k}\rangle\Bigg] \\
&= \frac{g_A}{2f_\pi}\sqrt{\frac{2}{L^3}}{\sum_{\boldsymbol{k}}}'\boldsymbol{\sigma}\cdot\boldsymbol{k}\tau_i\frac{1}{2\sqrt{\omega_k}}\Big[ie^{-i\boldsymbol{k}\cdot\boldsymbol{x}}|\boldsymbol{k}\rangle-ie^{i\boldsymbol{k}\cdot\boldsymbol{x}}|-\boldsymbol{k}\rangle\Big] \\
&= \frac{g_A}{2f_\pi}\sqrt{\frac{2}{L^3}}{\sum_{\boldsymbol{k}}}\boldsymbol{\sigma}\cdot\boldsymbol{k}\tau_i\frac{i}{2\sqrt{\omega_k}}e^{-i\boldsymbol{k}\cdot\boldsymbol{x}}|\boldsymbol{k}\rangle. \qquad (4.96)
\end{aligned}
$$

Now let us calculate

$$
\begin{aligned}
&\sum_{m\neq 0}\left(\frac{1}{E_0-E_m}\right)|m\rangle\langle m|V|0\rangle = \\
&=\sum_{m\neq 0}\left(\frac{1}{E_0-E_m}\right)|m\rangle\langle m|\frac{g_A}{2f_\pi}\sqrt{\frac{2}{L^3}}{\sum_{\boldsymbol{k}}}\boldsymbol{\sigma}\cdot\boldsymbol{k}\tau_i\frac{i}{2\sqrt{\omega_k}}e^{-i\boldsymbol{k}\cdot\boldsymbol{x}}|\boldsymbol{k}\rangle = \\
&=\frac{g_A}{2f_\pi}\sqrt{\frac{2}{L^3}}{\sum_{\boldsymbol{k}\neq 0}}\boldsymbol{\sigma}\cdot\boldsymbol{k}\tau_i\frac{i}{2{\omega_k}^{3/2}}e^{-i\boldsymbol{k}\cdot\boldsymbol{x}}|\boldsymbol{k}\rangle, \qquad (4.97)
\end{aligned}
$$

where we used $E_0-E_k=\omega_k$. Similarly,

$$
\sum_{m'\neq 0}\left(\frac{1}{E_0-E_{m'}}\right)\langle 0|V|m'\rangle\langle m'| = \frac{g_A}{2f_\pi}\sqrt{\frac{2}{L^3}}{\sum_{\boldsymbol{k}\neq 0}}\boldsymbol{\sigma}\cdot\boldsymbol{k}\tau_i\frac{(-i)}{2{\omega_k}^{3/2}}e^{i\boldsymbol{k}\cdot\boldsymbol{x}}\langle\boldsymbol{k}|, \qquad (4.98)
$$

Finally, we set the position of the nucleon to the origin, $\boldsymbol{x}=0$, and we evaluate

$$
\begin{aligned}
\langle\rho_i\rangle &= \left(\sum_{m'\neq 0}\frac{\langle 0|V|m'\rangle\langle m'|}{E_0-E_{m'}}\right)\left(\frac{1}{L^3}\sum_{\boldsymbol{k}}\sum_{\boldsymbol{k}'}a^\dagger_{i\boldsymbol{k}}e^{-i\boldsymbol{k}\cdot\boldsymbol{r}}a_{i\boldsymbol{k}'}e^{i\boldsymbol{k}'\cdot\boldsymbol{r}}\right)\left(\sum_{m\neq 0}\frac{|m\rangle\langle m|V|0\rangle}{E_0-E_m}\right) \\
&= \left(\frac{g_A}{2f_\pi}\sqrt{\frac{2}{L^3}}\right)^2\frac{1}{L^3}\sum_{\boldsymbol{k},\boldsymbol{k}'}\boldsymbol{\sigma}\cdot\boldsymbol{k}\boldsymbol{\sigma}\cdot\boldsymbol{k}'\underbrace{\tau_i^2}_{=1}\frac{e^{-i(\boldsymbol{k}-\boldsymbol{k}')\cdot\boldsymbol{r}}}{4\omega_k^{3/2}\omega_{k'}^{3/2}}. \qquad (4.99)
\end{aligned}
$$

The result becomes

$$\begin{aligned}\langle\rho_i\rangle &= \left(\frac{g_A}{2f_\pi}\sqrt{\frac{2}{L^3}}\right)^2 \frac{1}{4L^3}\sum_{\boldsymbol{k}\boldsymbol{k}'}\frac{\boldsymbol{\sigma}\cdot\boldsymbol{k}}{\omega_k^{3/2}}\frac{\boldsymbol{\sigma}\cdot\boldsymbol{k}'}{\omega_k'^{3/2}}e^{i(\boldsymbol{k}'-\boldsymbol{k})\cdot\boldsymbol{r}} \\ &= \left(\frac{g_A}{2f_\pi}\sqrt{\frac{2}{L^3}}\right)^2 \frac{1}{4L^3}\left|\sum_{\boldsymbol{k}}\frac{\boldsymbol{k}e^{-i\boldsymbol{k}\cdot\boldsymbol{r}}}{\omega_k^{3/2}}\right|^2 . \end{aligned} \tag{4.100}$$

Dropping the $\boldsymbol{k}=0$ term that gives zero contribution, and combining the $-\boldsymbol{k}$ and $\boldsymbol{k}$ terms, we find

$$\begin{aligned}\langle\rho_i\rangle &= \left(\frac{g_A}{2f_\pi}\sqrt{\frac{2}{L^3}}\right)^2 \frac{1}{4L^3}\left|{\sum_{\boldsymbol{k}}}'\frac{\boldsymbol{k}2\sin(\boldsymbol{k}\cdot\boldsymbol{r})}{\omega_k^{3/2}}\right|^2 \\ &= \left(\frac{g_A}{2f_\pi}\sqrt{\frac{2}{L^3}}\right)^2 \frac{1}{L^3}\left|{\sum_{\boldsymbol{k}}}'\frac{\boldsymbol{k}\sin(\boldsymbol{k}\cdot\boldsymbol{r})}{\omega_k^{3/2}}\right|^2 . \end{aligned} \tag{4.101}$$

4.3 QMC Hamiltonian and wave functions

With our periodic box and the pion momentum cutoff, we now have a finite number of degrees of freedom, and can now use real-space quantum Monte Carlo methods to solve for the ground and low lying excited state properties of A nucleons. Our goal here is to be able to adapt variational Monte Carlo (VMC), GFMC, and Auxiliary field diffusion Monte Carlo (AFDMC) (Schmidt and Fantoni (1999)) methods to include the pion degrees of freedom. We therefore need to write our Hamiltonian in the A nucleon sector along with the pion fields, find good initial variational trial wave functions, and describe how we include the additional terms in the propagators. Note that, at variance with nuclear lattice approaches (Lee (2009)), we adopt a continuum representation for the eigenstates of the position operator.

4.3.1 The quantum Monte Carlo Hamiltonian

We write the pion operators using Eq. (4.88) and the momentum operator conjugate to the particle position operator, $\boldsymbol{r}_i$, as $\boldsymbol{P}_i$. Since the number of nucleons is

conserved, the Hamiltonian for the sector with A nucleons and the pion field can be written down immediately,

$$\begin{aligned}
H &= H_N + H_{\pi\pi} + H_{AV} + H_{WT}, \\
H_N &= \sum_{i=1}^{A}\left[\frac{P_i^2}{2M_P} + M_P + \beta_K P_i^2 + \delta M\right] + \sum_{i<j}^{A}\delta_{R_0}(\boldsymbol{r}_i-\boldsymbol{r}_j)[C_s + C_T\boldsymbol{\sigma}_i\cdot\boldsymbol{\sigma}_j], \\
H_{\pi\pi} &= \frac{1}{2}{\sum_{\boldsymbol{k}}}'\left[|\boldsymbol{\Pi}^c_{\boldsymbol{k}}|^2 + \omega_{\boldsymbol{k}}^2|\boldsymbol{\pi}^c_{\boldsymbol{k}}|^2 + |\boldsymbol{\Pi}^s_{\boldsymbol{k}}|^2 + \omega_{\boldsymbol{k}}^2|\boldsymbol{\pi}^s_{\boldsymbol{k}}|^2\right], \\
H_{AV} &= \sum_{i=1}^{A}\frac{g_A}{2f_\pi}\sqrt{\frac{2}{L^3}}{\sum_{\boldsymbol{k}}}'\left\{\boldsymbol{\sigma}_i\cdot\boldsymbol{k}\left[\boldsymbol{\tau}_i\cdot\boldsymbol{\pi}^s_{\boldsymbol{k}}\cos(\boldsymbol{k}\cdot\boldsymbol{r}_i) - \boldsymbol{\tau}_i\cdot\boldsymbol{\pi}^c_{\boldsymbol{k}}\sin(\boldsymbol{k}\cdot\boldsymbol{r}_i)\right]\right\}, \\
H_{WT} &= \sum_{i=1}^{A}\frac{1}{2f_\pi^2L^3}\boldsymbol{\tau}_i\cdot\Bigg[{\sum_{\boldsymbol{k}}}'\cos(\boldsymbol{k}\cdot\boldsymbol{r}_i)\boldsymbol{\pi}^c_{\boldsymbol{k}}\times{\sum_{\boldsymbol{q}}}'\cos(\boldsymbol{q}\cdot\boldsymbol{r}_i)\boldsymbol{\Pi}^c_{\boldsymbol{q}} \\
&+ {\sum_{\boldsymbol{k}}}'\cos(\boldsymbol{k}\cdot\boldsymbol{r}_i)\boldsymbol{\pi}^c_{\boldsymbol{k}}\times{\sum_{\boldsymbol{q}}}'\sin(\boldsymbol{q}\cdot\boldsymbol{r}_i)\boldsymbol{\Pi}^s_{\boldsymbol{q}} \\
&+ {\sum_{\boldsymbol{k}}}'\sin(\boldsymbol{k}\cdot\boldsymbol{r}_i)\boldsymbol{\pi}^s_{\boldsymbol{k}}\times{\sum_{\boldsymbol{q}}}'\cos(\boldsymbol{q}\cdot\boldsymbol{r}_i)\boldsymbol{\Pi}^c_{\boldsymbol{q}} \\
&+ {\sum_{\boldsymbol{k}}}'\sin(\boldsymbol{k}\cdot\boldsymbol{r}_i)\boldsymbol{\pi}^s_{\boldsymbol{k}}\times{\sum_{\boldsymbol{q}}}'\sin(\boldsymbol{q}\cdot\boldsymbol{r}_i)\boldsymbol{\Pi}^s_{\boldsymbol{q}}\Bigg],
\end{aligned} \tag{4.102}$$

where the sums over i and j are over the nucleons, M_P is the physical nucleon mass, and $\delta_{R_0}(\boldsymbol{r}_i-\boldsymbol{r}_j)$ is a smeared out delta function for the contact term which we take to be the same form as that used in local chiral EFT potentials (Gezerlis *et al.* (2014)),

$$\delta_{R_0}(\boldsymbol{r}) = \frac{1}{\pi\Gamma(3/4)R_0^3}\exp\left[-(|\boldsymbol{r}|/R_0)^4\right], \tag{4.103}$$

where Γ is the gamma function, and $R_0 = 1.2$ fm. We are aware that there may be shortcomings in employing the regulator of Eq. (4.103) (Kaplan *et al.* (1996); Nogga *et al.* (2005)). However they are mitigated by the fact we focus on deuteron properties, which has a relatively small d-wave component, and we employ fixed pion masses. This regulator choice will be thoroughly analyzed, and might be revisited, for larger nuclei. The low-energy constants C_S and C_T need to be adjusted to agree

with experiment. We fit the deuteron and the neutron-neutron scattering length in section 4.9.5. There are, of course, many other possible choices for the contact term.

Notice that we have two distinct mass counter terms in H_N. We call β_K the kinetic mass counter term and δM the rest mass counter term. The values are not simply related because we are employing a cutoff on the three-momentum of the pion modes that explicitly breaks Lorentz invariance. The kinetic energy bare mass is given by $\frac{M_P}{1+2\beta_K M_P}$, while the bare rest mass is $M_P + \delta M$.

Our resulting field theory Hamiltonian is in the same form as the Hamiltonian of a nonrelativistic many-body quantum system, and all standard methods for such a system can be applied.

In this work we will sometimes neglect the Weinberg-Tomozawa H_{WT} term in our initial QMC calculations. In general we have found that it is small enough to be included perturbatively. This term is known to be relevant only in the isovector channel, and the s-wave πN scattering length is relatively small (Robilotta and Wilkin (1978); Weinberg (1992)).

4.3.2 Trial wave functions

Analogously to standard real-space QMC methods, we first construct an accurate ground state trial wave function for the Hamiltonian. In GFMC or AFDMC methods, the trial function performs the dual role of lowering the statistical errors and constraining the path integral to control the fermion sign or phase problem. For small numbers of nucleons where the fermion sign/phase problem is under control, our QMC methods will give exact results within statistical errors independent of the trial function. A good trial function in that case keeps the statistical errors small.

Standard GFMC and AFDMC methods use the position eigenbasis for the nucleons. Here we add to this nucleon basis the eigenbasis of the pion mode amplitudes, and write our trial wave functions to be

$$\Psi_T(R,S,\Pi) = \langle RS\Pi|\Psi_T\rangle, \tag{4.104}$$

where R represents the $3A$ coordinates of the nucleons, Π represents the $3N_{\boldsymbol{k}}$ pion mode amplitudes, and S the spin-isospin of the nucleons.

If we assume the pion motion is significantly faster than the nucleons, then a Born-Oppenheimer approximation where we initially neglect the nucleon mass can guide our construction of a trial wave function for the full dynamical system. We therefore initially analyze the problem without the nucleon kinetic energy and the Weinberg-Tomozawa terms in the Hamiltonian, assuming that they are smaller than the axial-vector pion-nucleon terms. Defining

$$\begin{aligned}
\boldsymbol{B}^c_{\boldsymbol{k}} &\equiv \sqrt{\frac{2}{L^3}}\frac{g_A}{f_\pi}\sum_{i=1}^{A}\boldsymbol{\tau}_i\sin(\boldsymbol{k}\cdot\boldsymbol{r}_i)\boldsymbol{\sigma}_i\cdot\boldsymbol{k},\\
\boldsymbol{B}^s_{\boldsymbol{k}} &\equiv -\sqrt{\frac{2}{L^3}}\frac{g_A}{f_\pi}\sum_{i=1}^{A}\boldsymbol{\tau}_i\cos(\boldsymbol{k}\cdot\boldsymbol{r}_i)\boldsymbol{\sigma}_i\cdot\boldsymbol{k},
\end{aligned} \tag{4.105}$$

allows us to complete the squares in these terms of the Hamiltonian, yielding

$$\begin{aligned}
H_{\pi\pi}+H_{AV} &= \frac{1}{2}{\sum_{\boldsymbol{k}}}'\Big[|\boldsymbol{\Pi}^c_{\boldsymbol{k}}|^2+\omega_{\boldsymbol{k}}^2|\tilde{\boldsymbol{\pi}}^c_{\boldsymbol{k}}|^2+|\boldsymbol{\Pi}^s_{\boldsymbol{k}}|^2+\omega_{\boldsymbol{k}}^2|\tilde{\boldsymbol{\pi}}^s_{\boldsymbol{k}}|^2\\
&\quad -\frac{1}{4\omega_k^2}\left(|\boldsymbol{B}^c_{\boldsymbol{k}}|^2+|\boldsymbol{B}^s_{\boldsymbol{k}}|^2\right)\Big]
\end{aligned} \tag{4.106}$$

with $\tilde{\boldsymbol{\pi}}^{c,s}_{\boldsymbol{k}} \equiv \boldsymbol{\pi}^{c,s}_{i\boldsymbol{k}} - \boldsymbol{B}^{c,s}_{\boldsymbol{k}}/2\omega_k^2$.

The $\tilde{\boldsymbol{\pi}}^{c,s}_{\boldsymbol{k}}$ operators do not commute because of the nucleon spin-isospin operators contained in $\boldsymbol{B}^{c,s}_{\boldsymbol{k}}$. If instead these spin-isospin operators were c-numbers, we could immediately write the ground-state wave function for the pions. This suggests taking the form for trial wave function to be

$$\langle RS\Pi|\Psi_T\rangle = \langle RS\Pi|\exp\left[-{\sum_{\boldsymbol{k}}}'\frac{\omega_k}{2}(|\tilde{\boldsymbol{\pi}}^c_{\boldsymbol{k}}|^2+|\tilde{\boldsymbol{\pi}}^s_{\boldsymbol{k}}|^2)\right]|\Phi\rangle\,. \tag{4.107}$$

where $|\Phi\rangle$ is an A nucleon model state. Writing in terms of the original pion coordinates, this wave function becomes

$$\langle RS\Pi|\Psi_T\rangle = \langle RS\Pi| \exp\left\{ -\sum_{\boldsymbol{k}}{}' \left[\frac{\omega_k}{2}(|\boldsymbol{\pi}^c_{\boldsymbol{k}}|^2 + |\boldsymbol{\pi}^s_{\boldsymbol{k}}|^2) + \frac{\alpha_k}{2\omega_k}\left(\boldsymbol{\pi}^c_{\boldsymbol{k}}\cdot\boldsymbol{B}^c_{\boldsymbol{k}} + \boldsymbol{\pi}^s_{\boldsymbol{k}}\cdot\boldsymbol{B}^s_{\boldsymbol{k}}\right) \right.\right.$$
$$\left.\left. -\frac{1}{4}\omega_k\alpha_k^2 G_k^2 \sum_{i<j}^{A} \boldsymbol{\tau}_i\cdot\boldsymbol{\tau}_j\boldsymbol{\sigma}_i\cdot\boldsymbol{k}\boldsymbol{\sigma}_j\cdot\boldsymbol{k}\cos(\boldsymbol{k}\cdot\boldsymbol{r}_{ij}) \right] \right\} |\Phi\rangle\,. \tag{4.108}$$

where $\boldsymbol{r}_{ij} = \boldsymbol{r}_i - \boldsymbol{r}_j$,

$$G_k = \frac{1}{\omega_k^2}\frac{g_A}{f_\pi}\sqrt{\frac{2}{L^3}}\,, \tag{4.109}$$

and we drop terms that only contribute to the overall normalization. We have also introduced the variational parameters α_k, which rescale the coupling for different momenta.

Eq. (4.108) is the standard form we will take for our trial functions. The two-body terms do not contain pion amplitudes; they look like two-body correlations typically included in variational calculations, and therefore they could be replaced or modified with other correlation forms that may be more convenient for calculations. The pion-nucleon correlation terms look very much like the AFDMC propagators, as it would be expected from the fact that the auxiliary fields in AFDMC can be thought of as replacing the real pion fields.

4.4 One nucleon

4.4.1 Lowest order self energy from nonrelativistic pion nucleon Hamiltonian

To estimate the magnitude of the mass counter terms, we first calculate these terms in perturbation theory. These should agree with our full Monte Carlo calculations for a weak coupling and when the cutoff is small. In this calculation we consider only the lowest order interaction term, represented by the diagram of Fig. 4.1. First, we need

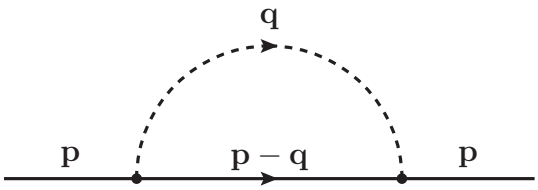

Figure 4.1: Diagram for the lowest order self-energy $\Sigma(E, \boldsymbol{p})$.

to compute the propagators for the nucleon and the pions (harmonic oscillators). The nonrelativistic propagator for the nucleon of mass M is

$$\begin{aligned} G(\boldsymbol{r}-\boldsymbol{r}', t-t') &= -iT\langle 0|N(\boldsymbol{r}, t)N^\dagger(\boldsymbol{r}', t')|0\rangle \\ &= -i\theta(t-t')\frac{1}{L^3}\sum_{\boldsymbol{p}} e^{i\boldsymbol{p}\cdot(\boldsymbol{r}-\boldsymbol{r}')}e^{-i\frac{p^2}{2M}(t-t')}. \end{aligned} \tag{4.110}$$

Writing the Fourier transform as

$$G(\boldsymbol{r}-\boldsymbol{r}', t-t') = \frac{1}{L^3}\sum_{\boldsymbol{p}}\frac{d\omega}{2\pi}e^{i\boldsymbol{p}\cdot(\boldsymbol{r}-\boldsymbol{r}')-i\omega(t-t')}G(\boldsymbol{p}, \omega), \tag{4.111}$$

yields

$$\begin{aligned} G(\boldsymbol{p}, \omega) &= -i\int_{-\infty}^{\infty} dt\Theta(t)e^{i\left(\omega-\frac{p^2}{2M}\right)t-\eta t} = -i\int_0^{\infty} dte^{i\left(\omega-\frac{p^2}{2M}+i\eta\right)t} \\ &= \frac{1}{\omega-\frac{p^2}{2M}+i\eta}, \end{aligned} \tag{4.112}$$

where the $-\eta t$ with η a positive infinitesimal is added to converge the integral at the upper limit. The harmonic oscillator propagator needed for an oscillator with frequency ω_0 and mass $m = 1$ is

$$\begin{aligned} G_{HO}(t-t') &= -iT\langle 0|x(t)x(t')|0\rangle = -iT\langle 0|\frac{a(t)+a^\dagger(t)}{\sqrt{2\omega_0}}\frac{a(t')+a^\dagger(t')}{\sqrt{2\omega_0}}|0\rangle \\ &= -i\frac{1}{2\omega_0}\left[\Theta(t-t')e^{-i\omega_0(t-t')}+\Theta(t'-t)e^{-i\omega_0(t'-t)}\right] \\ &= -\frac{i}{2\omega_0}e^{-i\omega_0|t-t'|}. \end{aligned} \tag{4.113}$$

Fourier transforming in time yields

$$\begin{aligned} G_{HO}(\omega) &= -\frac{i}{2\omega_0}\left[\int_0^\infty dt e^{i(\omega-\omega_0+i\eta)t} + \int_{-\infty}^0 dt e^{i(\omega+\omega_0-i\eta)t}\right] \\ &= \frac{1}{2\omega_0}\left[\frac{1}{\omega-\omega_0+i\eta} - \frac{1}{\omega+\omega_0-i\eta}\right] = \frac{1}{\omega^2-\omega_0^2+i\eta}. \end{aligned} \tag{4.114}$$

Equations (4.112) and (4.114), together with standard Feynman diagram rules (Fetter and Walecka (2003)), provide an expression for the self-energy,

$$\Sigma(E,\boldsymbol{p}) = -i3\left(\frac{g_A}{2f_\pi}\right)^2 \int_{-\infty}^\infty \frac{d\omega}{2\pi}\frac{1}{L^3}\sum_{\boldsymbol{q}} \frac{q^2}{(E-\omega-\frac{|\boldsymbol{p}-\boldsymbol{q}|^2}{2M}+i\eta)}\frac{1}{(\omega^2-\omega_q^2+i\eta)}, \tag{4.115}$$

where the factor of 3 comes from $\boldsymbol{\tau}^1\cdot\boldsymbol{\tau}^2$ (or the 3 types of hermitian pions), and $\omega_q^2 = q^2+m_\pi^2$. The ω integral has poles at $E-|\boldsymbol{p}-\boldsymbol{q}|^2/2M+i\eta$ and $\pm\omega_q\mp i\eta$. We can chose the integration contour along a semicircle in either half plane, a counterclockwise contour that encloses $-w_q+i\eta$ or a clockwise with $w_q-i\eta$. The self-energy is given by

$$\Sigma(E,\boldsymbol{p}) = -\frac{3}{2}\left(\frac{g_A}{2f_\pi}\right)^2 \frac{1}{L^3}\sum_{\boldsymbol{q}} \frac{q^2}{\left(E-\frac{|\boldsymbol{p}-\boldsymbol{q}|^2}{2M}-\omega_q\right)\omega_q}. \tag{4.116}$$

The single-nucleon spectrum is dictated by the pole of the Green's function,

$$E = \left(\frac{1}{2M_P}+\beta_K\right)p^2 + M_p + \delta M + \Sigma(E,\boldsymbol{p})\,. \tag{4.117}$$

We must adjust β_K and δM so that at small momentum, $E = M_P + \frac{p^2}{2M_P}$, or

$$\beta_K p^2 + \delta M + \Sigma\left(M_P+\frac{p^2}{2M_P},\boldsymbol{p}\right) = 0\,. \tag{4.118}$$

Expanding in powers of p, we find,

$$0 = \delta M - \frac{3}{2}\left(\frac{g_A}{2f_\pi}\right)^2 \frac{1}{L^3}\sum_{\boldsymbol{q}}\frac{q^2}{\omega_q D_q}, \tag{4.119}$$

$$
\begin{aligned}
0 &= \beta_K + \beta_K \frac{3}{2} \left(\frac{g_A}{2f_\pi} \right)^2 \frac{1}{L^3} \sum_{\boldsymbol{q}} \frac{q^2}{\omega_q D_q^2} \\
&\quad - \left(\frac{1}{M_P} + 2\beta_K \right)^2 \frac{1}{2} \left(\frac{g_A}{2f_\pi} \right)^2 \frac{1}{L^3} \sum_{\boldsymbol{q}} \frac{q^4}{\omega_q D_q^3},
\end{aligned}
\tag{4.120}
$$

where

$$
D_q = \delta M + \left(\frac{1}{2M_P} + \beta_K \right) q^2 + \omega_q \,. \tag{4.121}
$$

Solving these self consistently gives the lowest order values of δM and β_K. We see from the form above, that the kinetic mass renormalization is small.

4.4.2 Pion derivatives

The trial wave functions contain terms which are exponentials with arguments that are linear in the pion field amplitudes and contain nucleon operators. We wish to take derivatives with respect to the pion field amplitudes. These exponentials have the form

$$
\exp\left(\pi_1 \sum_i O_i^{(1)} + \pi_2 \sum_i O_i^{(2)} + ... \right) \tag{4.122}
$$

where π_j are the different pion field amplitudes (we use j below as a label for the momentum, Cartesian component and sine/cosine mode, for brevity, in this section only), and $O_i^{(1)}$ is the particular linear combination of the $\sigma_{i\alpha}\tau_{i\beta}$ terms for nucleon i that π_1 couples to. The $O_i^{(1)}$, $O_i^{(2)}$, ..., terms which act on the same particle do not commute, but the terms which act on different particles do commute. We can write this exponential as a product of exponentials for each nucleon as

$$
\exp\left(\sum_j \pi_j O_i^{(j)} \right) . \tag{4.123}
$$

Defining this single nucleon exponential as e^O, with real pion fields, O is Hermitian. We want to calculate a derivative $\partial e^O/\partial x$, where x is one of the pion field amplitudes. If we write $e^O = [e^{O/N}]^N$, then we have,

$$\begin{aligned}\frac{\partial e^O}{\partial x} &= \left(\frac{\partial e^{O/N}}{\partial x}\right)\underbrace{e^{O/N}\dots e^{O/N}}_{N-1 \text{ times}} + e^{O/N}\left(\frac{\partial e^{O/N}}{\partial x}\right)\underbrace{e^{O/N}\dots e^{O/N}}_{N-2 \text{ times}} + \dots \\ &\quad + \underbrace{e^{O/N}\dots e^{O/N}}_{N-1 \text{ times}}\left(\frac{\partial e^{O/N}}{\partial x}\right) \\ &= \sum_{j=0}^{N-1} e^{O(N-j-1)/N}\left(\frac{\partial e^{O/N}}{\partial x}\right)e^{Oj/N}. \end{aligned} \tag{4.124}$$

In the limit $N \to \infty$ the summation goes to an integral, and we make the substitution $\alpha = j/N$,

$$\frac{\partial}{\partial x}e^O = \int_0^1 d\alpha e^{O(1-\alpha)}\frac{\partial O}{\partial x}e^{O\alpha}. \tag{4.125}$$

Since O is Hermitian, we have $O|n\rangle = \lambda_n|n\rangle$, with $|n\rangle$ orthonormal,

$$\frac{\partial}{\partial x}e^O = \sum_{nm}\int_0^1 d\alpha |n\rangle e^{\lambda_n(1-\alpha)}\langle n|\frac{\partial O}{\partial x}|m\rangle e^{\lambda_m\alpha}\langle m| = \sum_{nm}|n\rangle\frac{e^{\lambda_m}-e^{\lambda_n}}{\lambda_m-\lambda_n}\langle n|\frac{\partial O}{\partial x}|m\rangle\langle m|\,. \tag{4.126}$$

For the diagonal or degenerate case, where $m = n$ or $\lambda_m = \lambda_n$, $\frac{e^{\lambda_m}-e^{\lambda_n}}{\lambda_m-\lambda_n} \to e^{\lambda_n}$.

Because O is linear in x, the laplacian does not contain terms with $\partial^2 O/\partial x^2$, hence:

$$\begin{aligned}\frac{\partial^2}{\partial x^2}e^O &= 2\sum_{nml}\int_0^1 d\beta\int_0^{1-\beta} d\alpha |n\rangle e^{\lambda_n(1-\alpha-\beta)}\langle n|\frac{\partial O}{\partial x}|m\rangle e^{\lambda_m\alpha}\langle m|\frac{\partial O}{\partial x}|l\rangle e^{\lambda_l\beta}\langle l| = \\ &= 2\sum_{nml}|n\rangle\langle n|\frac{\partial O}{\partial x}|m\rangle\langle m|\frac{\partial O}{\partial x}|l\rangle\langle l|f_{nml}, \end{aligned} \tag{4.127}$$

$$f_{nml} = \begin{cases} \frac{e^{\lambda_n}}{2}, & \text{if } \lambda_n = \lambda_m = \lambda_l \\ \frac{e^{\lambda_l} - e^{\lambda_m}}{(\lambda_l - \lambda_m)(\lambda_m - \lambda_n)} + \frac{e^{\lambda_l} - e^{\lambda_n}}{(\lambda_l - \lambda_n)(\lambda_n - \lambda_m)} & \text{if } \lambda_n \neq \lambda_m \neq \lambda_l \\ \frac{e^{\lambda_l} + e^{\lambda_n}(\lambda_n - \lambda_l - 1)}{(\lambda_l - \lambda_n)^2} & \text{if } \lambda_n = \lambda_m \neq \lambda_l \\ \frac{e^{\lambda_m} + e^{\lambda_n}(\lambda_n - \lambda_m - 1)}{(\lambda_m - \lambda_n)^2} & \text{if } \lambda_n = \lambda_l \neq \lambda_m \\ \frac{e^{\lambda_n} + e^{\lambda_m}(\lambda_m - \lambda_n - 1)}{(\lambda_m - \lambda_n)^2} & \text{if } \lambda_m = \lambda_l \neq \lambda_n \end{cases} \tag{4.128}$$

For mixed derivatives the result is similar,

$$\begin{aligned} \frac{\partial^2}{\partial x \partial y} e^O = \sum_{nml} \int_0^1 d\beta \int_0^{1-\beta} d\alpha \Bigg[& |n\rangle e^{\lambda_n (1-\alpha-\beta)} \langle n| \frac{\partial O}{\partial x} |m\rangle e^{\lambda_m \alpha} \langle m| \frac{\partial O}{\partial y} |l\rangle e^{\lambda_l \beta} \langle l| \\ & + |n\rangle e^{\lambda_n (1-\alpha-\beta)} \langle n| \frac{\partial O}{\partial y} |m\rangle e^{\lambda_m \alpha} \langle m| \frac{\partial O}{\partial x} |l\rangle e^{\lambda_l \beta} \langle l| \Bigg] \\ = \sum_{nml} \left[|n\rangle\langle n| \frac{\partial O}{\partial x} |m\rangle\langle m| \frac{\partial O}{\partial y} |l\rangle\langle l| + |n\rangle\langle n| \frac{\partial O}{\partial y} |m\rangle\langle m| \frac{\partial O}{\partial x} |l\rangle\langle l| \right] & f_{nml}. \end{aligned} \tag{4.129}$$

Notice that the result agrees with the second derivative of Eq. (4.127) if we take $x = y$.

4.5 Two fixed nucleons

4.5.1 Implementation

We can write the wave function as

$$\psi_T(\boldsymbol{\pi}^c_{\boldsymbol{k}}, \boldsymbol{\pi}^s_{\boldsymbol{k}}, \boldsymbol{x}_n, s_1, s_2) = \langle s_1 s_2 | \psi_{HO} e^{O_1} e^{O_2} e^{O_{12}} | \phi \rangle, \tag{4.130}$$

with

$$\psi_{HO} = \exp\left[\sum_{\boldsymbol{k}}{}' - \frac{\sqrt{k^2 + m_\pi^2}}{2} \left\{ \boldsymbol{\pi}^{c2}_{\boldsymbol{k}} + \boldsymbol{\pi}^{s2}_{\boldsymbol{k}} \right\} \right], \tag{4.131}$$

$$
\begin{aligned}
O_{12} &= \sum_{\boldsymbol{k}}{}' -\frac{\sqrt{k^2+m_\pi^2}}{2}\frac{1}{4}\alpha_k^2 G_k^2\left(2\boldsymbol{\tau}^1\cdot\boldsymbol{\tau}^2\cos(\boldsymbol{k}\cdot(\boldsymbol{x}_1-\boldsymbol{x}_2))\sum_{i,j}\sigma_i^1 k_i\sigma_j^2 k_j\right),\\
O_1 &= \sum_{\boldsymbol{k}}{}' -\frac{\sqrt{k^2+m_\pi^2}}{2}\alpha_k G_k \boldsymbol{k}\cdot\boldsymbol{\sigma}^1\left[-\sin(\boldsymbol{k}\cdot\boldsymbol{x}_1)\boldsymbol{\pi}_{\boldsymbol{k}}^c\cdot\boldsymbol{\tau}^1+\cos(\boldsymbol{k}\cdot\boldsymbol{x}_1)\boldsymbol{\pi}_{\boldsymbol{k}}^s\cdot\boldsymbol{\tau}^1\right],\\
O_2 &= \sum_{\boldsymbol{k}}{}' -\frac{\sqrt{k^2+m_\pi^2}}{2}\alpha_k G_k \boldsymbol{k}\cdot\boldsymbol{\sigma}^2\left[-\sin(\boldsymbol{k}\cdot\boldsymbol{x}_2)\boldsymbol{\pi}_{\boldsymbol{k}}^c\cdot\boldsymbol{\tau}^2+\cos(\boldsymbol{k}\cdot\boldsymbol{x}_2)\boldsymbol{\pi}_{\boldsymbol{k}}^s\cdot\boldsymbol{\tau}^2\right].
\end{aligned}
\tag{4.132}
$$

Notice that $\psi_{HO}e^{O_1}e^{O_2}e^{O_{12}}$ is symmetric under the exchange of $1\leftrightarrow 2$, and O_{12} does not depend on the pion coordinates. Hence, the pion derivatives are

$$
\begin{aligned}
\frac{\partial\psi_T}{\partial\pi_k} &= \langle s_1 s_2|\frac{\partial\psi_{HO}}{\partial\pi_k}e^{O_1}e^{O_2}e^{O_{12}}|\phi\rangle\\
&\quad+\langle s_1 s_2|\psi_{HO}\left(\frac{\partial e^{O_1}}{\partial\pi_k}e^{O_2}+e^{O_1}\frac{\partial e^{O_2}}{\partial\pi_k}\right)e^{O_{12}}|\phi\rangle,
\end{aligned}
\tag{4.133}
$$

and

$$
\begin{aligned}
\frac{\partial^2\psi_T}{\partial\pi_k^2} &= \langle s_1 s_2|\frac{\partial^2\psi_{HO}}{\partial\pi_k^2}e^{O_1}e^{O_2}e^{O_{12}}|\phi\rangle+2\langle s_1 s_2|\frac{\partial\psi_{HO}}{\partial\pi_k}\frac{\partial e^{O_1}}{\partial\pi_k}e^{O_2}e^{O_{12}}|\phi\rangle\\
&\quad+2\langle s_1 s_2|\frac{\partial\psi_{HO}}{\partial\pi_k}e^{O_1}\frac{\partial e^{O_2}}{\partial\pi_k}e^{O_{12}}|\phi\rangle+\langle s_1 s_2|\psi_{HO}\frac{\partial^2 e^{O_1}}{\partial\pi_k^2}e^{O_2}e^{O_{12}}|\phi\rangle\\
&\quad+2\langle s_1 s_2|\psi_{HO}\frac{\partial e^{O_1}}{\partial\pi_k}\frac{\partial e^{O_2}}{\partial\pi_k}e^{O_{12}}|\phi\rangle+\langle s_1 s_2|\psi_{HO}e^{O_1}\frac{\partial^2 e^{O_2}}{\partial\pi_k^2}e^{O_{12}}|\phi\rangle.
\end{aligned}
\tag{4.134}
$$

We want to implement the wave function of Eq. (4.130) efficiently. The e^{O_1} and e^{O_2} can be written as 4x4 matrices, but the term $e^{O_{12}}$ is, in principle, a 16x16 matrix. Let us write $e^{O_{12}}$ as

$$
e^{O_{12}} = \exp\left[(\boldsymbol{\sigma}^1\cdot\overleftrightarrow{A}\cdot\boldsymbol{\sigma}^2)(\boldsymbol{\tau}^1\cdot\boldsymbol{\tau}^2)\right],
\tag{4.135}
$$

with $\overleftrightarrow{A}$ being a real symmetric tensor,

$$
A_{\alpha\beta} = \sum_{\boldsymbol{k}}{}' -\frac{\sqrt{k^2+m_\pi^2}}{2}\frac{1}{4}\alpha_k^2 G_k^2\left(2\cos(\boldsymbol{k}\cdot(\boldsymbol{x}_1-\boldsymbol{x}_2))k_\alpha k_\beta\right).
\tag{4.136}
$$

The real eigenvalues λ_n and the real eigenvectors $|n\rangle$ are such that $A|n\rangle = \lambda_n|n\rangle$, hence

$$\begin{aligned}\boldsymbol{\sigma}^1 \cdot \overleftrightarrow{A} \cdot \boldsymbol{\sigma}^2 &= \sum_{\alpha,\beta} \sigma^1_\alpha A_{\alpha\beta} \sigma^2_\beta = \sum_{\alpha,\beta,n} \sigma^1_\alpha \lambda_n \langle\alpha|n\rangle\langle n|\beta\rangle \sigma^2_\beta \\ &= \sum_n \lambda_n \left(\sum_\alpha \sigma^1_\alpha \langle\alpha|n\rangle\right)\left(\sum_\beta \langle n|\beta\rangle \sigma^2_\beta\right). \end{aligned} \tag{4.137}$$

Notice that $\langle n|\beta\rangle = \langle\beta|n\rangle$ because the eigenvectors are real, thus we can define a rotated basis where

$$\sigma'_i = \sum_\alpha \sigma_\alpha \langle\alpha|i\rangle, \tag{4.138}$$

and the σ'_i obey the usual commutation relations. In this primed basis,

$$\boldsymbol{\sigma}^1 \cdot \overleftrightarrow{A} \cdot \boldsymbol{\sigma}^2 = \sum_n \lambda_n \sigma_n^{1'} \sigma_n^{2'} \equiv \sum_n \lambda_n S_n, \tag{4.139}$$

where we defined $S_n \equiv \sigma_n^{1'}\sigma_n^{2'}$. These operators commute,

$$[S_x, S_y] = \sigma_x^{1'}\sigma_x^{2'}\sigma_y^{1'}\sigma_y^{2'} - \sigma_y^{1'}\sigma_y^{2'}\sigma_x^{1'}\sigma_x^{2'} = i\sigma_z^{1'} i\sigma_z^{2'} - (-i\sigma_z^{1'})(-i\sigma_z^{2'}) = 0, \tag{4.140}$$

and similarly for cyclic permutations. Because they commute, we can write

$$e^{O_{12}} = \exp\left[(\boldsymbol{\sigma}^1 \cdot \overleftrightarrow{A} \cdot \boldsymbol{\sigma}^2)(\boldsymbol{\tau}^1 \cdot \boldsymbol{\tau}^2)\right] = \prod_i \exp\left[(\lambda_i S_i)(\boldsymbol{\tau}^1 \cdot \boldsymbol{\tau}^2)\right]. \tag{4.141}$$

Now we want to linearize the exponentials, that is,

$$e^{\lambda_i S_i (\boldsymbol{\tau}^1 \cdot \boldsymbol{\tau}^2)} = A_i \mathbf{1} + B_i (\boldsymbol{\tau}^1 \cdot \boldsymbol{\tau}^2) + C_i S_i + D_i S_i (\boldsymbol{\tau}^1 \cdot \boldsymbol{\tau}^2). \tag{4.142}$$

We use the fact that the isospin singlet (triplet) is an eigenstate of $\boldsymbol{\tau}^1 \cdot \boldsymbol{\tau}^2$ with eigenvalue -3 (1) to get the equations

$$\begin{aligned} e^{\lambda_i S_i} &= \cosh(\lambda_i) + S_i \sinh(\lambda_i) = A_i + B_i + (C_i + D_i) S_i \\ e^{-3\lambda_i S_i} &= \cosh(3\lambda_i) - S_i \sinh(3\lambda_i) = A_i - 3B_i + (C_i - 3D_i) S_i. \end{aligned} \tag{4.143}$$

Solving for the coefficients yields

$$\begin{aligned} A_i &= \frac{1}{4}\left[3\cosh(\lambda_i) + \cosh(3\lambda_i)\right], \\ B_i &= \frac{1}{4}\left[\cosh(\lambda_i) - \cosh(3\lambda_i)\right], \\ C_i &= \frac{1}{4}\left[3\sinh(\lambda_i) - \sinh(3\lambda_i)\right], \\ D_i &= \frac{1}{4}\left[\sinh(\lambda_i) + \sinh(3\lambda_i)\right]. \end{aligned} \tag{4.144}$$

Finally,

$$\begin{aligned} e^{O_{12}} &= e^{\lambda_x S_x(\boldsymbol{\tau}^1\cdot\boldsymbol{\tau}^2)} e^{\lambda_y S_y(\boldsymbol{\tau}^1\cdot\boldsymbol{\tau}^2)} e^{\lambda_z S_z(\boldsymbol{\tau}^1\cdot\boldsymbol{\tau}^2)} \\ &= \prod_i \left(A_i \mathbf{1} + B_i(\boldsymbol{\tau}^1\cdot\boldsymbol{\tau}^2) + C_i S_i + D_i S_i(\boldsymbol{\tau}^1\cdot\boldsymbol{\tau}^2)\right). \end{aligned} \tag{4.145}$$

All the operators listed in the equation above can be written as 4x4 matrices.

4.5.2 One pion exchange

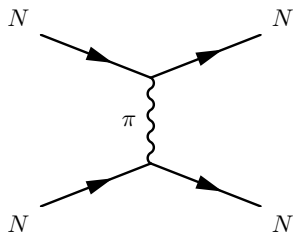

Figure 4.2: One pion exchange diagram.

As mentioned above, the long-range behavior of the nuclear force is due to the one-pion exchange, Fig. 4.2. It arises from tree-level diagrams with four external nucleons and an off-shell pion. The matrix element is given by the usual Feynman rules (and recalling that a derivative acting on a scalar field with incoming momentum q gives $\partial^i\phi = -iq^i\phi$), so we have the matrix element (Savage (1999))

$$\begin{aligned}\mathcal{M} &= \bar{N}\frac{g_A}{\sqrt{2}f_\pi}\sigma^i\tau^a q^i N\frac{i\delta^{ab}}{q^2-m_\pi^2+i\varepsilon}\bar{N}\frac{-g_A}{\sqrt{2}f_\pi}\sigma^j\tau^b q^j N \\ &= i\left(\frac{g_A}{\sqrt{2}f_\pi}\right)^2\bar{N}\sigma^i\tau^a N\bar{N}\sigma^j\tau^a N\frac{q^iq^j}{q^2+m_\pi^2} = -iV_\pi(\boldsymbol{q}), \qquad (4.146)\end{aligned}$$

with $g_A = 1.25$ and $f_\pi = 132$ MeV. This is more commonly written as

$$V_\pi(\boldsymbol{k}) = -\left(\frac{g_A}{\sqrt{2}f_\pi}\right)^2(\boldsymbol{\tau}^1\cdot\boldsymbol{\tau}^2)\frac{(\boldsymbol{\sigma}^1\cdot\boldsymbol{k})(\boldsymbol{\sigma}^2\cdot\boldsymbol{k})}{k^2+m_\pi^2}. \qquad (4.147)$$

The spatial potential is recovered from the momentum space potential $V_\pi(\boldsymbol{k})$ via a Fourier transform,

$$\begin{aligned}V_\pi(\boldsymbol{r}) &= \int\frac{d^3\boldsymbol{k}}{(2\pi)^3}e^{i\boldsymbol{k}\cdot\boldsymbol{r}}V_\pi(\boldsymbol{k}) = -\left(\frac{g_A}{\sqrt{2}f_\pi}\right)^2(\boldsymbol{\tau}^1\cdot\boldsymbol{\tau}^2)\int\frac{d^3\boldsymbol{k}}{(2\pi)^3}e^{i\boldsymbol{k}\cdot\boldsymbol{r}}\frac{(\boldsymbol{\sigma}^1\cdot\boldsymbol{k})(\boldsymbol{\sigma}^2\cdot\boldsymbol{k})}{k^2+m_\pi^2} \\ &= \left(\frac{g_A}{\sqrt{2}f_\pi}\right)^2(\boldsymbol{\tau}^1\cdot\boldsymbol{\tau}^2)(\boldsymbol{\sigma}^1\cdot\nabla)(\boldsymbol{\sigma}^2\cdot\nabla)\int\frac{d^3\boldsymbol{k}}{(2\pi)^3}e^{i\boldsymbol{k}\cdot\boldsymbol{r}}\frac{1}{k^2+m_\pi^2}. \qquad (4.148)\end{aligned}$$

Starting with the integral,

$$\begin{aligned}I(\boldsymbol{r}) &= \int\frac{d^3\boldsymbol{k}}{(2\pi)^3}e^{i\boldsymbol{k}\cdot\boldsymbol{r}}\frac{1}{k^2+m_\pi^2} = \frac{1}{4\pi^2}\int_0^\infty dk k^2\int_{-1}^1 d\cos\theta e^{ikr\cos\theta}\frac{1}{k^2+m_\pi^2} \\ &= \frac{1}{2\pi^2 r}\int_0^\infty dk\sin(kr)\frac{k}{k^2+m_\pi^2} = -\frac{i}{8\pi^2 r}\int_{-\infty}^\infty dk\frac{k}{k^2+m_\pi^2}(e^{ikr}-e^{-iqr}) \\ &= \frac{1}{4\pi r}e^{-m_\pi r}, \qquad (4.149)\end{aligned}$$

where we used Cauchy's residue theorem in the last step. Hence,

$$V_\pi(r) = \frac{1}{4\pi}\left(\frac{g_A}{\sqrt{2}f_\pi}\right)^2(\boldsymbol{\tau}^1\cdot\boldsymbol{\tau}^2)(\boldsymbol{\sigma}^1\cdot\nabla)(\boldsymbol{\sigma}^2\cdot\nabla)\frac{1}{r}e^{-m_\pi r}. \qquad (4.150)$$

Now we have to evaluate the partial derivatives acting on $I(r)$. Let us begin with

$$\begin{aligned}&\partial_i\partial_j\left(\frac{e^{-mr}}{r}\right) = \\ &\qquad e^{-mr}\partial_i\partial_j\left(\frac{1}{r}\right)+\partial_i e^{-mr}\partial_j\left(\frac{1}{r}\right)+\partial_j e^{-mr}\partial_i\left(\frac{1}{r}\right)+\frac{1}{r}\partial_i\partial_j e^{-mr}. \qquad (4.151)\end{aligned}$$

Next, we evaluate the two possible cases. For $i \neq j$,

$$\partial_i \partial_j \left(\frac{e^{-mr}}{r} \right) = e^{-mr} \frac{3\hat{r}^i \hat{r}^j}{r^3} + e^{-mr} 2m \frac{\hat{r}^i \hat{r}^j}{r^2} + e^{-mr} m \frac{\hat{r}^i \hat{r}^j}{r^2} + e^{-mr} m^2 \frac{\hat{r}^i \hat{r}^j}{r}. \quad (4.152)$$

And for $i = j$,

$$\begin{aligned} \partial_i \partial_i \left(\frac{e^{-mr}}{r} \right) &= e^{-mr} \frac{3\hat{r}^i \hat{r}^i}{r^3} - \frac{\delta_{ij}}{r^3} + e^{-mr} 2m \frac{\hat{r}^i \hat{r}^j}{r^2} + e^{-mr} m \frac{\hat{r}^i \hat{r}^j}{r^2} + e^{-mr} m^2 \frac{\hat{r}^i \hat{r}^j}{r} \\ &\quad - \frac{m}{r^2} \delta_{ij}. \end{aligned} \quad (4.153)$$

So far we ignored the singularity at the origin. For $r \to 0$, $e^{-mr} \to 1$. If we integrate around the origin,

$$\begin{aligned} &\int_{\substack{\text{sphere} \\ \text{radius } R \to 0}} d^3 r \; \boldsymbol{\sigma}_1 \cdot \nabla \boldsymbol{\sigma}_2 \cdot \nabla \frac{1}{r} = \int d^3 r \nabla \cdot \left[\boldsymbol{\sigma}_1 \boldsymbol{\sigma}_2 \cdot \nabla \frac{1}{r} \right] = \\ &= \int_{\text{Surface}} dS \; \hat{r} \cdot \boldsymbol{\sigma}_1 \boldsymbol{\sigma}_2 \cdot \hat{r} \left(\frac{-1}{r^2} \right) = - \int d\Omega \; \boldsymbol{\sigma}_1 \cdot \hat{r} \; \boldsymbol{\sigma}_2 \cdot \hat{r} \\ &= - \int d \cos\theta \int d\varphi (\sigma_{1x} \sin\theta \cos\varphi + \sigma_{1y} \sin\theta \sin\varphi + \sigma_{1z} \cos\theta) \times \\ &\quad (\sigma_{2x} \sin\theta \cos\varphi + \sigma_{2y} \sin\theta \sin\varphi + \sigma_{2z} \cos\theta) \\ &= - \int d \cos\theta (\pi \sin^2\theta [\sigma_{1x}\sigma_{2x} + \sigma_{1y}\sigma_{2y}] + 2\pi \sigma_{1z}\sigma_{2z} \cos^2\theta) \\ &= - \frac{4\pi}{3} \boldsymbol{\sigma}^1 \cdot \boldsymbol{\sigma}^2, \end{aligned} \quad (4.154)$$

where we used $\nabla 1/r = -\hat{r}/r^2$. Hence,

$$\begin{aligned} \partial_i \partial_j \left(\frac{e^{-mr}}{r} \right) = \frac{m_\pi^2}{3} \frac{e^{-m_\pi r}}{r} \left[(3\hat{r}^i \hat{r}^j - \delta_{ij}) \left(1 + \frac{3}{m_\pi r} + \frac{3}{(m_\pi r)^2} \right) + \delta_{ij} \right] \\ - \frac{4\pi}{3} \delta_{ij} \delta^3(r). \end{aligned} \quad (4.155)$$

Finally, the result is

$$\begin{aligned} V_\pi(r) = &\frac{m_\pi^2}{12\pi} \left(\frac{g_A}{\sqrt{2} f_\pi} \right)^2 (\boldsymbol{\tau}^1 \cdot \boldsymbol{\tau}^2) \\ &\left(\left[(3\hat{r} \cdot \boldsymbol{\sigma}^1 \hat{r} \cdot \boldsymbol{\sigma}^2 - \boldsymbol{\sigma}^1 \cdot \boldsymbol{\sigma}^2) \left(1 + \frac{3}{m_\pi r} + \frac{3}{(m_\pi r)^2} \right) + \boldsymbol{\sigma}^1 \cdot \boldsymbol{\sigma}^2 \right] \frac{e^{-m_\pi r}}{r} \right. \\ &\left. - \frac{4\pi}{3} \boldsymbol{\sigma}^1 \cdot \boldsymbol{\sigma}^2 \delta^3(r) \right). \end{aligned} \quad (4.156)$$

4.6 Two nucleons

4.6.1 Nucleon model states

To complete our trial wave functions, we need to construct good trial nuclear model states, $|\Phi\rangle$ of Eq. (4.108). We again are guided by previous experience with GFMC and AFDMC calculations. The trial functions there are typically built from operator correlated linear combinations of antisymmetric products of single-particle orbitals. For example, in nuclear matter the trial function is a Jastrow product of pair-wise operator correlations operating on a Slater determinant of orbitals. Here we will begin by assuming that the pion-nucleon correlations and the associated terms in Eq. (4.108) will include the long-range correlations.

Initially, we build our nuclear model state in the same way. However, we include only short-range operator correlations; the remaining terms in Eq. (4.108) will include long-range correlations. For the calculations described here, we need to construct model states for one- and two-nucleon systems. Since a single nucleon only interacts with the pion field, its model state $|\Phi\rangle$ in Eq. (4.108) is a spin-isospin state, i.e. proton up, proton down, neutron up, neutron down, with no spatial dependence.

Two nucleons in our Hamiltonian interact via pion exchange and from the short range smeared-out contact interactions. A reasonably good trial wave function for s-shell nuclei that contains the major correlations can be constructed with a Jastrow operator product multiplying an antisymmetric product of spin-isospin states. The Jastrow factors go to zero exponentially to properly match the separation energy of one nucleon. At short range, the Jastrow factors solve the two-body Schrödinger equation.

Quantum Monte Carlo simulations have been very successful at describing properties of nuclei and other nucleon systems (Carlson *et al.* (2015a)). Usually, in these

simulations, the nucleon-nucleon interactions are modeled by one of two choices of potentials classes. There are phenomenological potentials, such as the AV18 potential (and related AV6') (Wiringa *et al.* (1995)), and, in the past few years, chiral effective field theory interactions have been employed in QMC simulations (Tews *et al.* (2013); Gezerlis *et al.* (2013, 2014); Roggero *et al.* (2014); Lynn *et al.* (2017)). Both approaches include pionic degrees of freedom implicitly. The AV18 potential, for example, includes a charge-dependent Yukawa potential with a short-range cutoff for the one-pion exchange potential (OPEP), and in the intermediate range there are terms that account for two-pion exchange. Chiral effective field theory, similarly, includes pion-exchange terms. Some terms in these interaction potentials are built assuming static nucleons (which is not the case for the momentum-dependent terms, clearly), and the pion contributions are integrated out. The inclusion of pions in QMC simulations allows us to go beyond this approximation.

Chiral effective field theory

For the calculation of two nucleon trial wave functions we chose a chiral potential, at leading order (LO), of the form specified in Gezerlis *et al.* (2014). We do not include any of the OPE terms present in Gezerlis *et al.* (2014), since our formalism already accounts for this piece of the interaction. The pair interaction can be written in the usual operator form

$$\begin{aligned} V(r) &= v_c(r)\mathbf{1} + v_\tau(r)\boldsymbol{\tau}^1\cdot\boldsymbol{\tau}^2 + v_\sigma(r)\boldsymbol{\sigma}^1\cdot\boldsymbol{\sigma}^2 \\ &+ v_{\sigma\tau}(r)(\boldsymbol{\tau}^1\cdot\boldsymbol{\tau}^2)(\boldsymbol{\sigma}^1\cdot\boldsymbol{\sigma}^2) + v_t(r)t_{12} + v_{t\tau}(r)(\boldsymbol{\tau}^1\cdot\boldsymbol{\tau}^2)t_{12}, \end{aligned} \tag{4.157}$$

where t_{12} is the usual tensor operator,

$$t_{12} = 3\boldsymbol{\sigma}^1\cdot\hat{r}_{12}\boldsymbol{\sigma}^2\cdot\hat{r}_{12} - \boldsymbol{\sigma}^1\cdot\boldsymbol{\sigma}^2, \tag{4.158}$$

and the radial functions $v_i(r)$ are fully specified in Gezerlis *et al.* (2014). In this work, we are interested in the contact terms,

$$C_S \delta_{R_0}(r)\mathbf{1},$$
$$C_T \delta_{R_0}(r)\boldsymbol{\sigma}^1 \cdot \boldsymbol{\sigma}^2, \tag{4.159}$$

which are present in $v_c(r)$ and $v_\sigma(r)$, respectively, and we take C_S and C_T to be tunable constants. The δ_{R_0} are smeared delta functions,

$$\delta_{R_0}(r) = \frac{1}{\pi\Gamma(3/4)R_0^3} \exp\left[-(r/R_0)^4\right], \tag{4.160}$$

where Γ is the gamma function, and $R_0 = 1.2$ fm.

AV6'

The AV6' potential is a reprojection of the AV18 potential (Wiringa *et al.* (1995)) that preserves the binding energy of the deuteron, E_d=2.225 MeV. It also has the same form as Eq. (4.157), but with different radial functions.

4.6.2 The deuteron

A first step towards writing the trial wave function of the deuteron in the presence of explicit pions is to write the exact wave function for the deuteron in free space. The deuteron state is a total angular momentum 1 state, $J = 1$. It has even parity, and it has a quadrupole moment so there are both s and d state orbital angular momenta. Since the parity is even, it cannot have odd orbital angular momenta. Historically, the quadrupole moment indicated the presence of the tensor force, to mix s and d states. The tensor force is zero for singlets, so the spin state is $S = 1$. The total wave function has to be antisymmetric, so it must be in an isospin singlet state. In practical terms, this means we can work in the isospin singlet space and just replace

the $\boldsymbol{\tau}^1 \cdot \boldsymbol{\tau}^2$ operator with -3. Later, when we do more complicated nuclei, we will need to deal with the isospin explicitly. The three possible spin states for the two particles are the usual triplet states $|S\ M_S\rangle$,

$$\begin{aligned} |1\ 1\rangle &= |\uparrow\uparrow\rangle, \\ |1\ 0\rangle &= \frac{1}{\sqrt{2}}(|\uparrow\downarrow\rangle + |\downarrow\uparrow\rangle), \\ |1\ -1\rangle &= |\downarrow\downarrow\rangle. \end{aligned} \tag{4.161}$$

We can get a build a $J = 1$ state by:

- coupling an $L = 0$ state to an $S = 1$ state,
- coupling an $L = 1$ or 2 state to an $S = 1$ state.

Parity tells us that the $L = 1$ state is not part of the ground-state. The deuteron has a triply degenerate ground-state for the three M_J values corresponding to $J = 1$. For convenience, let us calculate the $M_J = 1$ state. Whenever coupling two angular momenta $j_1 \neq 0$ and $j_2 = 0$, then the Clebsch-Gordon coefficient is simply $\delta_{J,j_1}\delta_{M_J,m_1}$, thus

$$\langle J = 1,\ M = 1, L = 0,\ S = 1 | L = 0,\ M_L = 0,\ S = 1,\ M_S = 1\rangle = 1. \tag{4.162}$$

For the $L = 2$ states, we need to look at the table corresponding to coupling an angular momentum 2 to 1, and the column where $J = 1$ and $M_J = +1$. The coefficients are the following,

$$\begin{aligned} \langle J = 1, M_J = 1, L = 2, S = 1 | L = 2, M_L = 2, S = 1, M_S = -1\rangle &= \sqrt{\frac{3}{5}}, \\ \langle J = 1, M_J = 1, L = 2, S = 1 | L = 2, M_L = 1, S = 1, M_S = 0\rangle &= -\sqrt{\frac{3}{10}}, \\ \langle J = 1, M_J = 1, L = 2, S = 1 | L = 2, M_L = 0, S = 1, M_S = 1\rangle &= \sqrt{\frac{1}{10}}. \end{aligned} \tag{4.163}$$

We can construct the following $L = 0$ and $L = 2$ states, which have good $J = 1$ and $M_J = 1$,

$$\begin{aligned} |L=0\rangle &\equiv |l=0, m=0, S=1, M_S=1\rangle \\ |L=2\rangle &\equiv \sqrt{\frac{3}{5}}|l=2, m=2, S=1, M_S=-1\rangle \\ &- \sqrt{\frac{3}{10}}|l=2, m=1, S=1, M_S=0\rangle \\ &+ \sqrt{\frac{1}{10}}|l=2, m=0, S=1, M_S=1\rangle, \end{aligned} \tag{4.164}$$

such that the overlap of the angular part with the position eigenbasis gives the usual spherical harmonics, $\langle \hat{r}|lm\rangle = Y_{lm}(\hat{r})$. These states are called the spin spherical harmonics. The deuteron wave function is therefore

$$|\psi\rangle^d = f_0(\boldsymbol{r})|L=0\rangle + f_2(\boldsymbol{r})|L=2\rangle, \tag{4.165}$$

where $f_0(\boldsymbol{r})$ and $f_2(\boldsymbol{r})$ are functions that we need to determine, and $\boldsymbol{r}$ is the position operator. Since all the spin states are spin triplets, the $\boldsymbol{\sigma}_1 \cdot \boldsymbol{\sigma}_2$ operated on these states gives 1. Let us do a brute force calculation of the tensor operator on the spin state $|1\ 1\rangle$,

$$
\begin{aligned}
\sigma_{1x}x\sigma_{2x}x|1\ 1\rangle &= x^2|\downarrow\downarrow\rangle = x^2|1\ -1\rangle \\
\sigma_{1x}x\sigma_{2y}y|1\ 1\rangle &= ixy|\downarrow\downarrow\rangle = ixy|1\ -1\rangle \\
\sigma_{1x}x\sigma_{2z}z|1\ 1\rangle &= xz|\downarrow\uparrow\rangle \\
\sigma_{1y}y\sigma_{2x}x|1\ 1\rangle &= ixy|\downarrow\downarrow\rangle = ixy|1\ -1\rangle \\
\sigma_{1y}y\sigma_{2y}y|1\ 1\rangle &= -y^2|\downarrow\downarrow\rangle = -y^2|1\ -1\rangle \\
\sigma_{1y}y\sigma_{2z}z|1\ 1\rangle &= iyz|\downarrow\uparrow\rangle \\
\sigma_{1z}z\sigma_{2x}x|1\ 1\rangle &= xz|\uparrow\downarrow\rangle \\
\sigma_{1z}z\sigma_{2y}y|1\ 1\rangle &= iyz|\uparrow\downarrow\rangle \\
\sigma_{1z}z\sigma_{2z}z|1\ 1\rangle &= z^2|\uparrow\uparrow\rangle = z^2|1\ 1\rangle, \qquad (4.166)
\end{aligned}
$$

which gives

$$
t_{12}|1\ 1\rangle = \frac{3z^2 - r^2}{r^2}|1\ 1\rangle + \sqrt{2}\frac{3z(x+iy)}{r^2}|1\ 0\rangle + \frac{3(x+iy)^2}{r^2}|1\ -1\rangle, \qquad (4.167)
$$

or

$$
Y_{00}t_{12}(\hat{r})|1\ 1\rangle = \frac{1}{2\sqrt{\pi}}\left(\frac{3z^2 - r^2}{r^2}|1\ 1\rangle + \sqrt{2}\frac{3z(x+iy)}{r^2}|1\ 0\rangle + \frac{3(x+iy)^2}{r^2}|1\ -1\rangle\right). \qquad (4.168)
$$

The spherical harmonics Y_{2m} can be written as

$$
\begin{aligned}
Y_{22}(x,y,z) &= \langle\hat{r}|l=2\ m=2\rangle = \frac{1}{4}\sqrt{\frac{15}{2\pi}}\frac{(x+iy)^2}{r^2}, \\
Y_{21}(x,y,z) &= \langle\hat{r}|l=2\ m=1\rangle = -\frac{1}{2}\sqrt{\frac{15}{2\pi}}\frac{(x+iy)z}{r^2}, \\
Y_{20}(x,y,z) &= \langle\hat{r}|l=2\ m=0\rangle = \frac{1}{4}\sqrt{\frac{5}{\pi}}\frac{(2z^2 - x^2 - y^2)}{r^2}. \qquad (4.169)
\end{aligned}
$$

Therefore, operating with the tensor operator on the $|L=0\rangle$ spin spherical harmonic is just

$$
t_{12}|L=0\rangle = \sqrt{8}|L=2\rangle. \qquad (4.170)
$$

From this identity, notice that the deuteron wave function can be written as

$$|\psi\rangle^d = \left(f_0(\boldsymbol{r}) + \frac{1}{\sqrt{8}} f_2(\boldsymbol{r}) t_{12} \right) |L=0\rangle, \tag{4.171}$$

which is the operator Jastrow form. To complete the analysis, we need to work out what the tensor operator does when it operates on state $|L=2\rangle$. This can be done by brute force, but instead notice that

$$t_{12}|L=2\rangle = t_{12}\left(\frac{1}{\sqrt{8}} t_{12}|L=0\rangle \right) = \frac{t_{12}^2}{\sqrt{8}}|L=0\rangle. \tag{4.172}$$

On the triplet state, $\boldsymbol{\sigma}_1 \cdot \boldsymbol{\sigma}_2$ is 1, so we can write t_{12}^2 on this state as

$$\begin{aligned} t_{12}^2 &= (3\boldsymbol{\sigma}_1 \cdot \hat{r}\boldsymbol{\sigma}_2 \cdot \hat{r} - 1)^2 = 9(\boldsymbol{\sigma}_1 \cdot \hat{r})^2(\boldsymbol{\sigma}_2 \cdot \hat{r})^2 + 1 - 6(\boldsymbol{\sigma}_1 \cdot \hat{r})(\boldsymbol{\sigma}_2 \cdot \hat{r}) \\ &= 8 - 2t_{12}, \end{aligned} \tag{4.173}$$

where we used the identity $(\mathbf{a}\cdot\boldsymbol{\sigma})(\mathbf{b}\cdot\boldsymbol{\sigma}) = (\mathbf{a}\cdot\mathbf{b})\mathbf{1} + i(\mathbf{a}\times\mathbf{b})\cdot\boldsymbol{\sigma}$. Hence, on triplet states, we have

$$t_{12}|L=2\rangle = \frac{1}{\sqrt{8}}(8 - 2t_{12})|L=0\rangle = \sqrt{8}|L=0\rangle - 2|L=2\rangle. \tag{4.174}$$

The deuteron Hamiltonian can be written in terms of the relative coordinates in the usual way as

$$H = -\frac{\hbar^2}{2m_r}\nabla^2 + \tilde{v}_c(r) + \tilde{v}_t(r)t, \tag{4.175}$$

where t is the tensor operator, m_r is the reduced mass, and since $\boldsymbol{\sigma}_1 \cdot \boldsymbol{\sigma}_2 = 1$ and $\boldsymbol{\tau}_1 \cdot \boldsymbol{\tau}_2$ = -3, the potentials in terms of the original v_6 pieces are

$$\begin{aligned} \tilde{v}_c(r) &= v_c(r) + v_\sigma(r) - 3v_\tau(r) - 3v_{\sigma\tau}(r), \\ \tilde{v}_t(r) &= v_t(r) - 3v_{t\tau}(r). \end{aligned} \tag{4.176}$$

Substituting the wave function and H into the Schröedinger equation, and using

$$\nabla^2 = \frac{1}{r}\frac{\partial^2}{\partial r^2}r - \frac{l(l+1)}{r^2}, \tag{4.177}$$

gives the coupled equations for f_0 and f_2. We define

$$\begin{aligned} rf_0(r) &\equiv F_0(r), \\ rf_2(r) &\equiv F_2(r), \end{aligned} \tag{4.178}$$

and the coupled equations are

$$\begin{aligned} -\frac{\hbar^2}{2m_r}F''_0(r) + \tilde{v}_c(r)F_0(r) + \sqrt{8}\tilde{v}_t(r)F_2(r) = EF_0(r), \\ -\frac{\hbar^2}{2m_r}F''_2(r) + \frac{3\hbar^2}{m_r r^2}F_2(r) + (\tilde{v}_c(r) - 2\tilde{v}_t(r))F_2(r) + \sqrt{8}\tilde{v}_t(r)F_0(r) = EF_2(r). \end{aligned} \tag{4.179}$$

These equations can be integrated to give the ground-state wave function of the deuteron.

4.6.3 Two neutrons

The case of two neutrons corresponds to the uncoupled channel $T = 1$, $S = 0$. We start with the state $|0\rangle_n \equiv (|n\uparrow; n\downarrow\rangle - |n\downarrow; n\uparrow\rangle)/\sqrt{2}$, and the wave function is

$$|\psi\rangle^{nn} = f_0^n(r)|0\rangle_n. \tag{4.180}$$

Since $\boldsymbol{\tau}^1 \cdot \boldsymbol{\tau}^2 = 1$ and $\boldsymbol{\sigma}^1 \cdot \boldsymbol{\sigma}^2 = -3$, we have the central potential,

$$\tilde{v}_c^n(r) = v_c(r) + v_\tau(r) - 3v_\sigma(r) - 3v_{\sigma\tau}(r), \tag{4.181}$$

and the equation we need to solve is

$$-\frac{\hbar^2}{2m_r}F''^n_0(r) + \tilde{v}_c^n(r)F_0^n(r) = EF_0^n(r). \tag{4.182}$$

4.6.4 Deuteron and two neutrons with pions

For the short range interaction here, we use

$$H_{NN}^{2N} = \sum_{i=1}^{2} \left[\frac{P_i^2}{2M_P} + M_P + \beta_K P_i^2 + \delta M \right] + C_S \delta_{R_0}(r_{12}) + C_T \delta_{R_0}(r_{12}) \sigma_{12} \qquad (4.183)$$

and we take C_S and C_T to be tunable constants.

The wave function for the deuteron and for two neutrons is Eq. (4.108) using the model state $|\Phi\rangle$ given by $|\psi\rangle^{d,nn}$. When solving the corresponding differential Eqs. (4.179) and (4.182), we only retain the contact contributions of the leading-order local chiral potential of Gezerlis *et al.* (2014). The correlations arising from the one-pion exchange term are dynamically generated when summing over the pion modes.

4.6.5 Two nucleons in a box

Secs. 4.6.2 and 4.6.3 deal with the deuteron and two neutrons in free space. In order to compute the energy of those systems in the box we performed a "numerical experiment" using a well-established phenomenological pairwise interaction. We used a numerically stable version of the Lanczos algorithm (Lanczos (1950)) to solve for the energy of the deuteron and two neutrons in a box using the AV6' potential (Wiringa *et al.* (1995)). Previous numerical solutions are available for two neutrons in a finite volume (Klos *et al.* (2016)), and the differences between our results and those are negligible. The necessary inputs for the algorithm are a nxn Hermitian matrix, in our case the Hamiltonian H with a AV6' interaction, an initial state, and a number of iterations m. The output is a matrix V with orthonormal columns, and a tridiagonal real symmetric matrix $T = V^\dagger A V$ of size mxm. If $m = n$, then V is unitary and $H = VTV^\dagger$. The algorithm can be summarized as

1. Begin with a normalized state, we choose $|v_1\rangle = |\uparrow\uparrow\rangle$

2. Initial step

   (a) $|w_1'\rangle = H|v_1\rangle$

   (b) $\alpha_1 = \langle w_1'|v_1\rangle$

   (c) $|w_1\rangle = |w_1'\rangle - \alpha_1|v_1\rangle$

3. For $j = 2, \cdots, m$

   (a) $\beta_j = \sqrt{\langle w_{j-1}|w_{j-1}\rangle}$

   (b) $|v_j\rangle = |w_{j-1}\rangle/\beta_j$

   (c) $|w_j'\rangle = H|v_j\rangle$

   (d) $\alpha_j = \langle w_j'|v_j\rangle$

   (e) $|w_j\rangle = |w_j'\rangle - \alpha_j|v_j\rangle - \beta_j|v_{j-1}\rangle$

4. V is the matrix with columns $|v_1\rangle, \cdots, |v_m\rangle$, and T is

$$T = \begin{pmatrix} \alpha_1 & \beta_2 & & & & \\ \beta_2 & \alpha_2 & \beta_3 & & & \\ & \beta_3 & \alpha_3 & \ddots & & \\ & & \ddots & \ddots & \beta_{m-1} & \\ & & & \beta_{m-1} & \alpha_{m-1} & \beta_m \\ & & & & \beta_m & \alpha_m \end{pmatrix}. \tag{4.184}$$

The deuteron (or two neutrons) ground-state energy is the lowest eigenvalue of the tridiagonal matrix T. We use fast Fourier transforms to calculate the kinetic energy efficiently, and the cubic group irreducible representation that corresponds to the angular momentum channels in the periodic box.

4.7 Operators

4.7.1 Basis

In our code we chose to represent each particle state by a pair of bits, with the right bit being the spin and the left bit representing the isospin. Spin up (down) corresponds to 0 (1), and a proton (neutron) is represented by 0 (1). For example, a proton with spin up is 0 (00) and a neutron with spin down is 3 (11).

When we are dealing with two particles, the rightmost bit pair represents particle 1, and the two leftmost bits deal with particle 2. For example,

$$\begin{aligned} 3 &= 0011 = \underbrace{00}_{\text{particle 2}}\ \underbrace{11}_{\text{particle 1}} \rightarrow p\uparrow n\downarrow, \\ 4 &= 0100 = \underbrace{01}_{\text{particle 2}}\ \underbrace{00}_{\text{particle 1}} \rightarrow p\downarrow p\uparrow . \end{aligned} \tag{4.185}$$

The generalization to A particles is straightforward, we just add pairs of bits to the left until we have $2A$ bits. There are 4^A possible states, represented by integers in the interval $[0,4^A-1]$.

In order to show more concrete examples, let us present the model states of the deuteron and two neutrons, which correspond to determining the 16 entries of the ϕ array for the two cases. The deuteron corresponds to the isospin singlet, $(|p\ n\rangle - |n\ p\rangle)/\sqrt{2}$. We need to write the states of Eq. (4.161) in the same basis used in the code,

$$\begin{aligned} |\uparrow\uparrow\rangle &\rightarrow |p\uparrow\ n\uparrow\rangle - |n\uparrow\ p\uparrow\rangle \rightarrow \phi(8)=1, \phi(2)=-1, \\ |\downarrow\downarrow\rangle &\rightarrow |p\downarrow\ n\downarrow\rangle - |n\downarrow\ p\downarrow\rangle \rightarrow \phi(13)=1, \phi(7)=-1, \\ |\uparrow\downarrow\rangle &\rightarrow |p\uparrow\ n\downarrow\rangle - |n\uparrow\ p\downarrow\rangle \rightarrow \phi(12)=1, \phi(6)=-1, \\ |\downarrow\uparrow\rangle &\rightarrow |p\downarrow\ n\uparrow\rangle - |n\downarrow\ p\uparrow\rangle \rightarrow \phi(9)=1, \phi(3)=-1. \end{aligned} \tag{4.186}$$

Notice that the entries that do not appear in the equation above (0,1,4,5,10,11,14,15) have either two protons or two neutrons. The two neutrons system is in the $T = 1$, $S = 0$ channel. In our basis this corresponds to the model state $\phi(14) = 1$ and $\phi(11) = -1$.

4.7.2 One nucleon

For one nucleon the operators are implemented as 4x4 matrices.

$$\sigma_x\phi = \left[\begin{array}{cc:cc} 0 & 1 & 0 & 0 \\ 1 & 0 & 0 & 0 \\ \hdashline 0 & 0 & 0 & 1 \\ 0 & 0 & 1 & 0 \end{array}\right] \begin{bmatrix} \phi^{p\uparrow} \\ \phi^{p\downarrow} \\ \phi^{n\uparrow} \\ \phi^{n\downarrow} \end{bmatrix} = \begin{bmatrix} \phi^{p\downarrow} \\ \phi^{p\uparrow} \\ \phi^{n\downarrow} \\ \phi^{n\uparrow} \end{bmatrix} \tag{4.187}$$

$$\sigma_y\phi = \left[\begin{array}{cc:cc} 0 & -i & 0 & 0 \\ i & 0 & 0 & 0 \\ \hdashline 0 & 0 & 0 & -i \\ 0 & 0 & i & 0 \end{array}\right] \begin{bmatrix} \phi^{p\uparrow} \\ \phi^{p\downarrow} \\ \phi^{n\uparrow} \\ \phi^{n\downarrow} \end{bmatrix} = \begin{bmatrix} -i\phi^{p\downarrow} \\ i\phi^{p\uparrow} \\ -i\phi^{n\downarrow} \\ i\phi^{n\uparrow} \end{bmatrix} \tag{4.188}$$

$$\sigma_z\phi = \left[\begin{array}{cc:cc} 1 & 0 & 0 & 0 \\ 0 & -1 & 0 & 0 \\ \hdashline 0 & 0 & 1 & 0 \\ 0 & 0 & 0 & -1 \end{array}\right] \begin{bmatrix} \phi^{p\uparrow} \\ \phi^{p\downarrow} \\ \phi^{n\uparrow} \\ \phi^{n\downarrow} \end{bmatrix} = \begin{bmatrix} \phi^{p\uparrow} \\ -\phi^{p\downarrow} \\ \phi^{n\uparrow} \\ -\phi^{n\downarrow} \end{bmatrix} \tag{4.189}$$

$$\tau_x\phi = \left[\begin{array}{cc:cc} 0 & 0 & 1 & 0 \\ 0 & 0 & 0 & 1 \\ \hdashline 1 & 0 & 0 & 0 \\ 0 & 1 & 0 & 0 \end{array}\right] \begin{bmatrix} \phi^{p\uparrow} \\ \phi^{p\downarrow} \\ \phi^{n\uparrow} \\ \phi^{n\downarrow} \end{bmatrix} = \begin{bmatrix} \phi^{n\uparrow} \\ \phi^{n\downarrow} \\ \phi^{p\uparrow} \\ \phi^{p\downarrow} \end{bmatrix} \tag{4.190}$$

$$\tau_y\phi = \left[\begin{array}{cc:cc} 0 & 0 & -i & 0 \\ 0 & 0 & 0 & -i \\ \hdashline i & 0 & 0 & 0 \\ 0 & i & 0 & 0 \end{array}\right] \begin{bmatrix} \phi^{p\uparrow} \\ \phi^{p\downarrow} \\ \phi^{n\uparrow} \\ \phi^{n\downarrow} \end{bmatrix} = \begin{bmatrix} -i\phi^{n\uparrow} \\ -i\phi^{n\downarrow} \\ i\phi^{p\uparrow} \\ i\phi^{p\downarrow} \end{bmatrix} \tag{4.191}$$

$$\tau_z\phi = \left[\begin{array}{cc:cc} 1 & 0 & 0 & 0 \\ 0 & 1 & 0 & 0 \\ \hdashline 0 & 0 & -1 & 0 \\ 0 & 0 & 0 & -1 \end{array}\right] \begin{bmatrix} \phi^{p\uparrow} \\ \phi^{p\downarrow} \\ \phi^{n\uparrow} \\ \phi^{n\downarrow} \end{bmatrix} = \begin{bmatrix} \phi^{p\uparrow} \\ \phi^{p\downarrow} \\ -\phi^{n\uparrow} \\ -\phi^{n\downarrow} \end{bmatrix} \tag{4.192}$$

4.7.3 Two nucleons

One-body operators

When we have two nucleons a straightforward way is to consider the operators to be 16x16 matrices. For example, a one-body operator such as σ_z acting on particle 1 is

$$\sigma_z^1 = \left[\begin{array}{c:c:c:c} \sigma_z & 0 & 0 & 0 \\ \hdashline 0 & \sigma_z & 0 & 0 \\ \hdashline 0 & 0 & \sigma_z & 0 \\ \hdashline 0 & 0 & 0 & \sigma_z \end{array}\right] \tag{4.193}$$

while the same operator acting on particle 2 is given by

$\sigma_z^2 =$

$$\left[\begin{array}{cccc:cccc:cccc:cccc}
m_{00} & 0 & 0 & 0 & m_{01} & 0 & 0 & 0 & m_{02} & 0 & 0 & 0 & m_{03} & 0 & 0 & 0 \\
0 & m_{00} & 0 & 0 & 0 & m_{01} & 0 & 0 & 0 & m_{02} & 0 & 0 & 0 & m_{03} & 0 & 0 \\
0 & 0 & m_{00} & 0 & 0 & 0 & m_{01} & 0 & 0 & 0 & m_{02} & 0 & 0 & 0 & m_{03} & 0 \\
0 & 0 & 0 & m_{00} & 0 & 0 & 0 & m_{01} & 0 & 0 & 0 & m_{02} & 0 & 0 & 0 & m_{03} \\
\hdashline
m_{10} & 0 & 0 & 0 & m_{11} & 0 & 0 & 0 & m_{12} & 0 & 0 & 0 & m_{13} & 0 & 0 & 0 \\
0 & m_{10} & 0 & 0 & 0 & m_{11} & 0 & 0 & 0 & m_{12} & 0 & 0 & 0 & m_{13} & 0 & 0 \\
0 & 0 & m_{10} & 0 & 0 & 0 & m_{11} & 0 & 0 & 0 & m_{12} & 0 & 0 & 0 & m_{13} & 0 \\
0 & 0 & 0 & m_{10} & 0 & 0 & 0 & m_{11} & 0 & 0 & 0 & m_{12} & 0 & 0 & 0 & m_{13} \\
\hdashline
m_{20} & 0 & 0 & 0 & m_{21} & 0 & 0 & 0 & m_{22} & 0 & 0 & 0 & m_{23} & 0 & 0 & 0 \\
0 & m_{20} & 0 & 0 & 0 & m_{21} & 0 & 0 & 0 & m_{22} & 0 & 0 & 0 & m_{23} & 0 & 0 \\
0 & 0 & m_{20} & 0 & 0 & 0 & m_{21} & 0 & 0 & 0 & m_{22} & 0 & 0 & 0 & m_{23} & 0 \\
0 & 0 & 0 & m_{20} & 0 & 0 & 0 & m_{21} & 0 & 0 & 0 & m_{22} & 0 & 0 & 0 & m_{23} \\
\hdashline
m_{30} & 0 & 0 & 0 & m_{31} & 0 & 0 & 0 & m_{32} & 0 & 0 & 0 & m_{33} & 0 & 0 & 0 \\
0 & m_{30} & 0 & 0 & 0 & m_{31} & 0 & 0 & 0 & m_{32} & 0 & 0 & 0 & m_{33} & 0 & 0 \\
0 & 0 & m_{30} & 0 & 0 & 0 & m_{31} & 0 & 0 & 0 & m_{32} & 0 & 0 & 0 & m_{33} & 0 \\
0 & 0 & 0 & m_{30} & 0 & 0 & 0 & m_{31} & 0 & 0 & 0 & m_{32} & 0 & 0 & 0 & m_{33}
\end{array}\right]$$

where m_{ij} are the entries of the corresponding one particle 4x4 matrix.

In both cases, the matrices are sparse. A more efficient procedure comes from the realization that a one-body operator acting on a given particle can, at most, change that particle's state into a combination of only four states (proton/neutron $\uparrow/\downarrow$). This way the operators can be represented by 4x4 matrices, but we have to select the relevant states to construct the 4x1 array that is operated on, as well as the 4 elements of the 4^Ax1 array with all the amplitudes that will change.

Two-body operators

In general, two-body operators are represented by 16x16 matrices, but there are special cases where a simpler description is sufficient. That is the case of $\boldsymbol{\tau}^1 \cdot \boldsymbol{\tau}^2$, which corresponds to twice the exchange minus the original state,

$$\boldsymbol{\tau}^1 \cdot \boldsymbol{\tau}^2 |t_2\ s_2\ t_1\ s_1\rangle = 2|t_1\ s_2\ t_2\ s_1\rangle - |t_2\ s_2\ t_1\ s_1\rangle, \tag{4.194}$$

where t_i corresponds to the isospin of particle i, and s_i the spin (unchanged).

4.8 Green's function Monte Carlo

When introducing the diffusion Monte Carlo algorithm in Sec. 2.3 we assumed that the only degrees of freedom were the positions of the particles. The Green's function Monte Carlo method used for the nuclear field theory is similar to the DMC algorithm, with the main difference being that it allows spin- and isospin-dependent interactions, and it includes explicit summations over spin and isospin components. Just like DMC, the GFMC method projects out of a trial wave function $|\Psi_T\rangle$ the lowest eigenstate $|\Phi_0\rangle$ of the Hamiltonian H with non-zero overlap with $|\Psi_T\rangle$,

$$|\Phi_0\rangle \propto \lim_{\tau\to\infty} \exp\left[-(H - E_T)\tau\right] |\Psi_T\rangle, \tag{4.195}$$

where E_T controls the normalization. A repeated application of a short-time propagator is used as in the diffusion Monte Carlo method. Inserting a sequence of completeness relations between each short-time propagator, and using the abbreviated notation of Eq. (4.104), where $\mathbf{R}$ stands for all spatial coordinates and $\mathbf{\Pi}$ for all pion coordinates,

$$\langle \mathbf{R}_N S_N \mathbf{\Pi}_N | \Phi_0 \rangle = \sum_{S_0} \cdots \sum_{S_{N-1}} \int d^3\mathbf{R}_0 d^3\mathbf{\Pi}_0 \cdots d^3\mathbf{R}_{N-1} d^3\mathbf{\Pi}_{N-1}$$
$$\left(\prod_{i=0}^{N-1} \langle \mathbf{R}_{i+1} S_{i+1} \mathbf{\Pi}_{i+1} | \exp\left[-(H - E_T)\delta\tau\right] | \mathbf{R}_i S_i \mathbf{\Pi}_i \rangle \right) \langle \mathbf{R}_0 S_0 \mathbf{\Pi}_0 | \Psi_T \rangle, \tag{4.196}$$

where the summations are over the 4^A spin-isospin states of the A-nucleon system. Monte Carlo techniques are used to sample the $\mathbf{R}_i$ and $\mathbf{\Pi}_i$ in the propagation at each imaginary time-step. For a detailed description of the algorithm, the reader is referred to the review of Carlson *et al.* (2015a) and references therein.

For the remainder of this section we write $\mathcal{R}$ as an abbreviation for the $\mathbf{R}S\mathbf{\Pi}$. Since we consider two versions of the Hamiltonian (including and omitting the Weinberg-Tomozawa term, see Sec. 4.3), we need to consider two distinct versions of the propagator, namely:

$$G_{\rm av}(\mathcal{R}', \mathcal{R}) = \langle \mathcal{R}' | \exp\left[-(H - E_T)\delta\tau\right] | \mathcal{R} \rangle \approx \\ \langle \mathcal{R}' | \exp\left[-\delta\tau V_\pi/2\right] \exp\left[-\delta\tau H_{\pi\pi}\right] \exp\left[-\delta\tau T\right] \exp\left[-\delta\tau V_\pi/2\right] \exp\left[\delta\tau E_T\right] | \mathcal{R} \rangle, \tag{4.197}$$

and

$$G(\mathcal{R}', \mathcal{R}) = \langle \mathcal{R}' | \exp\left[-(H - E_T)\delta\tau\right] | \mathcal{R} \rangle \approx \langle \mathcal{R}' | \left(1 - \delta\tau V_{WT}\right) \exp\left[-\delta\tau V_\pi/2\right] \\ \times \exp\left[-\delta\tau H_{\pi\pi}\right] \exp\left[-\delta\tau T\right] \exp\left[-\delta\tau V_\pi/2\right] \exp\left[\delta\tau E_T\right] | \mathcal{R} \rangle. \tag{4.198}$$

4.8.1 Propagators

Kinetic energy

The Euclidean time propagator associated with the non-relativistic kinetic energy of the nucleons T gives rise to a free diffusion process described by the propagator:

$$G_T(\mathbf{R}', \mathbf{R}) = \langle \mathbf{R}' | \exp\left[-T\delta\tau\right] | \mathbf{R} \rangle = \left[\frac{1}{\lambda^3 \pi^{3/2}}\right]^A \exp\left[-\frac{(\mathbf{R} - \mathbf{R}')^2}{\lambda^2}\right], \tag{4.199}$$

with $\lambda = \sqrt{2\hbar^2 \delta\tau / m}$.

Free harmonic oscillator

Each harmonic oscillator of frequency ω in the Hamiltonian also gives rise to a propagator that can be exactly evaluated,

$$G_{\rm HO}(\pi'',\pi') = \left(\frac{\omega}{2\pi\sinh(\omega\delta\tau)}\right)^{1/2} \times \exp\left[-\frac{\omega}{2\sinh(\omega\delta\tau)}\left((\pi''^2+\pi'^2)\cosh(\omega\delta\tau)-2\pi'\pi''\right)\right]. \quad (4.200)$$

The importance sampled version of this Green's function is (Kalos and Schmidt (1997))

$$\tilde{G}_{\rm HO}(\pi'',\pi') = \frac{\psi_0(\pi'')}{\psi_0(\pi')}\exp\left[\frac{\omega\delta\tau}{2}\right]G_{\rm HO}(\pi'',\pi'), \quad (4.201)$$

where ψ_0 is the wave function for the ground-state of the harmonic oscillator, and we have introduced the trial energy of the harmonic oscillator $E_T^{\rm HO} = \omega/2$. Expanding the equation above we have

$$\tilde{G}_{\rm HO}(\pi'',\pi') = \left(\frac{\omega}{\pi(1-e^{-2\omega\delta\tau})}\right)^{1/2}\exp\left[-\frac{\omega(\pi''-e^{-\omega\delta\tau}\pi')^2}{1-e^{-2\omega\delta\tau}}\right], \quad (4.202)$$

which is a Gaussian centered at $e^{-\omega\delta\tau}\pi'$ with variance $(1-e^{-2\omega\delta\tau})/(2\omega)$. Notice that for $\delta\tau\to\infty$ we have $\tilde{G}(\pi'',\pi')\to\psi_0^2(\pi'')$, and for $\delta\tau\to 0$ we recover the free particle propagator. For N free harmonic oscillators, the importance sampled Green's function is just the product of one dimensional Green's functions of the form of Eq. (4.202).

Weinberg-Tomozawa term

The propagator of Eq. (4.198) contains pion derivatives. As a first-order approximation, we act with the pion derivatives present in V_{WT} on the propagator for the harmonic oscillators $\tilde{G}_{\rm HO}$. This procedure omits possible terms rising from the commutators, and is analogous to the one used to implement spin-orbit propagator used in

other quantum Monte Carlo methods for many-nucleon systems (Sarsa *et al.* (2003)). We consider only the linear part of the Weinberg-Tomozawa propagator,

$$(1 - \delta\tau\ V_{WT})\, e^{-\delta\tau H_0}. \tag{4.203}$$

We operate with the derivatives on the free-propagator, and the result is

$$\begin{aligned}
\delta\tau\ V_{WT} = -\frac{i\delta\tau}{2f_\pi^2 L^3}\epsilon_{ijk}\tau_i \sum_{\boldsymbol{q},\boldsymbol{q}'} \Bigg[& \cos(\boldsymbol{q}\cdot\boldsymbol{r})\cos(\boldsymbol{q}'\cdot\boldsymbol{r})\pi^c_{\boldsymbol{q}j}\frac{(-2\omega_{\boldsymbol{q}'})}{1-e^{-2\omega_{\boldsymbol{q}'}\delta\tau}}(\pi^c_{\boldsymbol{q}'k}{}'' - e^{-\omega_{\boldsymbol{q}'}\delta\tau}\pi^c_{\boldsymbol{q}'k}{}') \\
& + \cos(\boldsymbol{q}\cdot\boldsymbol{r})\sin(\boldsymbol{q}'\cdot\boldsymbol{r})\pi^c_{\boldsymbol{q}j}\frac{(-2\omega_{\boldsymbol{q}'})}{1-e^{-2\omega_{\boldsymbol{q}'}\delta\tau}}(\pi^s_{\boldsymbol{q}'k}{}'' - e^{-\omega_{\boldsymbol{q}'}\delta\tau}\pi^s_{\boldsymbol{q}'k}{}') \\
& + \sin(\boldsymbol{q}\cdot\boldsymbol{r})\cos(\boldsymbol{q}'\cdot\boldsymbol{r})\pi^s_{\boldsymbol{q}j}\frac{(-2\omega_{\boldsymbol{q}'})}{1-e^{-2\omega_{\boldsymbol{q}'}\delta\tau}}(\pi^c_{\boldsymbol{q}'k}{}'' - e^{-\omega_{\boldsymbol{q}'}\delta\tau}\pi^c_{\boldsymbol{q}'k}{}') \\
& + \sin(\boldsymbol{q}\cdot\boldsymbol{r})\sin(\boldsymbol{q}'\cdot\boldsymbol{r})\pi^s_{\boldsymbol{q}j}\frac{(-2\omega_{\boldsymbol{q}'})}{1-e^{-2\omega_{\boldsymbol{q}'}\delta\tau}}(\pi^s_{\boldsymbol{q}'k}{}'' - e^{-\omega_{\boldsymbol{q}'}\delta\tau}\pi^s_{\boldsymbol{q}'k}{}') \Bigg].
\end{aligned} \tag{4.204}$$

Pairwise interaction

For the two nucleon systems we need to compute the exponential of Eq. (4.157), which would involve, in principle, the computation of 16x16 matrices. Instead, we linearize the exponential in order to be able to work with only 4x4 operators. We wish to calculate

$$\begin{aligned}
& \exp(-[v_c + v_\sigma \boldsymbol{\sigma}^1\cdot\boldsymbol{\sigma}^2 + v_t t_{12} + v_\tau \boldsymbol{\tau}^1\cdot\boldsymbol{\tau}^2 + v_{\sigma\tau}\boldsymbol{\tau}^1\cdot\boldsymbol{\tau}^2\boldsymbol{\sigma}^1\cdot\boldsymbol{\sigma}^2 + v_{t\tau}t_{12}\boldsymbol{\tau}^1\cdot\boldsymbol{\tau}^2]\delta\tau) \\
= \ & p_c + p_\sigma \boldsymbol{\sigma}^1\cdot\boldsymbol{\sigma}^2 + p_t t_{12} + p_\tau \boldsymbol{\tau}^1\cdot\boldsymbol{\tau}^2 + p_{\sigma\tau}\boldsymbol{\tau}^1\cdot\boldsymbol{\tau}^2\boldsymbol{\sigma}^1\cdot\boldsymbol{\sigma}^2 + p_{t\tau}t_{12}\boldsymbol{\tau}^1\cdot\boldsymbol{\tau}^2.
\end{aligned} \tag{4.205}$$

A simple way to derive the form for the p functions is to work in the eigenbasis of the v_6 operators. If we rotate the coordinates so that the z axis is along $\hat{r}$, then the eigenbasis is trivially found to be the standard singlet and triplet sets in the spins and isospins. The $\boldsymbol{\sigma}^1\cdot\boldsymbol{\sigma}^2$ and $\boldsymbol{\tau}^1\cdot\boldsymbol{\tau}^2$ have eigenvalues 1 in the corresponding triplet states and eigenvalue -3 in the singlet. The tensor has eigenvalue 2 in the $M_S = \pm 1$ triplet spin states, and -4 in the $m = 0$ triplet state, while the tensor has eigenvalue 0

in the singlet. Evaluating Eq. (4.205) in each of the eigenstates gives 6 independent equations. We evaluate them in the order

$$\begin{array}{lllll} \text{state 1} & T=1, & S=1, & |M_S|=1, \\ \text{state 2} & T=1, & S=1, & M_S=0, \\ \text{state 3} & T=0, & S=1, & |M_S|=1, \\ \text{state 4} & T=0, & S=1, & M_S=0, \\ \text{state 5} & T=1, & S=0, & \\ \text{state 6} & T=0, & S=0\,. & \end{array} \tag{4.206}$$

We define

$$\begin{aligned} e_1 &= e^{-(v_c+v_\sigma+2v_t+v_\tau+v_{\sigma\tau}+2v_{t\tau})\delta\tau}, \\ e_2 &= e^{-(v_c+v_\sigma-4v_t+v_\tau+v_{\sigma\tau}-4v_{t\tau})\delta\tau}, \\ e_3 &= e^{-(v_c+v_\sigma+2v_t-3v_\tau-3v_{\sigma\tau}-6v_{t\tau})\delta\tau}, \\ e_4 &= e^{-(v_c+v_\sigma-4v_t-3v_\tau-3v_{\sigma\tau}+12v_{t\tau})\delta\tau}, \\ e_5 &= e^{-(v_c-3v_\sigma+v_\tau-3v_{\sigma\tau})\delta\tau}, \\ e_6 &= e^{-(v_c-3v_\sigma-3v_\tau+9v_{\sigma\tau})\delta\tau}, \end{aligned} \tag{4.207}$$

and we need to solve

$$\begin{aligned} e_1 &= p_c+p_\sigma+2p_t+p_\tau+p_{\sigma\tau}+2p_{t\tau} \\ e_2 &= p_c+p_\sigma-4p_t+p_\tau+p_{\sigma\tau}-4p_{t\tau} \\ e_3 &= p_c+p_\sigma+2p_t-3p_\tau-3p_{\sigma\tau}-6p_{t\tau} \\ e_4 &= p_c+p_\sigma-4p_t-3p_\tau-3p_{\sigma\tau}+12p_{t\tau} \\ e_5 &= p_c-3p_\sigma+p_\tau-3p_{\sigma\tau} \\ e_6 &= p_c-3p_\sigma-3p_\tau+9p_{\sigma\tau}. \end{aligned} \tag{4.208}$$

This is the matrix equation,

$$\begin{pmatrix} e_1 \\ e_2 \\ e_3 \\ e_4 \\ e_5 \\ e_6 \end{pmatrix} = \begin{pmatrix} 1 & 1 & 2 & 1 & 1 & 2 \\ 1 & 1 & -4 & 1 & 1 & -4 \\ 1 & 1 & 2 & -3 & -3 & -6 \\ 1 & 1 & -4 & -3 & -3 & 12 \\ 1 & -3 & 0 & 1 & -3 & 0 \\ 1 & -3 & 0 & -3 & 9 & 0 \end{pmatrix} \begin{pmatrix} p_c \\ p_\sigma \\ p_t \\ p_\tau \\ p_{\sigma\tau} \\ p_{t\tau} \end{pmatrix} . \tag{4.209}$$

The matrix inversion can be done analytically to give

$$\begin{pmatrix} p_c \\ p_\sigma \\ p_t \\ p_\tau \\ p_{\sigma\tau} \\ p_{t\tau} \end{pmatrix} = \frac{1}{48} \begin{pmatrix} 18 & 9 & 6 & 3 & 9 & 3 \\ 6 & 3 & 2 & 1 & -9 & -3 \\ 6 & -6 & 2 & -2 & 0 & 0 \\ 6 & 3 & -6 & -3 & 3 & -3 \\ 2 & 1 & -2 & -1 & -3 & 3 \\ 2 & -2 & -2 & 2 & 0 & 0 \end{pmatrix} \begin{pmatrix} e_1 \\ e_2 \\ e_3 \\ e_4 \\ e_5 \\ e_6 \end{pmatrix} . \tag{4.210}$$

The result is

$$\begin{aligned} p_c &= (6e_1 + 3e_2 + 2e_3 + e_4 + 3e_5 + e_6)/16 \\ p_\sigma &= (6e_1 + 3e_2 + 2e_3 + e_4 - 9e_5 - 3e_6)/48 \\ p_t &= (3e_1 - 3e_2 + e_3 - e_4)/24 \\ p_\tau &= (2e_1 + e_2 - 2e_3 - e_4 + e_5 - e_6)/16 \\ p_{\sigma\tau} &= (2e_1 + e_2 - 2e_3 - e_4 - 3e_5 + 3e_6)/48 \\ p_{t\tau} &= (e_1 - e_2 - e_3 + e_4)/24 \,. \end{aligned} \tag{4.211}$$

4.8.2 Diffusion constant

The effective mass of nucleon can be obtained by looking at its diffusion. First, let us consider the 1D diffusion of (classical) particles that are initially at the origin, $C(x,0) = \delta(x)$. The diffusion equation,

$$\frac{\partial C(x,\tau)}{\partial \tau} = D\frac{\partial^2 C(x,\tau)}{\partial x^2} \tag{4.212}$$

has the normalized solution

$$C(x,\tau) = \frac{1}{\sqrt{4\pi D\tau}} \exp\left[-\frac{x^2}{4D\tau}\right]. \tag{4.213}$$

If we multiply the diffusion equation by x^2 and integrate all over space we have

$$\begin{aligned} \frac{\partial}{\partial \tau}\int_{-\infty}^{+\infty} dx\ x^2 C(x,\tau) &= D\int_{-\infty}^{+\infty} dx\ x^2 \frac{\partial^2 C(x,\tau)}{\partial x^2}, \\ \frac{\partial}{\partial \tau}\langle x^2(\tau)\rangle &= 2D, \\ \langle x^2(\tau)\rangle &= 2D\tau + \text{constant}. \end{aligned} \tag{4.214}$$

Generalizing the result to three dimensions yields $\langle r^2(\tau)\rangle = 6D\tau + \text{constant}$. Thus, the mass of the nucleon m is related to the slope α of the graph $\langle r^2(\tau)\rangle$ vs τ through

$$mc^2 = \frac{3(\hbar c)^2}{\alpha}. \tag{4.215}$$

4.9 Results

All the results are obtained considering a cell in momentum space, in which the sums over the $\boldsymbol{k}$ wave vectors are limited by the spherical cutoff $\omega_c^s = \sqrt{k_c^2 + m_\pi^2}$, where

$$\frac{4\pi k_c^3}{3} = \left(\frac{2\pi}{L}\right)^3 N_{\boldsymbol{k}}, \tag{4.216}$$

$N_{\boldsymbol{k}}$ being the number of $\boldsymbol{k}$ vectors in the unprimed sums. The number of wave vectors, in the primed sums, in each of the first 10 shells is (1,3,6,4,3,12,12,6,15,12,12).

When $\boldsymbol{k}$ has no zero components there are 6 pion coordinates associated with each $\boldsymbol{k}$, corresponding to the sine and cosine components of the three Cartesian isospin coordinates. We set the pion mass to the average of the masses of the neutral and charged pions, $m_\pi = (m_{\pi_0} + 2m_{\pi_\pm})/3 = 138.04$ MeV. For the nucleon physical mass we used $M_P = 938.92$ MeV, the average of the inverses of the proton and neutron masses, $2/M_P = 1/M_{\text{proton}} + 1/M_{\text{neutron}}$.

It is worth noting that for one nucleon there is no node-crossing, because no fermion exchange occurs with only one fermion. For the two nucleon case the node-crossing is also zero. We expect s-shell nuclei to have a mild fermion sign or phase problem, as occurs in potential models. Whenever energies are computed, both the full propagator and the propagator omitting the Weinberg-Tomozawa term are used. For all other estimators we have limited ourselves to the latter case only.

4.9.1 Mass renormalization

Since our choice for the momentum cutoff is not Lorentz invariant, the two mass counter terms appearing in the Hamiltonians, β_K and δM, are not simply related. The kinetic mass counter term coefficient β_K is determined by requiring that the nucleon diffuses with the physical mass $M_P = 938.92$ MeV for long imaginary-times, and δM is set so that the ground state energy of one nucleon is also the physical mass M_P.

In order to determine β_K, let us consider the diffusion of (classical) particles that are initially at the origin, $C(\boldsymbol{r} = 0, \tau = 0) = \delta^{(3)}(\boldsymbol{r})$. The solution for the diffusion equation

$$\frac{\partial C(\boldsymbol{r}, \tau)}{\partial \tau} = \frac{\nabla^2}{2M_K} C(\boldsymbol{r}, \tau) \tag{4.217}$$

is a Gaussian centered at the origin and with variance τ/M_K. Multiplying the diffusion equation by $\boldsymbol{r}^2$ and integrating over $\boldsymbol{r}$, we get for the mean square displacement $\langle r^2(\tau)\rangle = 3\tau/M_K$ and the kinetic mass of the nucleon can be computed from the slope of $\langle r^2(\tau)\rangle$.

In Fig. 4.3 we plot the mean square displacement as a function of the imaginary time for a cutoff of $\omega_c^s \simeq 449$ MeV, and also the curve we would expect from a diffusion given by Eq. (4.199) with the physical mass M_P. A linear fit to the functional form we propose yields masses that differ by ~ 2 MeV at most from the physical mass, for every cutoff we considered. Thus, in our simulations we set the kinetic mass counter term to zero $\beta_K = 0$, in agreement with our nonrelativistic calculation reported in Sec. 4.4.1 which shows this correction is small.

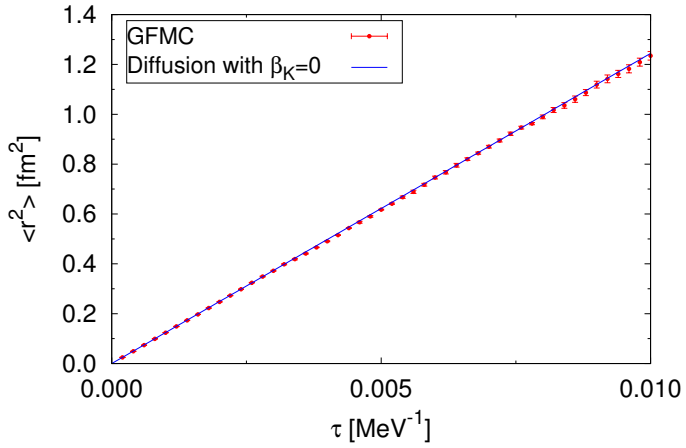

Figure 4.3: Mean square displacement $\langle r^2\rangle$ as a function of the imaginary-time τ. The (blue) curve stands for a particle diffusing according to Eq. (4.199) with the mass set as the physical mass, $M = M_P$. The (red) circles are the GFMC results for $\omega_c^s \simeq 449$ MeV.

The rest mass counter term δM is calculated by requiring that the total energy of a single nucleon interacting with the pion field is equal to the physical mass of the

nucleon. We investigated the full single-nucleon Hamiltonian and the one without the Weinberg-Tomozawa term, using the corresponding propagators. We summarize our results in Fig. 4.4 that are obtained for $L = 10$ fm. The difference between the mass counter terms is $\simeq 4.7$ MeV for the largest cutoff considered, order 0.5% of the total rest mass. Given the simplification in the computational procedures, such small energy difference suggests that it is quite safe to propagate the configurations using the axial-vector coupling only, and to include the Weinberg-Tomozawa contribution to the energy perturbatively.

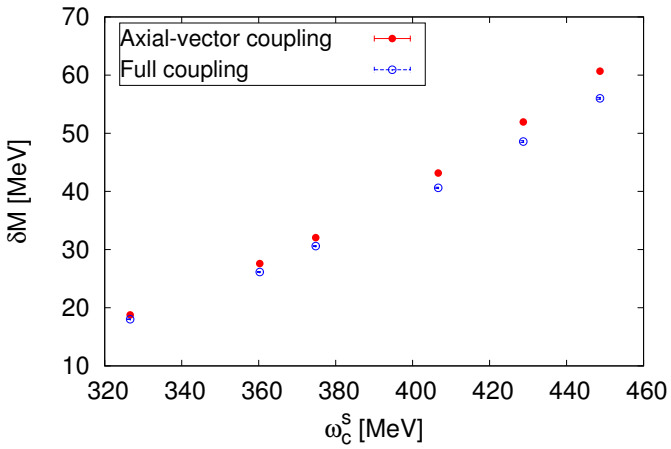

Figure 4.4: Rest mass counter term as a function of the cutoff ω_c^s. The (blue) open circles are the results with the full one-nucleon Hamiltonian Eq. (4.102). The (red) closed circles are the results neglecting the Weinberg-Tomozawa terms H_{WT}.

We also investigated the dependence of our results on the simulation box size. We varied the side of the box $L = 5$, 10, 15 fm, and we compared the results for the rest mass counter term, neglecting the Weinberg-Tomozawa term $H_{\rm WT}^{1N}$. In Fig. 4.5 it is possible to see that the counter term calculated with $L = 5$ fm deviates from the other values for the smallest cutoff considered. However, the difference between the results obtained with $L = 10$ and 15 fm is $\simeq 0.5\%$ of M_P at most. Therefore, in order

to speed up the calculations, we chose $L = 10$ fm for all the calculations presented in the remainder of this work. As an example, for $\omega_c^s \sim 449$ MeV, the box with $L = 15$ fm requires more than 3 times the number of $\boldsymbol{k}$ vectors. In Fig. 4.5 we also show our lowest order nonrelativistic results for the rest mass counter term, described in Sec. 4.4.1. The results differ, at most, by 0.4% of M_P.

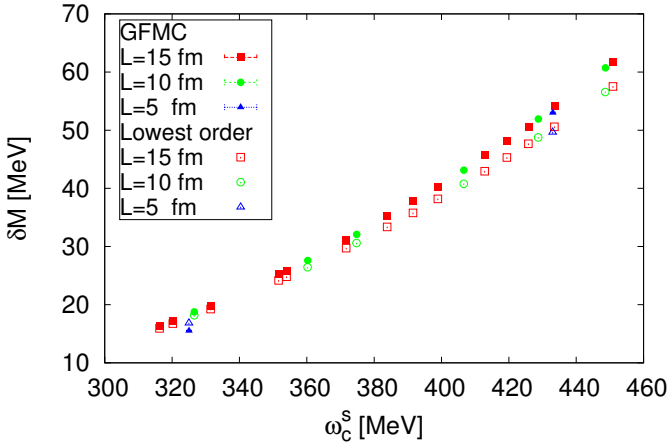

Figure 4.5: The rest mass counter term as a function of the cutoff for $L = 5$, 10, 15 fm, (blue) triangles, (green) circles, (red) squares, respectively. The closed symbols represent GFMC results obtained discarding H_{WT} in Eq. (4.102) in the one-nucleon Hamiltonian. The open symbols stand for the lowest-order nonrelativistic rest mass calculated with Eq. (4.119).

4.9.2 Euclidean time density correlation function

The Euclidean time density correlation function (Fetter and Walecka (2003)), defined as

$$D(\boldsymbol{r}) = \frac{\langle \Psi_T | \rho(\boldsymbol{r}) e^{-(H-E_T)\delta\tau} \rho(0) | \Psi_0 \rangle}{\langle \Psi_T | \Psi_0 \rangle}, \tag{4.218}$$

accounts for the nucleon displacement in between diffusion steps. In Fig. 4.6 we compare our results with the free-particle propagator of Eq. (4.199), where we set $M = M_P$, with those obtained from $D(\boldsymbol{r})$, assuming that the latter is a function of only $r = |\boldsymbol{r}|$, which is true for large enough systems. The fact that in the short-time limit the nucleon is diffusing with a constant related to M_P is consistent with our findings reported in Sec. 4.9.1.

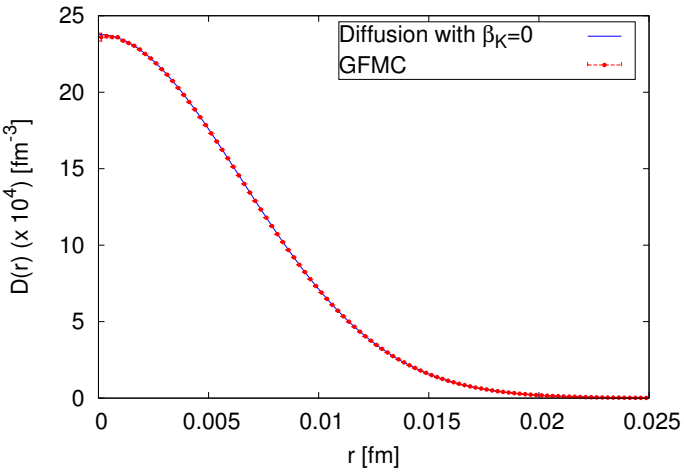

Figure 4.6: Euclidean time density correlation as a function of the displacement for a cutoff $\omega_c^s \simeq 449$ MeV. The red circles correspond to the GFMC results, while the blue curve stands for Eq. (4.199) evaluated at $M = M_P$.

4.9.3 The pion cloud

One of the most interesting properties that can be computed within the formalism presented in this paper are those of the virtual pions surrounding the nucleons. Although this might in principle contain some dynamical information, at present we limit ourselves to analyze static properties.

An interesting quantity to analyze is the ground-state momentum distribution of the pion cloud for the different charged states $n_\alpha(\boldsymbol{k})$. Since we the sum of Eq. (4.54)

are written in such a way that $\boldsymbol{k}$ is included and $-\boldsymbol{k}$ is not, this is best represented by the expectation value of

$$N_{i\boldsymbol{k}} = a^\dagger_{\alpha\boldsymbol{k}} a_{\alpha\boldsymbol{k}} + a^\dagger_{\alpha-\boldsymbol{k}} a_{\alpha-\boldsymbol{k}}, \tag{4.219}$$

with the creation and annihilation operators for a pion in a given charge state are given in Eqs. (4.86–4.87). We computed the momentum distributions and radial densities of the pion cloud using the forward walking procedure described in Appendix B in order to avoid the bias due to the trial wave function. We considered a box with L=10 fm, and the model state $|\Phi\rangle$ of Eq. (4.108) corresponding to a spin-up proton.

In the limit $L \to \infty$, $n_\alpha(\boldsymbol{k})$ should be a function of $k = |\boldsymbol{k}|$ alone. Already for L=10 fm we found minimal differences among the modes with the same k, hence in Fig. 4.7 we show the pion momentum distribution as a function of k, only. The normalization is chosen such that $N_\alpha = L^3 \sum_i n_\alpha(k_i) g_i$, where N_α is the total number of pions of charge α, and g_i is the multiplicity of the i-th shell. An interesting feature is that the distribution of π_+ is approximately twice the one of π_0. This follows from the structure of the axial-vector coupling, which involves

$$\tau_i \pi_i = \frac{1}{2}\tau_+(\pi_x - i\pi_y) + \frac{1}{2}\tau_-(\pi_x + i\pi_y) + \tau_z \pi_0, \tag{4.220}$$

with $\tau_\pm = (\tau_x \pm i\tau_y)$ being the isospin raising and lowering operators, and $\pi_0 = \pi_z$. If we suppose that the cartesian π_i are produced in the same amount, then we expect twice as many π_0 than π_+. Since we are looking at a one proton state, the production of π_- is much smaller compared to that of π^+ and π^0. Conversely, if the baryon is a neutron, we get analogous results with the distributions of π_+ and π_- interchanged. Although increasing the cutoff increases the total pion production, the number of pions at low-momenta appears to be cutoff independent.

The pion densities, whose off-diagonal components are related to the momentum distributions through a Fourier transform, can also be resolved for different charge

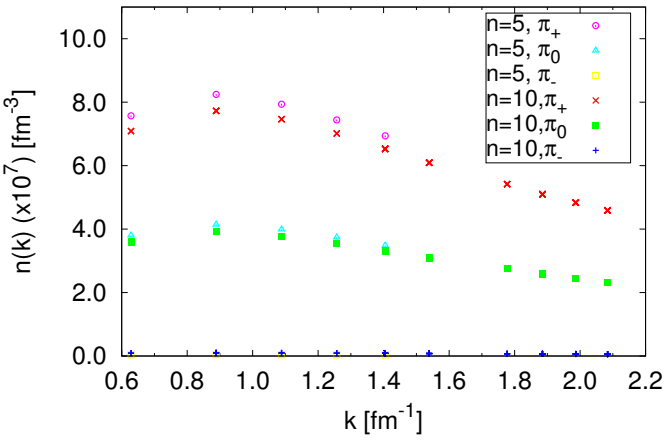

Figure 4.7: Momentum distribution for the different charge states, for systems with different shell numbers, $n = 5$ corresponds to a cutoff $\omega_c^s \simeq 327$ MeV, and $n = 10$ to $\omega_c^s \simeq 449$ MeV. The different symbols correspond to π_+, π_0, and π_- for $n = 5$, (purple) open circles, (cyan) triangles, and (yellow) open squares, respectively; and π_+, π_0, and π_- for $n = 10$, (red) crosses, (green) solid squares, and (blue) pluses, respectively.

states, as in Eq. (4.75). The results for the density are displayed in Fig. (4.8) for a spin-up proton as model state – we did not plot the $n = 5$ density for π_- because it is negligible in the scale of the Figure. In analogy to $n_\alpha(k)$, the production of π_- is heavily suppressed. If the model state is a neutron, we, of course, get identical results with the densities of π_+ and π_- interchanged.

4.9.4 One pion exchange

As mentioned above, the long-range behavior of the nuclear force is due to the one-pion exchange. It arises from tree-level diagrams with four external nucleons and an off-shell pion. At lowest order in perturbation theory, the potential arising from

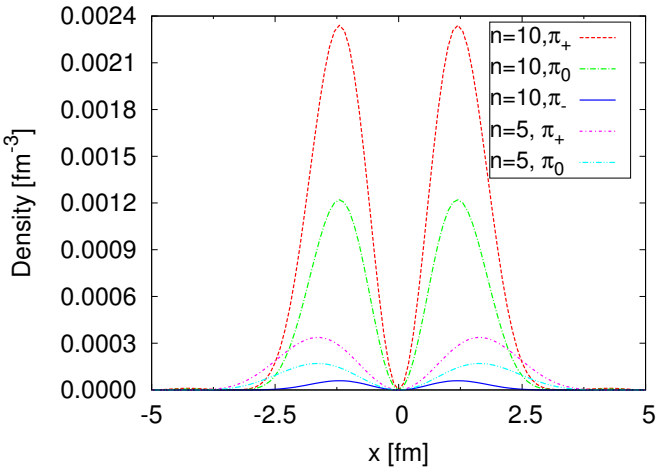

Figure 4.8: Pion density for the different charge states as a function of x coordinate of the box. We plot the density for two systems with different shell numbers, $n = 5$ corresponds to a cutoff $\omega_c^s \simeq 327$ MeV, and $n = 10$ to $\omega_c^s \simeq 449$ MeV. The different curves correspond to π_+, π_0, and π_- for $n = 10$, red long-dash, green dot dash, and solid (blue), respectively; and π_+, π_0 for $n = 5$, purple dot short-dash, and cyan double-dot dash, respectively.

two static nucleons is

$$V_{\rm OPE}(\boldsymbol{q}) = -\left(\frac{g_A}{2f_\pi}\right)^2 \frac{(\boldsymbol{\sigma}_1\cdot\boldsymbol{q})(\boldsymbol{\sigma}_2\cdot\boldsymbol{q})}{q^2+m_\pi^2}\boldsymbol{\tau}_1\cdot\boldsymbol{\tau}_2, \tag{4.221}$$

where $\boldsymbol{q}$ is the transferred momentum. The coordinate-space potential is recovered from $V_{\rm OPE}(\boldsymbol{q})$ via a Fourier transform. In order to make a meaningful comparison we need to compute the one-pion exchange potential keeping into account the geometry and the cutoff of the simulation cell we use.

In Eq. (4.106) the last term on the RHS of the fixed nucleon Hamiltonian contains contributions of the self-energy of the nucleons and the one-pion exchange potential,

in which we are interested. Keeping only terms that involve the coupling between the two nucleons,

$$V_{\rm OPE}(\boldsymbol{r}) = -\frac{1}{L^3}\frac{g_A^2}{2f_\pi^2}\boldsymbol{\tau}_1\cdot\boldsymbol{\tau}_2\sum_{\boldsymbol{k}}{}'(\boldsymbol{\sigma}_1\cdot\boldsymbol{k})(\boldsymbol{\sigma}_2\cdot\boldsymbol{k}) \times\frac{\cos(\boldsymbol{k}\cdot\boldsymbol{r})}{\omega_k^2}, \tag{4.222}$$

which is consistent with Eq. (4.221).

The instantaneous one-pion exchange potential neglects terms where two or more pions are exchanged and the vertices are in different time orders. These commutator terms contribute even for fixed nucleons. However they become unimportant for large nucleon separations. We studied the interaction between two fixed nucleons as a function of the inter-particle distance r in the $T = 1$ and $S = 0$ and $T = 0$ and $S = 1$ channels. We used VMC calculations and checked that they were accurate by performing GFMC calculations at a few separations. Our VMC results, represented by the points in Fig. 4.9, are obtained by subtracting the nucleon self-interaction terms from the ground-state expectation value of $H_{\pi\pi} + H_{AV}$ for two different spherical cutoffs. For comparison, we also show the curves corresponding to the one-pion exchange potential of Eq. (4.222) for the same cutoff employed in the VMC calculations. As expected, the VMC results agree with the one-pion exchange potential at sufficiently large distances, $r \gtrsim 3.0$ fm. The differences at smaller distances are from multiple pion-exchange contributions, which are automatically included in the VMC calculations. This is one of the key features of explicitly including the modes of the pion field, which is absent in conventional nuclear many-body theory approaches, in which multiple pion-exchange potentials have to be explicitly included in the Hamiltonian.

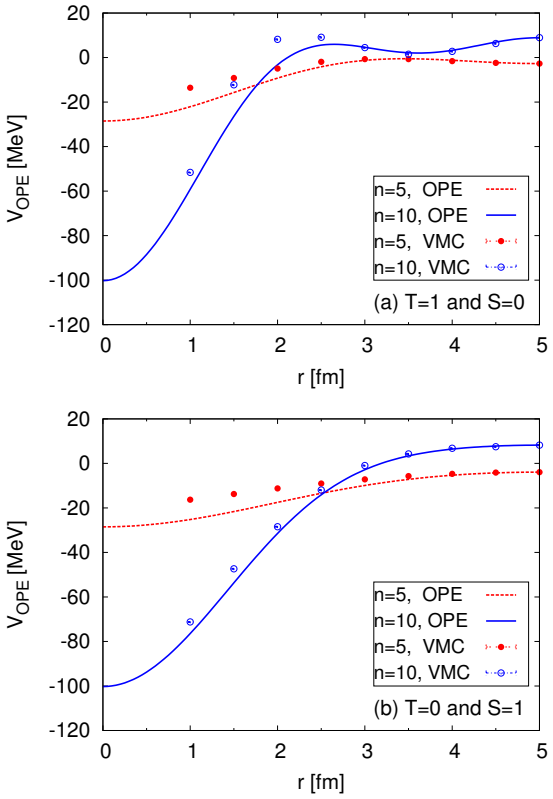

Figure 4.9: One-pion exchange potential for two nucleons a distance r apart along the x-axis in the $T = 1$ and $S = 0$ channel (upper panel) and $T = 0$ and $S = 1$ channel (lower panel). The points (VMC) correspond to our variational results, where the full red circles denote $n = 5$ ($\omega_c^s \simeq 327$ MeV) and open blue circles stand for $n = 10$ ($\omega_c^s \simeq 449$ MeV). The curves (OPE) correspond to the one-pion exchange potential of Eq. (4.222) with the same cutoff as the VMC calculations.

4.9.5 Two nucleons

We need to fix the low-energy constants C_S and C_T associated to the contact terms entering H_{NN}^{2N} of Eq. (4.183). These should be either fitted to experiment or to QCD. Instead of fitting to experiment, we take the expedient step of fitting to results of a potential model that has been fit to experiments. Since our calculations rely on a

periodic box, we fit C_S and C_T to reproduce the ground state results of the Argonne v_6' (AV6P) potential (Wiringa *et al.* (1995)) for the deuteron and two-neutrons in a periodic box. Note that a possible way of direct fit to experiments would involve the Lüscher method (Lüscher (1991)). The energy spectrum of a system of two particles in a box with periodic boundary conditions, for box sizes greater than the interaction range, and for energies below the inelastic threshold, is determined by the scattering phases at these energies. The Lüscher method can be used to compute the energy levels given the scattering phases or, conversely, to calculate the scattering phases if the energy spectrum is known.

As a first step, we developed a numerically stable version of the Lanczos algorithm (Lanczos (1950)) to solve for the energy of the deuteron and two neutrons in a periodic box using the AV6P potential and a plane wave basis. By imposing periodic boundary conditions, the continuum version of the AV6P potential, which has the operator structure of Eq. (4.157), is modified to include periodic images from the surrounding boxes,

$$V_{NN}(\boldsymbol{r}_{12}) \to \sum_{\boldsymbol{n}} V(\boldsymbol{r}_{12} + L\boldsymbol{n}), \tag{4.223}$$

where $\boldsymbol{n} = (n_x, n_y, n_z)$ with n_i integers numbers. The self potential energy term of the periodic images is included. We proved that for $L \geq 10$ fm one image in each direction is sufficient to obtain periodic solutions since the AV6P interaction is at most of one pion exchange range. In panel (a) and (b) of Fig. 4.10 we plot the binding energy of the deuteron and two neutrons, respectively as a function of the box side. For $L < 25$ fm, the deuteron energies are much lower than the value for the system in free space. However, for $L \geq 25$ fm the agreement between finite periodic box results and the continuum is remarkably good.

We then tune C_S and C_T in the GFMC simulations with explicit pions to reproduce the energies of both two nucleon systems. We do not include the Weinberg-Tomozawa

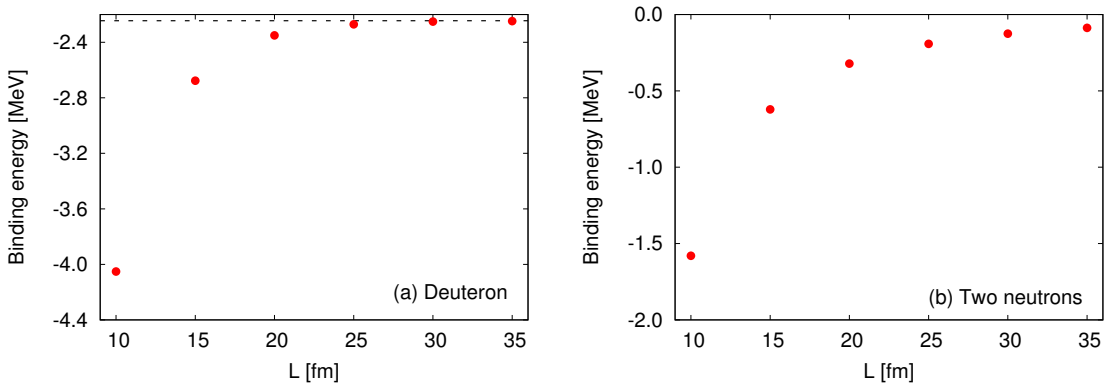

Figure 4.10: Binding energy of the deuteron (a) and two neutrons (b) in a box. The symbols correspond to the energy calculated using the Lanczos algorithm with the AV6' potential. The dashed line corresponds to the binding energy of the deuteron in free space using the AV6' potential.

term, as the one-nucleon results suggest it will provide a small contribution for the momentum cutoffs we employed. Based on the results of Fig. 4.10, we performed the explicit-pion calculations only for $25 \leq L \leq 35$ fm. The pion nucleon axial-vector coupling in our formalism is already periodic, hence only the contact terms of Eq. (4.183) should in principle be modified as in Eq. (4.223). Since those terms are short-ranged compared to the one-pion exchange potential, for $25 \leq L \leq 35$ fm we find that we do not require the potential from the surrounding boxes.

The fitted values of C_S and C_T for different box sizes and cutoffs are reported in Tab. 4.1. We are aware that the cutoffs we used are very low compared to those typically used in other chiral EFT formulations. This choice is by no means due to an intrinsic limitation of the method, but to the extent of the computational effort that we deemed reasonable to obtain these demonstrative results. It is worth mentioning that the chiral potential of Gezerlis *et al.* (2014) at LO gives a deuteron binding energy of $E_d = -2.02$ MeV, which considerably differs from the experimental value

-2.23 MeV. Hence, one of the reasons for the difference between the values of C_S and C_T that we found and the ones reported in Gezerlis *et al.* (2014) for the LO potential can be attributed to this difference in the fitted deuteron energy. Additional reasons for this difference are the finite volume of the box, and the momentum cutoff that we employ. Finally, subleading multiple pion-exchange contributions, fully accounted for in our calculations, appear at NLO in the standard power counting of the chiral interaction.

Table 4.1: Contact parameters for different box sizes, L=25, 30, and 35 fm, as a function of the cutoff ω_c^s. The ω_c^s are given in MeV, while C_S and C_T are in fm^2.

	L= 25 fm			L= 30 fm			L= 35 fm		
n	ω_c^s	C_S	C_T	ω_c^s	C_S	C_T	ω_c^s	C_S	C_T
1	150.06	-3.342	-0.185	146.49	-3.333	-0.197	144.30	-3.331	-0.196
2	160.61	-3.409	-0.140	154.06	-3.372	-0.165	149.98	-3.354	-0.176
3	166.05	-3.444	-0.121	158.02	-3.395	-0.149	152.97	-3.368	-0.165
4	169.68	-3.474	-0.109	160.67	-3.412	-0.137	154.99	-3.379	-0.157
5	181.85	-3.579	-0.085	169.67	-3.466	-0.108	161.88	-3.415	-0.134
6				177.08	-3.512	-0.100	167.61	-3.437	-0.120
7				180.40	-3.521	-0.094	170.19	-3.457	-0.110
8							176.06	-3.485	-0.108
9							180.28	-3.501	-0.101
10							184.20	-3.533	-0.097

Chapter 5

FINAL REMARKS

We have investigated several properties of vortices in 2D Fermi gases over the BEC-BCS crossover region. We dedicated a considerable portion of this work to carefully understand and control size effects in the disk geometry, since it is very convenient for simulating a single vortex. Given that we were interested in the evolution of the properties in the BEC-BCS crossover, determining the crossover region was important to verify that the interaction strengths studied in this work span the crossover.

The vortex excitation energies and the density profiles are quantities that can be compared with experiments, once they become available. Interestingly, the observed density depletion of the vortex core goes from $\approx 30\%$ at the BCS side, $\eta = 1.5$, to an empty core for $\eta \leqslant 0.25$, at the BEC limit. In 3D, Bogoliubov-de Gennes theory has been used to calculate the density suppression at the vortex core throughout the BEC-BCS crossover (Bulgac and Yu (2003); Sensarma *et al.* (2006); Simonucci *et al.* (2013)). Also, determining the probability current was essential to investigate the changes in the vortex core throughout the crossover region.

Similar calculations in 3D could be compared to our findings. A pseudogap phenomena occurring in 2D and 3D Fermi gases can be related in a universal way through a variable that spans the BEC-BCS crossover (Marsiglio *et al.* (2015)). Further studies are necessary to determine if this universality holds for other quantities, such as the density and the probability current density per particle. This would provide a very clean way of comparing 2D and 3D results.

In 3D the interplay between experiments, theory, and simulations led to rapid advances in our comprehension of cold Fermi gases. Hopefully, our results will motivate experiments to increase our understanding of vortices in 2D Fermi gases.

In the second part of this dissertation we describe a promising scheme to explicitly include pion fields in a quantum Monte Carlo calculation of a one- and two-nucleon systems. This approach can be readily extended to larger nuclei, consistently with the limits of application of the underlying GFMC (or AFDMC) techniques. One important remark to be made is that, since pion fields are bosonic, no further contribution to the fermion sign/phase problem is introduced.

The first application to the one-nucleon system is meant to verify the consistency of the method itself. In particular we analyzed finite-size effects, and the extent of the differences due to the choice of the initial Lagrangian. We first studied the renormalization of the nucleon mass with a Hamiltonian in which the coupling between the nucleons and the pion fields is described by an axial-vector interaction. A consistency check against first-order diagrammatic calculation of the self-energy of the nucleon has been successfully carried out. We tried to assess the importance of including the Weinberg-Tomozawa coupling in the interaction. Although this term appears at leading order in the chiral expansion, we showed that its effect in the renormalization of the nucleon mass is much smaller than that of the axial-vector coupling. One interesting possibility opened by our method is the direct study of the pion distribution. In the one-nucleon sector, we analyzed the momentum and density distributions of the pion cloud surrounding the nucleon. Although many details are still missing, this can be thought of as a first step towards the calculation of the single-nucleon electroweak form factors. Standard chiral-EFT calculations fail to describe the proton and nucleon form factors for momentum transfers beyond $Q^2 \sim 0.1$ GeV^2 (Kubis and Meissner (2001)). The inclusion of vector mesons sensibly improve the agreement

with data (Scherer (2010)). Within our explicit-pion QMC framework, we plan to assess whether the resummation of important higher-order contributions can mimic their inclusion.

Turning to the two-body problem, the correct asymptotic behavior of the potential between two static nucleons was verified. As expected, the short/intermediate range part of the potential differs from the OPE expression, due to multiple-pion exchange, automatically included in our formalism. The low-energy constants of the contact terms in the Hamiltonian were determined by fitting exact diagonalization results on the binding energy of the two-body problem (pn and nn) in a finite box. This is a necessary step towards the simulations of light nuclei within the explicit-pion formalism. In this paper we employed a sharp spherical momentum cutoff. The dependence of results on the specific choice of the regularization will be explored in future works.

As previously mentioned, the extension of the calculations to larger systems (and in particular A=3,4 nuclei) is straightforward, aside for the larger computational cost. Work along this direction is currently in progress.

Adhikari, S. K., W. G. Gibson and T. K. Lim, "Effective-range theory in two dimensions", The Journal of Chemical Physics **85**, 10, 5580–5583, URL http://scitation.aip.org/content/aip/journal/jcp/85/10/10.1063/1.451572 (1986).

Anderson, E. R. and J. E. Drut, "Pressure, Compressibility, and Contact of the Two-Dimensional Attractive Fermi Gas", Phys. Rev. Lett. **115**, 115301, URL http://link.aps.org/doi/10.1103/PhysRevLett.115.115301 (2015).

Anderson, J. B., "A random-walk simulation of the Schrodinger equation: H+3", The Journal of Chemical Physics **63**, 4, 1499–1503, URL http://scitation.aip.org/content/aip/journal/jcp/63/4/10.1063/1.431514 (1975).

Barrett, B. R., P. Navratil and J. P. Vary, "Ab initio no core shell model", Prog. Part. Nucl. Phys. **69**, 131–181 (2013).

Berezinsky, V. L., "Destruction of long range order in one-dimensional and two-dimensional systems having a continuous symmetry group. 1. Classical systems", Sov. Phys. JETP **32**, 493–500 (1971).

Bernard, V., M. Lage, U.-G. Meiner and A. Rusetsky, "Resonance properties from the finite-volume energy spectrum", Journal of High Energy Physics **2008**, 08, 024, URL http://stacks.iop.org/1126-6708/2008/i=08/a=024 (2008).

Bertaina, G. and S. Giorgini, "BCS-BEC Crossover in a Two-Dimensional Fermi Gas", Phys. Rev. Lett. **106**, 110403, URL http://link.aps.org/doi/10.1103/PhysRevLett.106.110403 (2011).

Bloch, I., J. Dalibard and W. Zwerger, "Many-body physics with ultracold gases", Rev. Mod. Phys. **80**, 885–964, URL http://link.aps.org/doi/10.1103/RevModPhys.80.885 (2008).

Borasoy, B., E. Epelbaum, H. Krebs, D. Lee and U. G. Meißner, "Lattice simulations for light nuclei: Chiral effective field theory at leading order", The European Physical Journal A **31**, 1, 105–123, URL https://doi.org/10.1140/epja/i2006-10154-1 (2007).

Botelho, S. S. and C. A. R. Sá de Melo, "Vortex-Antivortex Lattice in Ultracold Fermionic Gases", Phys. Rev. Lett. **96**, 040404, URL http://link.aps.org/doi/10.1103/PhysRevLett.96.040404 (2006).

Bouchaud, J.P., Georges, A. and Lhuillier, C., "Pair wave functions for strongly correlated fermions and their determinantal representation", J. Phys. France **49**, 4, 553–559, URL http://dx.doi.org/10.1051/jphys:01988004904055300 (1988).

Bulgac, A. and Y. Yu, "Vortex State in a Strongly Coupled Dilute Atomic Fermionic Superfluid", Phys. Rev. Lett. **91**, 190404, URL http://link.aps.org/doi/10.1103/PhysRevLett.91.190404 (2003).

Carbone, A., A. Cipollone, C. Barbieri, A. Rios and A. Polls, "Self-consistent Green's functions formalism with three-body interactions", Phys. Rev. **C88**, 5, 054326 (2013).

Carlson, J., S.-Y. Chang, V. R. Pandharipande and K. E. Schmidt, "Superfluid Fermi Gases with Large Scattering Length", Phys. Rev. Lett. **91**, 050401, URL http://link.aps.org/doi/10.1103/PhysRevLett.91.050401 (2003).

Carlson, J., S. Gandolfi and A. Gezerlis, *Fifty Years of Nuclear BCS* (World Scientific Publishing Company, 2013).

Carlson, J., S. Gandolfi, F. Pederiva, S. C. Pieper, R. Schiavilla, K. E. Schmidt and R. B. Wiringa, "Quantum Monte Carlo methods for nuclear physics", Rev. Mod. Phys. **87**, 1067–1118, URL https://link.aps.org/doi/10.1103/RevModPhys.87.1067 (2015a).

Carlson, J., S. Gandolfi, F. Pederiva, S. C. Pieper, R. Schiavilla, K. E. Schmidt and R. B. Wiringa, "Quantum Monte Carlo methods for nuclear physics", Rev. Mod. Phys. **87**, 1067 (2015b).

Carlson, J. and K. E. Schmidt, *Monte Carlo Approaches to Effective Field Theories*, pp. 431–439 (Springer US, Boston, MA, 1992), URL https://doi.org/10.1007/978-1-4615-3466-2_29.

Casula, M., C. Attaccalite and S. Sorella, "Correlated geminal wave function for molecules: An efficient resonating valence bond approach", The Journal of Chemical Physics **121**, 15, 7110–7126, URL http://scitation.aip.org/content/aip/journal/jcp/121/15/10.1063/1.1794632 (2004).

Casulleras, J. and J. Boronat, "Unbiased estimators in quantum Monte Carlo methods: Application to liquid ^{4}He", Phys. Rev. B **52**, 3654–3661, URL https://link.aps.org/doi/10.1103/PhysRevB.52.3654 (1995).

Contessi, L., A. Lovato, F. Pederiva, A. Roggero, J. Kirscher and U. van Kolck, "Ground-state properties of 4He and 16O extrapolated from lattice QCD with pionless EFT", Physics Letters B **772**, 839 – 848, URL http://www.sciencedirect.com/science/article/pii/S0370269317306044 (2017).

De Blasio, F. V. and O. Elgarøy, "Microscopic Structure of a Vortex Line in Superfluid Neutron Star Matter", Phys. Rev. Lett. **82**, 1815–1818, URL http://link.aps.org/doi/10.1103/PhysRevLett.82.1815 (1999).

Epelbaum, E., H.-W. Hammer and U.-G. Meissner, "Modern Theory of Nuclear Forces", Rev. Mod. Phys. **81**, 1773–1825 (2009).

Epelbaum, E., H. Krebs, D. Lee and U.-G. Meissner, "Ab initio calculation of the Hoyle state", Phys. Rev. Lett. **106**, 192501 (2011).

Feller, W., *An Introduction to Probability Theory and Its Applications*, no. v. 1 in An introduction to probability theory and its applications (Asia Publishing House, 1957), URL https://books.google.com/books?id=4PEEjwEACAAJ.

Fetter, A. and J. Walecka, *Quantum Theory of Many-Particle Systems*, Dover Books on Physics (Dover Publications, 2003).

Feynman, R. P., "Slow Electrons in a Polar Crystal", Phys. Rev. **97**, 660–665, URL https://link.aps.org/doi/10.1103/PhysRev.97.660 (1955).

Foulkes, W. M. C., L. Mitas, R. J. Needs and G. Rajagopal, "Quantum Monte Carlo simulations of solids", Rev. Mod. Phys. **73**, 33–83, URL http://link.aps.org/doi/10.1103/RevModPhys.73.33 (2001).

Gårdestig, A., K. Kubodera and F. Myhrer, "Comparison of the heavy-fermion and Foldy-Wouthuysen formalisms at third order", Phys. Rev. C **76**, 014005, URL https://link.aps.org/doi/10.1103/PhysRevC.76.014005 (2007).

Galea, A., H. Dawkins, S. Gandolfi and A. Gezerlis, "Diffusion Monte Carlo study of strongly interacting two-dimensional Fermi gases", Phys. Rev. A **93**, 023602, URL http://link.aps.org/doi/10.1103/PhysRevA.93.023602 (2016).

Gandolfi, S., "Quantum Monte Carlo study of strongly interacting Fermi gases", Journal of Physics: Conference Series **529**, 1, 012011, URL http://stacks.iop.org/1742-6596/529/i=1/a=012011 (2014).

Gandolfi, S., A. Y. Illarionov, F. Pederiva, K. E. Schmidt and S. Fantoni, "Equation of state of low-density neutron matter, and the $^1S_0$ pairing gap", Phys. Rev. C **80**, 045802, URL http://link.aps.org/doi/10.1103/PhysRevC.80.045802 (2009).

Gezerlis, A. and J. Carlson, "Strongly-Paired Fermions: Cold Atoms and Neutron Matter", Phys. Rev. C **77**, 032801(R) (2008).

Gezerlis, A. and J. Carlson, "Low-density neutron matter", Phys. Rev. C **81**, 025803, URL http://link.aps.org/doi/10.1103/PhysRevC.81.025803 (2010).

Gezerlis, A., S. Gandolfi, K. E. Schmidt and J. Carlson, "Heavy-Light Fermion Mixtures at Unitarity", Phys. Rev. Lett. **103**, 060403, URL http://link.aps.org/doi/10.1103/PhysRevLett.103.060403 (2009).

Gezerlis, A., I. Tews, E. Epelbaum, M. Freunek, S. Gandolfi, K. Hebeler, A. Nogga and A. Schwenk, "Local chiral effective field theory interactions and quantum Monte Carlo applications", Phys. Rev. C **90**, 054323, URL https://link.aps.org/doi/10.1103/PhysRevC.90.054323 (2014).

Gezerlis, A., I. Tews, E. Epelbaum, S. Gandolfi, K. Hebeler, A. Nogga and A. Schwenk, "Quantum Monte Carlo Calculations with Chiral Effective Field Theory Interactions", Phys. Rev. Lett. **111**, 032501, URL https://link.aps.org/doi/10.1103/PhysRevLett.111.032501 (2013).

Giorgini, S., L. P. Pitaevskii and S. Stringari, "Theory of ultracold atomic Fermi gases", Rev. Mod. Phys. **80**, 1215–1274, URL http://link.aps.org/doi/10.1103/RevModPhys.80.1215 (2008).

Hagen, G., T. Papenbrock, M. Hjorth-Jensen and D. J. Dean, "Coupled-cluster computations of atomic nuclei", Rept. Prog. Phys. **77**, 9, 096302 (2014).

Hergert, H., S. K. Bogner, T. D. Morris, A. Schwenk and K. Tsukiyama, "The In-Medium Similarity Renormalization Group: A Novel Ab Initio Method for Nuclei", Phys. Rept. **621**, 165–222 (2016).

Hjorth-Jensen, M., M. Lombardo and U. van Kolck, *An Advanced Course in Computational Nuclear Physics: Bridging the Scales from Quarks to Neutron Stars*, Lecture Notes in Physics (Springer International Publishing, 2017), URL https://books.google.com/books?id=8l7TDgAAQBAJ.

Kalos, M. H. and K. E. Schmidt, "Model fermion Monte Carlo with correlated pairs. II", Journal of Statistical Physics **89**, 1, 425–443, URL https://doi.org/10.1007/BF02770774 (1997).

Kaplan, D. B., M. J. Savage and M. B. Wise, "Nucleon-nucleon scattering from effective field theory", Nuclear Physics B **478**, 3, 629 – 659, URL http://www.sciencedirect.com/science/article/pii/0550321396003574 (1996).

Khuri, N. N., A. Martin, J.-M. Richard and T. T. Wu, "Low-energy potential scattering in two and three dimensions", Journal of Mathematical Physics **50**, 7, URL http://scitation.aip.org/content/aip/journal/jmp/50/7/10.1063/1.3167803 (2009).

Klos, P., J. E. Lynn, I. Tews, S. Gandolfi, A. Gezerlis, H.-W. Hammer, M. Hoferichter and A. Schwenk, "Quantum Monte Carlo calculations of two neutrons in finite volume", Phys. Rev. C **94**, 054005, URL https://link.aps.org/doi/10.1103/PhysRevC.94.054005 (2016).

König, P.-M., R. Roth and K. R. Mecke, "Morphological Thermodynamics of Fluids: Shape Dependence of Free Energies", Phys. Rev. Lett. **93**, 160601, URL https://link.aps.org/doi/10.1103/PhysRevLett.93.160601 (2004).

Kosterlitz, J. M. and D. J. Thouless, "Long range order and metastability in two dimensional solids and superfluids. (Application of dislocation theory)", J. Phys. C **5**, 11, L124, URL http://stacks.iop.org/0022-3719/5/i=11/a=002 (1972).

Kubis, B. and U.-G. Meissner, "Low-energy analysis of the nucleon electromagnetic form-factors", Nucl. Phys. **A679**, 698–734 (2001).

Lanczos, C., "An iteration method for the solution of the eigenvalue problem of linear differential and integral operators", J. Res. Natl. Bur. Stand. B **45**, 255–282 (1950).

Lee, D., "Lattice simulations for few- and many-body systems", Progress in Particle and Nuclear Physics **63**, 1, 117 – 154, URL http://www.sciencedirect.com/science/article/pii/S014664100800094X (2009).

Leggett, A. J., "A theoretical description of the new phases of liquid ^{3}He", Rev. Mod. Phys. **47**, 331–414, URL https://link.aps.org/doi/10.1103/RevModPhys.47.331 (1975).

Levinsen, J. and M. M. Parish, "Strongly Interacting Two-Dimensional Fermi Gases", in "Annual Review of Cold Atoms and Molecules", chap. Chapter 1, pp. 1–75 (World Scientific, 2015), URL http://www.worldscientific.com/doi/abs/10.1142/9789814667746_0001.

Luo, Z., C. E. Berger and J. E. Drut, "Harmonically trapped fermions in two dimensions: Ground-state energy and contact of SU(2) and SU(4) systems via a nonuniform lattice Monte Carlo method", Phys. Rev. A **93**, 033604, URL https://link.aps.org/doi/10.1103/PhysRevA.93.033604 (2016).

Lüscher, M., "Two-particle states on a torus and their relation to the scattering matrix", Nuclear Physics B **354**, 2, 531 – 578, URL http://www.sciencedirect.com/science/article/pii/0550321391903666 (1991).

Lynn, J. E., I. Tews, J. Carlson, S. Gandolfi, A. Gezerlis, K. E. Schmidt and A. Schwenk, "Quantum Monte Carlo calculations of light nuclei with local chiral two- and three-nucleon interactions", Phys. Rev. C **96**, 054007, URL https://link.aps.org/doi/10.1103/PhysRevC.96.054007 (2017).

Machleidt, R. and D. R. Entem, "Chiral effective field theory and nuclear forces", Phys. Rept. **503**, 1–75 (2011).

Madeira, L., S. Gandolfi and K. E. Schmidt, "Core structure of two-dimensional Fermi gas vortices in the BEC-BCS crossover region", Phys. Rev. A **95**, 053603, URL https://link.aps.org/doi/10.1103/PhysRevA.95.053603 (2017).

Madeira, L., A. Lovato, F. Pederiva and K. E. Schmidt, "Quantum Monte Carlo for dynamical pions and nucleons", arXiv pre-print ArXiv:1803.10725[nucl-th] (2018).

Madeira, L., S. A. Vitiello, S. Gandolfi and K. E. Schmidt, "Vortex line in the unitary Fermi gas", Phys. Rev. A **93**, 043604, URL http://link.aps.org/doi/10.1103/PhysRevA.93.043604 (2016).

Makhalov, V., K. Martiyanov and A. Turlapov, "Ground-State Pressure of Quasi-2D Fermi and Bose Gases", Phys. Rev. Lett. **112**, 045301, URL http://link.aps.org/doi/10.1103/PhysRevLett.112.045301 (2014).

Marsiglio, F., P. Pieri, A. Perali, F. Palestini and G. C. Strinati, "Pairing effects in the normal phase of a two-dimensional Fermi gas", Phys. Rev. B **91**, 054509, URL http://link.aps.org/doi/10.1103/PhysRevB.91.054509 (2015).

Martikainen, J.-P. and P. Törmä, "Quasi-Two-Dimensional Superfluid Fermionic Gases", Phys. Rev. Lett. **95**, 170407, URL http://link.aps.org/doi/10.1103/PhysRevLett.95.170407 (2005).

Martiyanov, K., V. Makhalov and A. Turlapov, "Observation of a Two-Dimensional Fermi Gas of Atoms", Phys. Rev. Lett. **105**, 030404, URL http://link.aps.org/doi/10.1103/PhysRevLett.105.030404 (2010).

Metropolis, N., A. W. Rosenbluth, M. N. Rosenbluth, A. H. Teller and E. Teller, "Equation of State Calculations by Fast Computing Machines", The Journal of Chemical Physics **21**, 6, 1087–1092, URL http://scitation.aip.org/content/aip/journal/jcp/21/6/10.1063/1.1699114 (1953).

Nieves, J. and E. R. Arriola, "Bethe-Salpeter approach for unitarized chiral perturbation theory", Nuclear Physics A **679**, 1, 57 – 117, URL http://www.sciencedirect.com/science/article/pii/S0375947400003213 (2000).

Nogga, A., R. G. E. Timmermans and U. v. Kolck, "Renormalization of one-pion exchange and power counting", Phys. Rev. C **72**, 054006, URL https://link.aps.org/doi/10.1103/PhysRevC.72.054006 (2005).

Orel, A. A., P. Dyke, M. Delehaye, C. J. Vale and H. Hu, "Density distribution of a trapped two-dimensional strongly interacting Fermi gas", New Journal of Physics **13**, 11, 113032, URL http://stacks.iop.org/1367-2630/13/i=11/a=113032 (2011).

Ortiz, G. and D. M. Ceperley, "Core Structure of a Vortex in Superfluid ^{4}He", Phys. Rev. Lett. **75**, 4642–4645, URL http://link.aps.org/doi/10.1103/PhysRevLett.75.4642 (1995).

Petrov, D. S., M. A. Baranov and G. V. Shlyapnikov, "Superfluid transition in quasi-two-dimensional Fermi gases", Phys. Rev. A **67**, 031601, URL http://link.aps.org/doi/10.1103/PhysRevA.67.031601 (2003).

Rammelmüller, L., W. J. Porter and J. E. Drut, "Ground state of the two-dimensional attractive Fermi gas: Essential properties from few to many body", Phys. Rev. A **93**, 033639, URL https://link.aps.org/doi/10.1103/PhysRevA.93.033639 (2016).

Randeria, M., J.-M. Duan and L.-Y. Shieh, "Bound states, Cooper pairing, and Bose condensation in two dimensions", Phys. Rev. Lett. **62**, 981–984, URL http://link.aps.org/doi/10.1103/PhysRevLett.62.981 (1989).

Randeria, M., J.-M. Duan and L.-Y. Shieh, "Superconductivity in a two-dimensional Fermi gas: Evolution from Cooper pairing to Bose condensation", Phys. Rev. B **41**, 327–343, URL http://link.aps.org/doi/10.1103/PhysRevB.41.327 (1990).

Ravenhall, D. G., C. J. Pethick and J. R. Wilson, "Structure of Matter below Nuclear Saturation Density", Phys. Rev. Lett. **50**, 2066–2069, URL http://link.aps.org/doi/10.1103/PhysRevLett.50.2066 (1983).

Robilotta, M. R. and C. Wilkin, "On the pion-deuteron scattering length", Journal of Physics G: Nuclear Physics **4**, 6, L115, URL http://stacks.iop.org/0305-4616/4/i=6/a=002 (1978).

Roggero, A., A. Mukherjee and F. Pederiva, "Quantum Monte Carlo Calculations of Neutron Matter with Nonlocal Chiral Interactions", Phys. Rev. Lett. **112**, 221103, URL https://link.aps.org/doi/10.1103/PhysRevLett.112.221103 (2014).

Sadd, M., G. V. Chester and L. Reatto, "Structure of a Vortex in Superfluid ^4He", Phys. Rev. Lett. **79**, 2490–2493, URL http://link.aps.org/doi/10.1103/PhysRevLett.79.2490 (1997).

Sarsa, A., S. Fantoni, K. E. Schmidt and F. Pederiva, "Neutron matter at zero temperature with an auxiliary field diffusion Monte Carlo method", Phys. Rev. C **68**, 024308, URL https://link.aps.org/doi/10.1103/PhysRevC.68.024308 (2003).

Savage, M., URL http://www.int.washington.edu/users/mjs5/Class_560/lec560_3/node2.html (1999).

Scherer, S., "Chiral Perturbation Theory: Introduction and Recent Results in the One-Nucleon Sector", Prog. Part. Nucl. Phys. **64**, 1–60 (2010).

Schmidt, K. and S. Fantoni, "A quantum Monte Carlo method for nucleon systems", Physics Letters B **446**, 2, 99 – 103, URL http://www.sciencedirect.com/science/article/pii/S0370269398015226 (1999).

Sensarma, R., M. Randeria and T.-L. Ho, "Vortices in Superfluid Fermi Gases through the BEC to BCS Crossover", Phys. Rev. Lett. **96**, 090403, URL http://link.aps.org/doi/10.1103/PhysRevLett.96.090403 (2006).

Shi, H., S. Chiesa and S. Zhang, "Ground-state properties of strongly interacting Fermi gases in two dimensions", Phys. Rev. A **92**, 033603, URL http://link.aps.org/doi/10.1103/PhysRevA.92.033603 (2015).

Simonucci, S., P. Pieri and G. C. Strinati, "Temperature dependence of a vortex in a superfluid Fermi gas", Phys. Rev. B **87**, 214507, URL http://link.aps.org/doi/10.1103/PhysRevB.87.214507 (2013).

Tempere, J., M. Wouters and J. T. Devreese, "Imbalanced Fermi superfluid in a one-dimensional optical potential", Phys. Rev. B **75**, 184526, URL http://link.aps.org/doi/10.1103/PhysRevB.75.184526 (2007).

Tews, I., T. Krüger, K. Hebeler and A. Schwenk, "Neutron Matter at Next-to-Next-to-Next-to-Leading Order in Chiral Effective Field Theory", Phys. Rev. Lett. **110**, 032504, URL https://link.aps.org/doi/10.1103/PhysRevLett.110.032504 (2013).

Toulouse, J. and C. J. Umrigar, "Optimization of quantum Monte Carlo wave functions by energy minimization", The Journal of Chemical Physics **126**, 8, 084102, URL http://dx.doi.org/10.1063/1.2437215 (2007).

Weinberg, S., "Nuclear forces from chiral lagrangians", Physics Letters B **251**, 2, 288 – 292, URL http://www.sciencedirect.com/science/article/pii/0370269390909383 (1990).

Weinberg, S., "Three-body interactions among nucleons and pions", Physics Letters B **295**, 1, 114 – 121, URL http://www.sciencedirect.com/science/article/pii/037026939290099P (1992).

Wiringa, R. B., V. G. J. Stoks and R. Schiavilla, "Accurate nucleon-nucleon potential with charge-independence breaking", Phys. Rev. C **51**, 38–51, URL https://link.aps.org/doi/10.1103/PhysRevC.51.38 (1995).

Yu, Y. and A. Bulgac, "Spatial Structure of a Vortex in Low Density Neutron Matter", Phys. Rev. Lett. **90**, 161101, URL http://link.aps.org/doi/10.1103/PhysRevLett.90.161101 (2003).

Zhang, W., G.-D. Lin and L.-M. Duan, "Berezinskii-Kosterlitz-Thouless transition in a trapped quasi-two-dimensional Fermi gas near a Feshbach resonance", Phys. Rev. A **78**, 043617, URL http://link.aps.org/doi/10.1103/PhysRevA.78.043617 (2008).

Zwierlein, M. W., J. R. Abo-Shaeer, A. Schirotzek, C. H. Schunck and W. Ketterle, "Vortices and superfluidity in a strongly interacting Fermi gas", Nature **435**, 7045, 1047–1051, URL http://dx.doi.org/10.1038/nature03858 (2005).

APPENDIX A

OPTIMIZATION METHODS

Quantum Monte Carlo methods rely on a trial wave function which should mimic as many as possible properties of the true ground-state wave function. The trial wave function is used in three different ways in QMC simulations: as an approximation of the ground-state in VMC calculations, as an importance function when importance sampling is performed in DMC simulations, and also as the nodal surface for the fixed-node approximation. Thus, it is clear that a careful optimization of the wave functions is required to produce accurate results, and also to reduce their variance.

The wave functions presented in this work have many variational parameters, so that a brute-force search for a set of parameters that minimizes the variational energy of the system is not feasible. In the following sections we introduce two methods which can be used to find optimal values for the variational parameters.

A.1 Stochastic reconfiguration

The Stochastic Reconfiguration (SR) method (Casula *et al.* (2004)) allows us to minimize the energy expectation value of a variational wave function containing many variational parameters in an arbitrary functional form. We assume that the wave function Ψ has p variational parameters $\{\alpha_k^0\}_{k=1,\cdots,p}$ and we seek the solution of the linear system,

$$\sum_{k=0}^{p} s_{j,k}\Delta\alpha_k = \langle\Psi|O_k(\Lambda I - H)|\Psi\rangle, \tag{A.1}$$

where the operators O_k are defined on each N particle configuration $x = \{\boldsymbol{r}_1, \cdots, \boldsymbol{r}_N\}$ as the logarithmic derivatives with respect to the parameters α_k,

$$O_k(x) = \frac{\partial}{\partial\alpha_k}\ln\Psi(x) \text{ for } k > 0. \tag{A.2}$$

The operator $O_{k=0}$ is the identity, equal to 1 independent of the configuration. The $(p+1)\times(p+1)$ matrix $s_{k,j}$ is given by

$$s_{j,k} = \frac{\langle\Psi|O_jO_k|\Psi\rangle}{\langle\Psi|\Psi\rangle}, \tag{A.3}$$

and it is calculated at each iteration through standard variational Monte Carlo sampling; the single iteration constitutes a small simulation referred hereafter as bin. After each bin, the wave function parameters are iteratively updated,

$$\alpha_k \to \alpha_k + \frac{\Delta\alpha_k}{\Delta\alpha_0}. \tag{A.4}$$

The method is convergent to an energy minimum for large enough Λ.

SR is similar to a standard steepest descent (SD) calculation, where the expectation value of the energy,

$$E(\alpha_k) = \frac{\langle\Psi|H|\Psi\rangle}{\langle\Psi|\Psi\rangle} \tag{A.5}$$

is optimized by iteratively changing the α_k according to the derivatives of the energy (generalized forces f_k),

$$f_k = -\frac{\partial E}{\partial \alpha_k} = -\frac{\langle\Psi|O_k H + H O_k + (\partial_{\alpha_k} H)|\Psi\rangle}{\langle\Psi|\Psi\rangle} + 2\frac{\langle\Psi|O_k|\Psi\rangle\langle\Psi|H|\Psi\rangle}{\langle\Psi|\Psi\rangle^2}$$
$$\alpha_k \to \alpha_k + \Delta t f_k. \tag{A.6}$$

The small time step Δt can be taken as a suitable fixed value, or it can be determined at each iteration by minimizing the energy expectation value. Notice that we have assumed that the variational parameters may also appear in the Hamiltonian. The variation of the total energy ΔE at each step is negative for small enough Δt,

$$\Delta E = -\Delta t \sum_i f_i^2 + \mathcal{O}(\Delta t^2), \tag{A.7}$$

thus the method certainly converges at the minimum when all the forces vanish.

In the following we will show that similar considerations hold for the SR method. Indeed, by eliminating the equation with $k = 0$ from the linear system (Eq. A.1), the SR iteration can be written in a form similar to SD,

$$\alpha_i \to \alpha_i + \Delta t \sum_k \overline{s}_{i,k}^{-1} f_k, \tag{A.8}$$

where $\overline{s}$ is the reduced $p \times p$ matrix,

$$\overline{s}_{j,k} = s_{j,k} - s_{j,0} s_{0,k} \tag{A.9}$$

and Δt is given by

$$\Delta t = \frac{1}{2\left(\Lambda - \frac{\langle\Psi|H|\Psi\rangle}{\langle\Psi|\Psi\rangle} - \sum_{k>0} \Delta\alpha_k s_{k,0}\right)}. \tag{A.10}$$

Thus the value of Δt changes during the simulation, and it remains small for large enough energy shift Λ. However, the analogy with the SD method shows that an energy minimum is reached when Δt is sufficiently small and constant between iterations. The energy variation for a small change of the parameters is

$$\Delta E = -\Delta t \sum_{i,j} \overline{s}_{i,j}^{-1} f_i f_j. \tag{A.11}$$

The above term is always negative because $\overline{s}$ and $\overline{s}^{-1}$ are positive definite; s being an overlap matrix with all positive eigenvalues.

A condition for the stability of the SR, or SD, is that at each iteration the new parameters α' are close to the old α according to a distance. The most important difference between SR and SD is the definition of this distance. For SD we use the Cartesian metric,

$$\Delta_\alpha = \sum_k |\alpha'_k - \alpha_k|^2. \tag{A.12}$$

Instead the SR uses the physical Hilbert space metric of the wave function Ψ,

$$\Delta_\alpha = \sum_{i,j} \overline{s}_{i,j}(\alpha'_i - \alpha_i)(\alpha'_j - \alpha_j), \tag{A.13}$$

namely the square distance between the two normalized wave functions corresponding to two different sets of parameters $\{\alpha'_k\}$ and $\{\alpha_k\}$. The most convenient change of the variational parameters minimizes the functional $\Delta E + \overline{\Lambda}\Delta_\alpha$, where ΔE is the linear change in the energy $\Delta E = -\sum_i f_i(\alpha'_i - \alpha_i)$; and $\overline{\Lambda}$ is a Lagrange multiplier that allows a stable minimization of Ψ (with small change Δ_α). Finally, the iteration is obtained from Eq. (A.8).

The advantage of SR over SD is that sometimes a small change of the variational parameters correspond to a large change of the wave function, and SD takes into account this effect by using the Hilbert space metric of the wave function Ψ. A weak tolerance criterion $\epsilon \simeq 10^{-3}$ provides a very stable algorithm even when the dimension of the variational space is large.

Instead of setting the constant Λ, we choose to determine Δt by verifying the stability and convergence of the algorithm at fixed Δt. The simulation is stable whenever $1/\Delta t > \Lambda_{cut}$, where Λ_{cut} is strongly dependent on the wave function.

Our aim is to conduct simulations with small bins, so many iterations can be performed. However, in the Monte Carlo framework the forces f_k are determined with some statistical noise, and there is an optimal value for the bin length which guarantees fast convergence and unbiased forces.

A.2 Linear method

A.2.1 Overview

We first introduce the normalized wave function (Toulouse and Umrigar (2007))

$$|\bar{\Psi}(\mathbf{p})\rangle = \frac{|\Psi(\mathbf{p})\rangle}{\sqrt{\langle\Psi(\mathbf{p})|\Psi(\mathbf{p})\rangle}}. \tag{A.14}$$

Then we expand this normalized wave function to first order in the parameters $\mathbf{p}$, around the current parameters $\mathbf{p}^0$,

$$|\bar{\Psi}_{\rm lin}(\mathbf{p})\rangle = |\Psi_0\rangle + \sum_{i=1}^{N} \Delta p_i |\bar{\Psi}_i\rangle, \tag{A.15}$$

where the wave function at $\mathbf{p} = \mathbf{p}^0$ is simply $|\bar{\Psi}(\mathbf{p}^0)\rangle = |\bar{\Psi}_0\rangle = |\Psi_0\rangle$ (chosen to be normalized to 1), and for $i \geqslant 1$, $|\bar{\Psi}_i\rangle$ are the derivatives of $|\bar{\Psi}(\mathbf{p})\rangle$ that are orthogonal to $|\Psi_0\rangle$,

$$|\bar{\Psi}_i\rangle = \left.\frac{\partial|\bar{\Psi}(\mathbf{p})\rangle}{\partial p_i}\right|_{\mathbf{p}=\mathbf{p}^0} = |\Psi_i\rangle - S_{0i}|\Psi_0\rangle. \tag{A.16}$$

In order for $|\bar{\Psi}_i\rangle$ to be orthogonal to $|\Psi_0\rangle$, we must have $S_{0i} = \langle\Psi_0|\Psi_i\rangle$:

$$\langle\Psi_0|\bar{\Psi}_i\rangle = \langle\Psi_0|\Psi_i\rangle - S_{0i}\langle\Psi_0|\Psi_0\rangle = \langle\Psi_0|\Psi_i\rangle - S_{0i} = 0. \tag{A.17}$$

We want to minimize the energy, up to linear order, with respect to the parameters $\mathbf{p}$,

$$E_{\text{lin}} = \min_{\mathbf{p}} E_{\text{lin}}(\mathbf{p}), \tag{A.18}$$

where

$$E_{\text{lin}}(\mathbf{p}) = \frac{\langle\bar{\Psi}_{\text{lin}}(\mathbf{p})|H|\bar{\Psi}_{\text{lin}}(\mathbf{p})\rangle}{\langle\bar{\Psi}_{\text{lin}}(\mathbf{p})|\bar{\Psi}_{\text{lin}}(\mathbf{p})\rangle}. \tag{A.19}$$

This leads to the stationary condition of the associated Lagrange function,

$$\nabla_{\mathbf{p}}\left[\langle\bar{\Psi}_{\text{lin}}(\mathbf{p})|H|\bar{\Psi}_{\text{lin}}(\mathbf{p})\rangle - E_{\text{lin}}\langle\bar{\Psi}_{\text{lin}}(\mathbf{p})|\bar{\Psi}_{\text{lin}}(\mathbf{p})\rangle\right] = 0, \tag{A.20}$$

where E_{lin} acts as a Lagrange multiplier for the normalization condition. Eq. (A.20) leads to the generalized eigenvalue equation:

$$\bar{\mathbf{H}} \cdot \Delta\mathbf{p} = E_{\text{lin}}\bar{\mathbf{S}} \cdot \Delta\mathbf{p}, \tag{A.21}$$

where $\bar{\mathbf{H}}$ is the matrix of the Hamiltonian H in the $(N+1)$-dimensional basis of the current normalized wave function and its derivatives $\left\{|\bar{\Psi}_0\rangle, |\bar{\Psi}_1\rangle, \ldots, |\bar{\Psi}_N\rangle\right\}$, with elements $\bar{H}_{ij} = \langle\bar{\Psi}_i|H|\bar{\Psi}_j\rangle$; $\bar{\mathbf{S}}$ is the overlap matrix of this $(N+1)$-dimensional basis, with elements $\bar{S}_{ij} = \langle\bar{\Psi}_i|\bar{\Psi}_j\rangle$ (note that, because of the orthogonality of the derivatives with respect to $|\Psi_0\rangle$, $\bar{S}_{00} = 1$ and $\bar{S}_{i0} = \bar{S}_{0i} = 0$, for $i \geqslant 1$); $\Delta\mathbf{p}$ is the $(N+1)$-dimensional vector of parameter variations with $\Delta p_0 = 1$.

The linear method consists of solving the generalized eigenvalue equation of Eq. (A.21) for the lowest (physically reasonable) eigenvalue, and associated eigenvector $\Delta\bar{\mathbf{p}}$.

A.2.2 Overlap and Hamiltonian matrices

The elements of the symmetric overlap matrix $\bar{\mathbf{S}}$ are

$$\bar{S}_{00} = 1, \tag{A.22}$$

and, for $i, j > 0$,

$$\bar{S}_{i0} = \bar{S}_{0j} = 0, \tag{A.23}$$

and

$$\bar{S}_{ij} = \left\langle \frac{\Psi_i(\mathbf{R})}{\Psi_0(\mathbf{R})}\frac{\Psi_j(\mathbf{R})}{\Psi_0(\mathbf{R})} \right\rangle - \left\langle \frac{\Psi_i(\mathbf{R})}{\Psi_0(\mathbf{R})} \right\rangle \left\langle \frac{\Psi_j(\mathbf{R})}{\Psi_0(\mathbf{R})} \right\rangle. \tag{A.24}$$

The elements of the Hamiltonian matrix $\bar{\mathbf{H}}$ are

$$\bar{H}_{00} = \langle E_L(\mathbf{R}) \rangle, \tag{A.25}$$

and, for $i, j > 0$,

$$\bar{H}_{i0} = \left\langle \frac{\Psi_i(\mathbf{R})}{\Psi_0(\mathbf{R})} E_L(\mathbf{R}) \right\rangle - \left\langle \frac{\Psi_i(\mathbf{R})}{\Psi_0(\mathbf{R})} \right\rangle \langle E_L(\mathbf{R}) \rangle, \tag{A.26}$$

$$\bar{H}_{0j} = \left\langle \frac{\Psi_j(\mathbf{R})}{\Psi_0(\mathbf{R})} E_L(\mathbf{R}) \right\rangle - \left\langle \frac{\Psi_j(\mathbf{R})}{\Psi_0(\mathbf{R})} \right\rangle \langle E_L(\mathbf{R}) \rangle + \langle E_{L,j}(\mathbf{R}) \rangle, \tag{A.27}$$

and

$$\begin{aligned} \bar{H}_{ij} = & \left\langle \frac{\Psi_i(\mathbf{R})}{\Psi_0(\mathbf{R})} \frac{\Psi_j(\mathbf{R})}{\Psi_0(\mathbf{R})} E_L(\mathbf{R}) \right\rangle - \left\langle \frac{\Psi_i(\mathbf{R})}{\Psi_0(\mathbf{R})} \right\rangle \left\langle \frac{\Psi_j(\mathbf{R})}{\Psi_0(\mathbf{R})} E_L(\mathbf{R}) \right\rangle \\ & - \left\langle \frac{\Psi_j(\mathbf{R})}{\Psi_0(\mathbf{R})} \right\rangle \left\langle \frac{\Psi_i(\mathbf{R})}{\Psi_0(\mathbf{R})} E_L(\mathbf{R}) \right\rangle + \left\langle \frac{\Psi_i(\mathbf{R})}{\Psi_0(\mathbf{R})} \right\rangle \left\langle \frac{\Psi_j(\mathbf{R})}{\Psi_0(\mathbf{R})} \right\rangle \langle E_L(\mathbf{R}) \rangle \\ & + \left\langle \frac{\Psi_i(\mathbf{R})}{\Psi_0(\mathbf{R})} E_{L,j}(\mathbf{R}) \right\rangle - \left\langle \frac{\Psi_i(\mathbf{R})}{\Psi_0(\mathbf{R})} \right\rangle \langle E_{L,j}(\mathbf{R}) \rangle. \end{aligned} \tag{A.28}$$

A.2.3 Stabilization

We stabilize the linear method by adding a positive constant, $a_{\text{diag}} \geqslant 0$, to the diagonal of $\bar{\mathbf{H}}$ except for the first element,

$$\bar{H}_{ij} \to \bar{H}_{ij} + a_{\text{diag}} \delta_{ij} (1 - \delta_{i0}). \tag{A.29}$$

Also, there is an arbitrariness in the previously described procedure. We have found the parameter variations $\Delta\bar{\mathbf{p}}$ from the expansion of the wave function $|\bar{\Psi}(\mathbf{p})\rangle$ of Eq. (A.14), but another choice of normalization would lead to different parameter variations. Consider a differently normalized wave function

$$|\bar{\bar{\Psi}}(\mathbf{p})\rangle = N(\mathbf{p}) |\bar{\Psi}(\mathbf{p})\rangle, \tag{A.30}$$

with $N(\mathbf{p}^0) = 1$, which leaves the normalization at $\mathbf{p} = \mathbf{p}^0$ unchanged ($|\bar{\bar{\Psi}}(\mathbf{p}^0)\rangle = |\Psi_0\rangle$). The derivatives are

$$|\bar{\bar{\Psi}}_i\rangle = \left. \frac{\partial |\bar{\bar{\Psi}}(\mathbf{p})\rangle}{\partial p_i} \right|_{\mathbf{p}=\mathbf{p}^0} = |\bar{\Psi}_i\rangle + N_i |\Psi_0\rangle, \tag{A.31}$$

where

$$N_i = \left. \frac{\partial N(\mathbf{p})}{\partial p_i} \right|_{\mathbf{p}=\mathbf{p}^0}, \tag{A.32}$$

i.e., their projections onto the current wave function depend on the normalization. The first-order expansion of this new wave function is

$$|\bar{\bar{\Psi}}_{\rm lin}(\mathbf{p})\rangle = |\Psi_0\rangle + \sum_{i=1}^{N} \Delta p_i |\bar{\bar{\Psi}}_i\rangle, \tag{A.33}$$

which leads to different optimal parameter variations $\Delta\bar{\bar{\mathbf{p}}}$. The two wave functions, $|\bar{\Psi}_{\rm lin}(\mathbf{p})\rangle$ and $|\bar{\bar{\Psi}}_{\rm lin}(\mathbf{p})\rangle$, lie on the same variational space. Therefore, they must be proportional after minimization of the energy, which implies that $\Delta\bar{\mathbf{p}}$ and $\Delta\bar{\bar{\mathbf{p}}}$ are related by a uniform rescaling,

$$\Delta\bar{\bar{\mathbf{p}}} = \frac{\Delta\bar{\mathbf{p}}}{1 - \sum_{i=1}^{N} N_i \Delta\bar{p}_i}. \tag{A.34}$$

An arbitrary choice of normalization does not necessarily give good parameter variations. A good one is to choose each derivative $|\bar{\bar{\Psi}}_i\rangle$ orthogonal to a linear combination of $|\Psi_0\rangle$ and $|\bar{\Psi}_{\rm lin}\rangle$, that is

$$\left\langle \xi\Psi_0 + (1-\xi)\frac{\bar{\Psi}_{\rm lin}}{||\bar{\Psi}_{\rm lin}||} \right\rangle = 0, \tag{A.35}$$

where ξ is a constant between 0 and 1. Hence

$$N_i = -\frac{(1-\xi)\sum_j^{\rm nonlin} \Delta\bar{p}_j \bar{S}_{ij}}{(1-\xi) + \xi\sqrt{1 + \sum_{j,k}^{\rm nonlin} \Delta\bar{p}_j \Delta\bar{p}_k \bar{S}_{jk}}}. \tag{A.36}$$

We verified that the method is stable for $\xi = 1/2$.

A.2.4 Heuristic procedure

The constant $a_{\rm diag}$ introduced in Eq. (A.29) heavily influences the behavior of the algorithm. For large values of $a_{\rm diag}$, the method becomes equivalent to the steepest descent, and for small values of $a_{\rm diag}$, the algorithm becomes unstable. We adopt a heuristic procedure described in Contessi *et al.* (2017) which has proven to be very robust. For a given value of $a_{\rm diag}$ we solve Eq. (A.21). If the linear variation of the wave function is small,

$$\frac{|\bar{\Psi}_T^{\rm lin}(\mathbf{p})|^2}{|\bar{\Psi}_T(\mathbf{p}^0)|^2} = 1 + \sum_{i,j=1}^{N} \bar{S}_{ij} \Delta p_i \Delta p_j \leqslant \delta, \tag{A.37}$$

then a short correlated run is performed in which the energy expectation value

$$E(\mathbf{p}) \equiv \frac{\langle\bar{\Psi}_T(\mathbf{p})|H|\bar{\Psi}_T(\mathbf{p})\rangle}{\langle\bar{\Psi}_T(\mathbf{p})|\bar{\Psi}_T(\mathbf{p})\rangle} \tag{A.38}$$

is estimated along with the full variation of the wave function for a set of possible values of a_{diag} (≈ 100 values). The optimal a_{diag} is chosen such it minimizes $E(\mathbf{p})$ with the constraint:

$$\frac{|\bar{\Psi}_T(\bar{\mathbf{p}})|^2}{|\bar{\Psi}_T(\mathbf{p}^0)|^2} \leqslant \delta. \tag{A.39}$$

We verified that $\delta = 0.2$ guarantees a fast and stable convergence.

APPENDIX B

FORWARD WALKING

The DMC algorithm solves Eq. (2.21) stochastically and, after an iterative process, the asymptotic solution is obtained $\Psi(\mathbf{R}, t \to \infty) = \Phi_0(\mathbf{R})$. The direct calculation of an operator $S(\mathbf{R})$ from $\Phi_0(\mathbf{R})$ corresponds to the mixed estimator

$$\langle S(\mathbf{R})\rangle_m = \frac{\int d\mathbf{R}\Psi_T(\mathbf{R})S(\mathbf{R})\Phi_0(\mathbf{R})}{\int d\mathbf{R}\Psi_T(\mathbf{R})\Phi_0(\mathbf{R})}, \tag{B.1}$$

which is exact only when S commutes with the Hamiltonian H (so that $\Phi_0(\mathbf{R})$ is an eigenfunction of S).

There are several methods to compute expectation values of quantities that do not commute with H, and one of them is the extrapolation method. In this method, the "pure" (exact) estimator,

$$\langle S(\mathbf{R})\rangle_p = \frac{\int d\mathbf{R}\Phi_0(\mathbf{R})S(\mathbf{R})\Phi_0(\mathbf{R})}{\int d\mathbf{R}\Phi_0(\mathbf{R})\Phi_0(\mathbf{R})}, \tag{B.2}$$

is approximated by

$$\langle S(\mathbf{R})\rangle_e = 2\langle S(\mathbf{R})\rangle_m - \langle S(\mathbf{R})\rangle_v, \tag{B.3}$$

where

$$\langle S(\mathbf{R})\rangle_v = \frac{\int d\mathbf{R}\Psi_T(\mathbf{R})S(\mathbf{R})\Psi_T(\mathbf{R})}{\int d\mathbf{R}\Psi_T(\mathbf{R})\Psi_T(\mathbf{R})} \tag{B.4}$$

is the variational estimator of S. The accuracy of the extrapolation method relies completely on the trial wave function. Moreover, even in the case of accurate trial wave functions, the bias of the extrapolated estimator is difficult to be calculated. For these reasons several algorithms that overcome these restrictions have been proposed. Here we describe a method called forward walking, which is discussed in detail in Casulleras and Boronat (1995).

The pure estimator of Eq. (B.2) can be rewritten as

$$\langle S(\mathbf{R})\rangle_p = \frac{\int d\mathbf{R}\Phi_0(\mathbf{R})S(\mathbf{R})\frac{\Phi_0(\mathbf{R})}{\Psi_T(\mathbf{R})}\Psi_T(\mathbf{R})}{\int d\mathbf{R}\Phi_0(\mathbf{R})\frac{\Phi_0(\mathbf{R})}{\Psi_T(\mathbf{R})}\Psi_T(\mathbf{R})}. \tag{B.5}$$

The quantity $\Phi_0(\mathbf{R})/\Psi_T(\mathbf{R})$ is related to the asymptotic offspring of the $\mathbf{R}$ walker (Casulleras and Boronat (1995)). If each walker $\mathbf{R}_i$ is assigned a weight $W(\mathbf{R}_i)$, proportional to its number of descendants, then Eq. (B.5) becomes

$$\langle S(\mathbf{R})\rangle_p = \frac{\sum_i S(\mathbf{R}_i)W(\mathbf{R}_i)}{\sum_i W(\mathbf{R}_i)}, \tag{B.6}$$

where the summations run over all walkers and all times in the asymptotic regime. In order to evaluate Eq. (B.6), an algorithm that calculates $S(\mathbf{R}_i)$ and weights proportional to its future progeny must be introduced.

The algorithm we implemented, which is described in Casulleras and Boronat (1995), is the following. The set of walkers $\{\mathbf{R}_i\}$ and the values that the operator S takes on them $\{S_i\}$ evolve after one time step according to

$$\begin{aligned} \{\mathbf{R}_i\} &\rightarrow \{\mathbf{R}'_i\}, \\ \{S_i\} &\rightarrow \{S'_i\}, \end{aligned} \tag{B.7}$$

while the number of walkers changes from N to N'. In order to sample the pure estimator, an auxiliary variable $\{P_i\}$ is introduced for each walker, with an evolution law

$$\{P_i\} \rightarrow \{P'_i\} = \{p(\mathbf{R}'_i) \times S'_i\} + \left\{ \frac{p(\mathbf{R}'_i)}{p(\mathbf{R}_i)} \times P_i^t \right\}, \tag{B.8}$$

where p is the weight associated with the branching factor, Eq. (2.40), and $\{P_i^t\}$ is the old set $\{P_i\}$ "transported" to the new set. The values of $\{P_i\}$ are initialized to zero at the beginning of the run. After M addition steps, we get the set $\{P_i\}$ corresponding to N_f walkers. The pure estimator is given by

$$\langle S(\mathbf{R}) \rangle_p = \frac{1}{M\mathcal{N}} \sum_i^{N_f} \{P_i\}, \tag{B.9}$$

where $\mathcal{N}$ is a normalization constant related to the weights p in Eq. (B.8).

The transport operation in Eq. (B.8) accounts for the replication of $S(\mathbf{R})$ contribution. In order to ensure that we are in the asymptotic regime where $\Phi_0(\mathbf{R})/\Psi_T(\mathbf{R})$ is related to the offspring of the $\mathbf{R}$ walker, the series is continued for a while only with the reweighting law

$$\{P_i\} \rightarrow \{P'_i\} = \left\{ \frac{p(\mathbf{R}'_i)}{p(\mathbf{R}_i)} P_i^t \right\}. \tag{B.10}$$

Since our calculations are divided in blocks, we use the evolution law of Eq. (B.8) in the first half of the block, and Eq. (B.10) in the second half. We choose the block length as to minimize the variance of $\{P_i\}$.

APPENDIX C

CONVENTIONS

In this appendix we list our conventions related to the explicit pion formalism, Chapter 4. We use units such that $\hbar = c = 1$. The contravariant space-time and momentum four-vector are given by

$$x^\mu = (t, \vec{x}) \quad , \quad p^\mu = (E, \vec{p}). \tag{C.1}$$

Greek indices μ, ν etc. run over the four space-time coordinate labels $0, 1, 2, 3$, with $x^0 = t$ the time coordinate. Latin indices i, j, k, and so on run over the three space coordinate labels $1, 2, 3$. The metric $g^{\mu\nu} = g_{\mu\nu}$ with $g^{00} = 1$, $g^{ii} = -1$. The covariant versions of the above-mentioned vectors are

$$x_\mu = g_{\mu\nu} x^\nu = (t, -\vec{x}) \quad , \quad p_\mu = g_{\mu\nu} p^\nu = (E, -\vec{p}) \tag{C.2}$$

where summation over repeated indices is always understood; also

$$x^2 = x_\mu x^\mu = t^2 - \vec{x}^2 \quad , \quad p^2 = p_\mu p^\mu = E^2 - \vec{p}^2 \tag{C.3}$$

While for an ordinary three-vector we have, in general, $\vec{x} = (x^1, x^2, x^3)$, there is caution in place with the (three-dimensional) gradient operator which is defined to be

$$\vec{\nabla} = (\partial_1, \partial_2, \partial_3) \tag{C.4}$$

with

$$\partial_i = \frac{\partial}{\partial x^i} = -\frac{\partial}{\partial x_i} = -\partial^i \tag{C.5}$$

The Levi-Civita tensor is

$$\epsilon^{ijk} = \begin{cases} +1 & \text{if } (i,j,k) \text{ even permutation of (1,2,3)} \\ -1 & \text{if odd permuation} \\ 0 & \text{otherwise} \end{cases} \tag{C.6}$$

Note that $\epsilon^{ijk} = -\epsilon_{ijk}$ and for the cross product $\epsilon^{ijk} v^j u^k = [\vec{v} \times \vec{u}]^i$, $\epsilon_{ijk} v_j u_k = [\vec{v} \times \vec{u}]_i$.

The charged and neutral pion field operators are defined as

$$\begin{aligned} \pi_\pm(\mathbf{x}) &= \frac{1}{\sqrt{2}} [\pi_x(\mathbf{x}) \pm i \pi_y(\mathbf{x})] \\ \pi_0(\mathbf{x}) &= \pi_z(\mathbf{x}), \end{aligned} \tag{C.7}$$

so that $\pi_{+,0,-}$ **creates** a $\pi^{+,0,-}$ or **annihilates** a $\pi^{-,0,+}$.

The spin 1/2 and isospin 1/2 operators of the nucleons are defined as $\mathbf{s} = \boldsymbol{\sigma}/2$ and $\mathbf{t} = \boldsymbol{\tau}/2$, where $\boldsymbol{\sigma}$ and $\boldsymbol{\tau}$ are the Pauli matrices operating in spin and isospin space, respectively. The Pauli matrices are

$$\sigma^1 = \begin{pmatrix} 0 & 1 \\ 1 & 0 \end{pmatrix}; \qquad \sigma^2 = \begin{pmatrix} 0 & -i \\ i & 0 \end{pmatrix}; \qquad \sigma^3 = \begin{pmatrix} 1 & 0 \\ 0 & -1 \end{pmatrix}. \tag{C.8}$$

Notice that for isospin components it does not make sense to distinguish between upper and lower indices, thus upper and lower subscripts have the same meaning. The proton and neutron states are defined as:

$$|p\rangle = \begin{pmatrix} 1 \\ 0 \end{pmatrix}; \qquad |n\rangle = \begin{pmatrix} 0 \\ 1 \end{pmatrix}. \tag{C.9}$$

The operator $\boldsymbol{\tau} \cdot \boldsymbol{\pi}$ is

$$\begin{aligned} \boldsymbol{\tau} \cdot \boldsymbol{\pi} &= \tau_x \pi_x + \tau_y \pi_y + \tau_z \pi_z \\ &= \frac{1}{2}(\tau_x + i\tau_y)(\pi_x - i\pi_y) + \frac{1}{2}(\tau_x - i\tau_y)(\pi_x + i\pi_y) + \tau_z \pi_z \\ &= \frac{1}{2}\tau_+(\pi_x - i\pi_y) + \frac{1}{2}\tau_-(\pi_x + i\pi_y) + \tau_z \pi_0, \end{aligned} \tag{C.10}$$

where we can identify $(\pi_x - i\pi_y)/\sqrt{2}$ with the annihilation of a π_+ (or with the creation of a π_-) and $(\pi_x + i\pi_y)/\sqrt{2}$ with the annihilation of a π_- (or with the creation of a π_+).